Spring 1-1-2018

Structural Response and Risk Considering Regional Ground Motion Characteristics

Robert Edward Chase
University of Colorado at Boulder, robert.chase@colorado.edu

Structural Response and Risk Considering Regional Ground Motion Characteristics

by

Robert Edward Chase

B.S., University New Hampshire, 2013

M.S., University of Colorado, 2017

A thesis submitted to the

Faculty of the Graduate School of the

University of Colorado in partial fulfillment

of the requirement for the degree of

Doctor of Philosophy

Department of Civil, Environmental and Architectural Engineering

2018

This thesis entitled:

Structural Response and Risk Considering Regional Ground Motion Characteristics

written by Robert Edward Chase

has been approved for the Department of Civil, Environmental and Architectural Engineering

_____

Prof. Abbie B. Liel

_____

Dr. Nicolas Luco

_____

Prof. Petros Sideris

_____

Prof. Shideh Dashti

_____

Dr. Taojun Liu

Date _____

The final copy of this thesis has been examined by the signatories, and we find that both the content and the form meet acceptable presentation standards of scholarly work in the above mentioned discipline.

ABSTRACT

Chase, Robert Edward (Ph.D. in Civil Engineering)

Structural Response and Risk Considering Regional Ground Motion Characteristics

Thesis Directed by Professor Abbie B. Liel

Regions of the U.S. have different tectonic environments and, correspondingly, seismic ground motion characteristics can vary significantly across the country. Structures' seismic risk depends greatly on these characteristics, which can significantly influence structural seismic response. Current seismic design procedures and many typical assessments only consider ground motion intensity at a structure's fundamental period, and not motion characteristics like frequency content and ground motion duration. This dissertation explores the relationships between regional ground motion characteristics and structural risk through three studies that aim to fill this gap in the literature.

Chapter 2 investigates induced earthquakes in the central U.S. to investigate the characteristics of ground motions and resulting structural response. Ground motion suites of induced motions and tectonic motions with similar earthquake source characteristics are gathered for dynamic analysis on a numerical model of a residential chimney. Tectonic motions are found to produce slightly higher probabilities of chimney collapse, when compared to induced motions of the same intensity. These higher probabilities are due to differences in the frequency content, which stem from differences in depth, stress drop, and regional seismic environment between the two ground motion sets.

Chapter 3 analyzes light-frame wood buildings in sequences of induced motions, through dynamic simulations, to investigate damage and seismic loss accumulation in multiple shaking

events. The study finds that, although cracks widen and elongate in subsequent events, the vulnerability of new light-frame wood construction does not increase when initially damaged at levels observed in recent induced events. However, seismic losses or repair costs may increase dramatically if owners are repairing after every event.

In Chapter 4, light-frame wood buildings are simulated using hazard-consistent incremental dynamic analysis to assess collapse capacities and expected seismic loss, for one to four-story commercial and multifamily buildings at sites in California and the Pacific Northwest. Modification factors for design base shear are developed for these buildings to account for site-specific spectral shape. Collapse risk, losses, and design base shear are found to be higher for sites with larger contributions from subduction hazards, due to broader motion frequency content and, to a lesser extent, longer shaking durations.

DEDICATION

To family and friends.

ACKNOWLEDGMENTS

First and foremost, I would like to thank my advisor, Professor Abbie Liel. Throughout my time at CU, Abbie has gone above and beyond to help me become a better student, researcher, writer, and person. She has demonstrated incredible patience even when I know it was not easy. I could not have completed this work without her guidance and support and for that I am forever thankful. Thank you, Abbie!

I would also like to extend a huge thank you to Dr. Nicolas Luco for his additional support and guidance on multiple projects throughout my Ph.D. The additional insight and advice on multiple areas in my research and career is invaluable and for that I am truly thankful.

I would also like to thank the other members of my committee, Professor Petros Sideris, Professor Shideh Dashti, and Dr. Taojun Liu. Their input and comments on this dissertation are a tremendous help and for that I am thankful.

A big thanks to Zach Bullock with his help with ground motion prediction equations and correlation models incorporated in this research.

A huge shout out to all research group members and officemates. I can't thank the current group enough. Thanks to Jakub, Dustin, Sam, Polly, Bridger, Casie, and Zach for the donuts, coffee, snacks, and other great times in and out of the office. Another huge shout out to the older members including Cody, Sarah, Yolanda, Sean, Julio, Mark, Travis and many others.

Last, but certainly not least, I would like to thank my parents and sister for the unwavering love and support. I know I would not be in the position I am in today without it.

I would like to acknowledge the contributions of Bridger Baird, Guido Camata, Reagan Chandramohan, D. Jared Debock, Greg Deierlein, Morgan Moschetti, Anne Sheehan, Nicola Tarque, Melanie Walling, Isabel White, and Kuanshi Zhong. I also thank Ershad Ziaei Ghehnavieh

and Weichiang Pang for sharing their models of wood light frame buildings. I also would like to thank HB Risk for the license to use their product, Seismic Performance Prediction Program (SP3).

This material is based upon work supported by the National Science Foundation (NSF) under Grant No. 1515438 to the Colorado Collaboratory for Induced Seismicity. Any opinion, findings, and conclusions or recommendations expressed in this material are those of the author(s) and do not necessarily reflect the views of the National Science Foundation. Initial work was also funded by a University of Colorado Innovation Seed Grant. Furthermore, additional NSF funding was provided under the Graduate Research Internship Position (GRIP) supplement.

This work utilized the RMACC Summit supercomputer, which is supported by the National Science Foundation (awards ACI-1532235 and ACI-1532236), the University of Colorado Boulder, and Colorado State University. The Summit supercomputer is a joint effort of the University of Colorado Boulder and Colorado State University (Anderson, et al., 2017).

TABLE OF CONTENTS

LIST OF TABLES

LIST OF FIGURES

CHAPTER 1

1 INTRODUCTION

1.1 OVERVIEW AND MOTIVATION

In some parts of the country, earthquakes present a significant risk to buildings and other infrastructure. There are significant uncertainties in quantifying this risk. One form of uncertainty stems from the variability in the characteristics of ground motions created by these earthquakes. Ground accelerations are the primary cause of damage to buildings and bridges, and can vary in amplitude, frequency content, and duration, among other characteristics. Quantifying the link between earthquake properties, the resulting ground motions, structural response, seismic risk and structural design is vital to ensure that we are designing buildings that can protect their occupants during a major earthquake, thereby contributing to more resilient communities. Understanding this link is particularly important today as modern seismic design in the U.S. aims to achieve uniform risk at high seismic sites across the country (ASCE, 2016; International Code Council, 2018). At the present time, design and assessment strategies consider primarily shaking amplitude variation across the country, with less attention to regional differences in frequency content and spectral shape.

This dissertation attends to relationships between regional earthquake characteristics and ground motion characteristics to improve understanding of structural seismic response considering ground motions from different types of earthquake events. The three studies presented in Chapter 2[1], Chapter 3[2], and Chapter 4[3] each seek to investigate different facets of this topic. Chapter 2 investigates the influence of human-caused, or induced, earthquakes on brittle structures; Chapter

[1] This study is in preparation to be submitted for publication at *Seismological Research Letters*.
[2] This study is in preparation to be submitted for publication at *Earthquake Engineering & Structural Dynamics*.
[3] This study is in preparation to be submitted for publication at *Engineering Structures*.

3 examines the effect of a series of low to moderate magnitude earthquakes, like those occurring in swarms of induced events, on damage and damage accumulation in light-frame wood buildings; Chapter 4 explores how expected ground motion frequency content and duration, consistent with a site's seismic hazard, influence a building's expected collapse capacity, seismic loss, and seismic design.

Past research has investigated connections between earthquake and ground motion characteristics, such as magnitude, ground motion intensity, frequency content, and duration, and structural response. For example, Joyner & Boore (1988) linked earthquakes and ground motion characteristics, demonstrating that spectral accelerations and velocities increased with larger earthquake magnitudes. Joyner & Boore (1988) also showed how spectral shape is influenced by earthquake characteristics such as magnitude and rupture distance. Furthermore, spectral shape has been found to influence structural response greatly when we are interested in seismic performance in the nonlinear regime. In one pioneering study in this area, Baker & Cornell (2006) demonstrated that spectral shape and ground motion record selection techniques had a significant impact on structural response due to period elongation as a structure becomes damaged. In terms of duration of shaking, Trifunac and Brady (1975) showed ground motion duration increased with earthquake magnitude and rupture distance. Ground motion duration may also significantly influence structural response. Bommer et al. (2004) showed that an increased duration of shaking produced greater strength and stiffness degradation in structures over a range of different periods. Currently, research is advancing in an effort to implement modifications in current codes and risk assessments to account for the effect of regional tectonic environment on ground motion duration and spectral shape in structural design (Chandramohan, 2016). Other ground motion characteristics, such as vertical shaking (Harrington & Liel, 2016) and velocity pulses (Baker,

2008), have also been shown to impact structural response, but these characteristics are not considered in this dissertation.

1.2 DISSERTATION OUTLINE

This dissertation aims to advance knowledge of the influence of regional characteristics of unique ground motions, such as induced seismicity experienced in Oklahoma and the central U.S. or subduction earthquakes in Cascadia, affect seismic risk, especially focusing on characteristics of frequency content and ground motion duration.

In Chapter 2 of this dissertation, the connection between earthquakes, ground motion characteristics, and structural fragility are examined by evaluating the response of brittle structures in induced earthquakes. Induced earthquakes are man-made seismic events that have been occurring around the world and have been caused by numerous processes, including oil and gas activities (Rubinstein, 2015). This study focuses on earthquakes caused by wastewater injection in central Oklahoma and southern Kansas. The number of earthquakes in this region has increased significantly since approximately 2009, with 888 $M_W \geq 3.0$ earthquakes occurring in 2015, compared to only 130 experienced in California in the same year. More recently, earthquake rates have decreased somewhat, with over 400 $M_W \geq 3.0$ earthquakes in Oklahoma in 2017 (USGS, 2017; Petersen, et al., 2018). Even with this significant increase in seismicity, few previous studies have been conducted to examine how these induced ground motions impact local infrastructure in this region, which is of concern due to the lack of consideration to seismic forces in structural design.

Chapter 2 compares the differences in structural response of brittle structures when subjected to induced ground motions versus similar natural (tectonic) ground motions. To do so, a

simulation model of a residential chimney is subjected to two different suites of ground motions: one of induced motions and one of tectonic motions. Differences in structural response and collapse are related to ground motion characteristics and earthquake source parameters. Specifically, Chapter 2 shows that tectonic ground motions have a greater probability of causing collapse than induced ground motions for a given ground motion intensity level. These differences stem from variability in frequency content and, to a lesser extent, shaking duration between the two ground motion sets. The difference in frequency content is shown to be a product of differences in regional seismic environment between the western and central United States. Differences between earthquake rupture depths, stress drops, and geometric attenuation also proved to influence the differences in frequency content between the induced and tectonic ground motion sets. This study has been submitted and is currently under review for publication.

Chapter 3 examines how damage may accumulate if a structure is subjected to multiple small to moderate magnitude earthquakes. Induced earthquakes in Oklahoma and southern Kansas have thus far been of smaller magnitude than the larger earthquakes typically considered in seismic hazard and risk assessments. Indeed, the largest induced earthquake thus far in Oklahoma recorded a moment magnitude of M_W 5.8. However, these induced events have tended to occur in swarms with multiple events occurring within a short time period (Llenos & Michael, 2013). This phenomenon motivates research to quantify how building fragilities, damage accumulation and seismic losses sustained from these induced swarms can propagate throughout a seismic sequence. Most earthquake engineering assessments are based on how an undamaged structure will perform in an earthquake. However, mainshock-aftershock studies, such as Raghunandan et al. (2015), have found that once a structure is significantly damaged in an initial earthquake, its susceptibility to collapse increases greatly. Ghosh et al. (2015) developed a framework to examine the

accumulation of damage from multiple shaking events. That study found that bridge damage indices increased for scenarios where multiple seismic pulses were observed.

Thus, Chapter 3 quantifies damage and seismic losses for light-frame wood buildings when subjected to sequences of smaller magnitude events. Three research questions are investigated. First, what damage can we expect in light-frame wood construction in induced earthquakes? Second: how does this damage change if the building experiences an earthquake sequence? Finally, are these results consistent with observations from the central U.S. to date? To conduct this investigation, one and two-story multifamily wood frame buildings are designed, and their seismic response dynamically simulated using three-dimensional (3D) nonlinear models subjected to recorded ground motion sequences from induced earthquakes. Damage is quantified through seismic losses, which are estimated using the FEMA P-58 methodology (FEMA, 2012). This methodology considers damage to nonstructural components, even when damage to the structural system itself may be limited. To address the impact of earthquake sequences, we examine how expected losses and building vulnerability will accumulate and/or change over a sequence of earthquakes, and compare damages observed in past events to the simulation results.

Results show that, at levels of shaking experienced in recent earthquakes, minor damage, consisting of cracking of interior finishes and non-structural damage to plumbing and HVAC systems is expected, which is consistent with the observed damage. The study also examines how expected losses and building vulnerability will accumulate and/or change over a sequence of earthquakes. Results indicate that damage quantified in terms of absorbed hysteretic energy tended to accumulate over the sequences. This damage corresponds to elongation or widening of cracks. However, vulnerability is not significantly altered by damage in a preceding event, and losses do not change if the building is only repaired once at the end of the sequence, as this worsening of

damage does not significantly alter repair actions. If repairs are conducted after each earthquake, the total seismic losses increase greatly from the sequence. This study has been submitted and is currently under review for publication.

The research in Chapter 4 quantifies expected seismic losses and collapse risk in light-frame wood buildings, considering region-specific seismic hazard differences between California and Cascadia that can influence duration and frequency content of shaking and, as a result, seismic risk. One-, two-, and four-story multifamily and commercial light-frame wood buildings are analyzed through dynamic simulations to estimate seismic loss and collapse risk and show the influence of seismic environment. The study employs the hazard-consistent incremental dynamic analysis methodology, developed by Chandramohan (2016), and examines risk in six different west coast cities.

Ultimately, the study finds that light-frame wood building response correlates strongly with spectral shape, but correlates weakly with ground motion duration. The weak correlation with duration is due to the relatively low ductility of these buildings when compared to other types of buildings previously examined in other ground motion duration studies (Chandramohan, et al., 2016; Raghunandan & Liel, 2013). Sites with large contributions from subduction hazards, namely Portland, Anchorage, and Eugene, have higher expected seismic losses and higher expected collapse risk for light-frame wood buildings, due to flatter, less peaked spectral shapes.

The study also explores how much design values for the ASCE 7 (2016) equivalent lateral force procedure would need to be altered to ensure uniform collapse risk across sites, considering the influence of both subduction and crustal events. This study finds that design base shear should be increased at sites with large contributions from subduction earthquakes and potentially for crustal sites with contributions from large magnitude earthquakes at close rupture distances.

However, the selection of conditioning intensity level and the reference site (for duration and spectral shape) should be considered carefully as these factors have a large influence on potential changes to design base shear. This study is being prepared for submission for publication.

Overall, the findings from this dissertation advance the knowledge of how ground motions specific to the different regions across the United States influence structural response and risk. The overall goal is to contribute to seismic design and assessment procedures that will ultimately make communities more resilient and better prepared for damaging seismic events.

CHAPTER 2

2 EFFECT OF GROUND MOTIONS FROM INDUCED EARTHQUAKES ON RESPONSE OF BRITTLE STRUCTURES

2.1 INTRODUCTION

Seismicity has drastically increased in parts of the central United States, including Oklahoma, Texas and southern Kansas, in the past several years (Ellsworth, et al., 2015; Frohlich, et al., 2016; Wilson, et al., 2017; Petersen M. , et al., 2018). Oklahoma, for example, has experienced the two largest earthquakes in its recorded history (2011 Prague M_W 5.7 and 2016 Pawnee M_W 5.8) during this time, as well as a sharp increase in the frequency of smaller events (USGS, 2016). The deep disposal of wastewater byproducts of oil and gas production processes (including, but not limited to, hydraulic fracturing) is believed to be the major contributor to the seismicity increase in these regions (Rubinstein, 2015; Weingarten, et al., 2015). The United States is home to thousands of wastewater injection wells, though only about 10% have been linked to seismic activity (NRC, 2013).

Despite the relatively low magnitude of these events, this seismic activity has caused structural and nonstructural damage to buildings and infrastructure, particularly in Oklahoma. For example, multiple buildings sustained minor to moderate damage, including to brick veneer, in the M_W 5.8 Pawnee earthquake, which also affected structures on the Oklahoma State University campus (Bitton, 2016; Clayton, et al., 2016). The 2011 M_W 5.7 Prague event also had significant impacts, including severe damage to a masonry building at St. Gregory University and to chimneys in the area (Lacey, 2011). Additionally, lower magnitude recent earthquakes have caused cracking in house foundations, failure of nonstructural masonry components of buildings, such as chimneys, and interruptions to electrical power (Barrett, 2016; Jampole, 2017), There is also concern about

potential damage to pipelines and oil industry infrastructure. This damage is the source of millions of dollars in insurance claims in Oklahoma alone, and these claims undoubtedly underestimate the total economic impacts of damage, as only about 15% of property owners in Oklahoma have even some level of earthquake insurance (Barrett, 2016). Beyond economic impacts, damage to the built environment from induced earthquakes is having other effects, leading to changes in regulations of wastewater disposal activities, legal action, including a number of class action lawsuits underway in Oklahoma and elsewhere, and sparking concerns about "immediate danger to health, safety, and welfare" (State Corporation of the State of Kansas, 2015). However, little is known about the potential of induced earthquakes to cause damage to the built environment and whether the patterns of damage are similar to or different from tectonic events. Addressing this gap requires investigation at the intersection of seismology and engineering to understand how ground motions from induced earthquakes, as used and interpreted by earthquake engineers, may affect the built environment.

This study investigates the effects of ground motions from induced earthquakes on the response of brittle structures and compares these effects to response from tectonic earthquakes. To do so, we employ a suite of recorded acceleration time histories from induced earthquakes with large enough shaking intensities and broadband frequency content for engineering analysis, as well as a comparable set of tectonic (non-induced) ground motions. We then simulate the dynamic response of brittle structures under these motions up to collapse, using a nonlinear model, and state of the art earthquake engineering analysis techniques. Structural response is primarily quantified in terms of collapse capacity, a measure of the minimum ground shaking intensity necessary to cause collapse. Brittle structures are of interest because they are prevalent in the affected parts of the country and have presented the highest profile damage in recent events. The set of brittle

structures interrogated includes a two-dimensional model representing a residential brick chimney, of the type that has experienced damage in recent events in Oklahoma and elsewhere. Subsequently, key characteristics of the structure, including strength, fundamental period, and ductility, are varied to investigate brittle structures more broadly, and to determine which structural characteristics most affect the response of the structure, with a focus on comparison of seismic fragilities between induced and tectonic motions. Results are analyzed to correlate assessed collapse capacities with ground motion parameters (e.g., frequency content and duration) and underlying earthquake parameters known to influence ground motion characteristics (e.g., focal depth, stress drop, and geometric attenuation). Though the way that ground motions and ground motion characteristics influence structural response is well documented and understood, this study explicitly examines the extent to which this knowledge is applicable to induced motions.

2.2 METHODS

2.2.1 Ground Motions

Acceleration time histories recorded from induced and tectonic earthquakes were gathered for input to engineering analyses. Induced ground motions from the database assembled by Assatourians & Atkinson (2018) were provided for use in this study. These induced earthquakes include those from Oklahoma, Southern Kansas, and Alberta, Canada, recorded between February, 2011 and September, 2016 (Assatourians & Atkinson, 2018). These are "confirmed" induced events, indicating that the scientific community generally considers these events to be human caused. This suite of induced records contains records which have been processed for engineering analysis.

The database collected by Assatourians & Atkinson (2018) contains both horizontal components and the vertical component of 68 records from 26 different earthquakes recorded at 31 different stations. These earthquakes have moment magnitudes (M_w) ranging from 4.0 to 5.7 (median 4.4) and occurred at a median rupture depth of 4.5 km. From each set of records, the maximum horizontal component, as determined by the motion having larger spectral acceleration at the first-mode period of the baseline chimney of 0.26s, or Sa(T=0.26s), was selected for use in this study. The vertical component of shaking is not considered in this study. Each record in this ground motion suite has a PGA of 0.013g or higher. The median rupture distance (R_{rup}) for the induced suite is 8.8 km. R_{rup} is defined as the shortest distance from the site to the fault rupture plane.

A set of tectonic motions with similar magnitudes and site-to-source distance to the induced motion set were chosen from historic earthquakes presumed to have resulted from natural (non-induced) processes. These 68 tectonic motions were obtained from the PEER NGA-West2 Ground Motion Database (Ancheta, et al., 2013) focusing on recorded motions with similar magnitude and rupture distances to the induced set. Previous studies, e.g. Chase & Liel (2017), have shown that an important characteristic of the induced earthquakes from the perspective of structural response is that they are largely of smaller magnitude than tectonic earthquakes from which ground motions are used in engineering analysis. This study aims to remove this discrepancy by selecting a tectonic ground motion suite with records from earthquakes with a similar distribution of magnitudes to the induced set. The 68 tectonic ground motions in this suite are from 31 earthquakes with moment magnitudes ranging from 4.0 to 5.7 (median 4.4), and occurring at a median rupture depth of 7.0 km. The mean rupture distance (R_{rup}) for the tectonic suite is 9.6 km. The crustal records gathered in the tectonic suite are from a range of geographic locations, with most records from California

and Italy. The NGA-West2 database is comprised of shallow crustal earthquakes in active tectonic regimes (Ancheta, et al., 2013). The records in this database are suitable for comparison to induced records due to their similar magnitudes, rupture distances, and depths as well as similar attenuation characteristics as is shown Atkinson et al. (2018) and Moschetti et al. (2018).

Although the record sets were collected to be as similar as possible, there are differences in the ground motions selected due to limitations in available records. Figure 2.1 compares the earthquake (*i.e.*, M_w, depth, rupture distance), and ground motion (*i.e.*, PGA, Sa(T=0.26s), and 5-75% significant duration (Bommer & Martinez-Pereira, 2000)) characteristics of the two sets. The median Sa(T=0.26 sec) is quite similar between the two sets, but the PGAs between the two sets differ more substantially. The induced set median PGA is 0.12g and the tectonic set median PGA is 0.04g. This relationship between PGA and Sa(T=0.26s) is indicative of differences in spectral shapes between the two sets, which are explored in more detail later in this paper. Figure 2.1 also shows that the tectonic ground motions are from earthquakes occurring deeper (median depth is 37% deeper) than the induced motions. The tectonic ground motions have slightly longer significant durations (median duration is 14% longer). The average shear wave velocity in the top 30 m of the soil at the recording site ($V_{s,30}$) are fairly similar, with both sets recorded on sites with soil conditions.

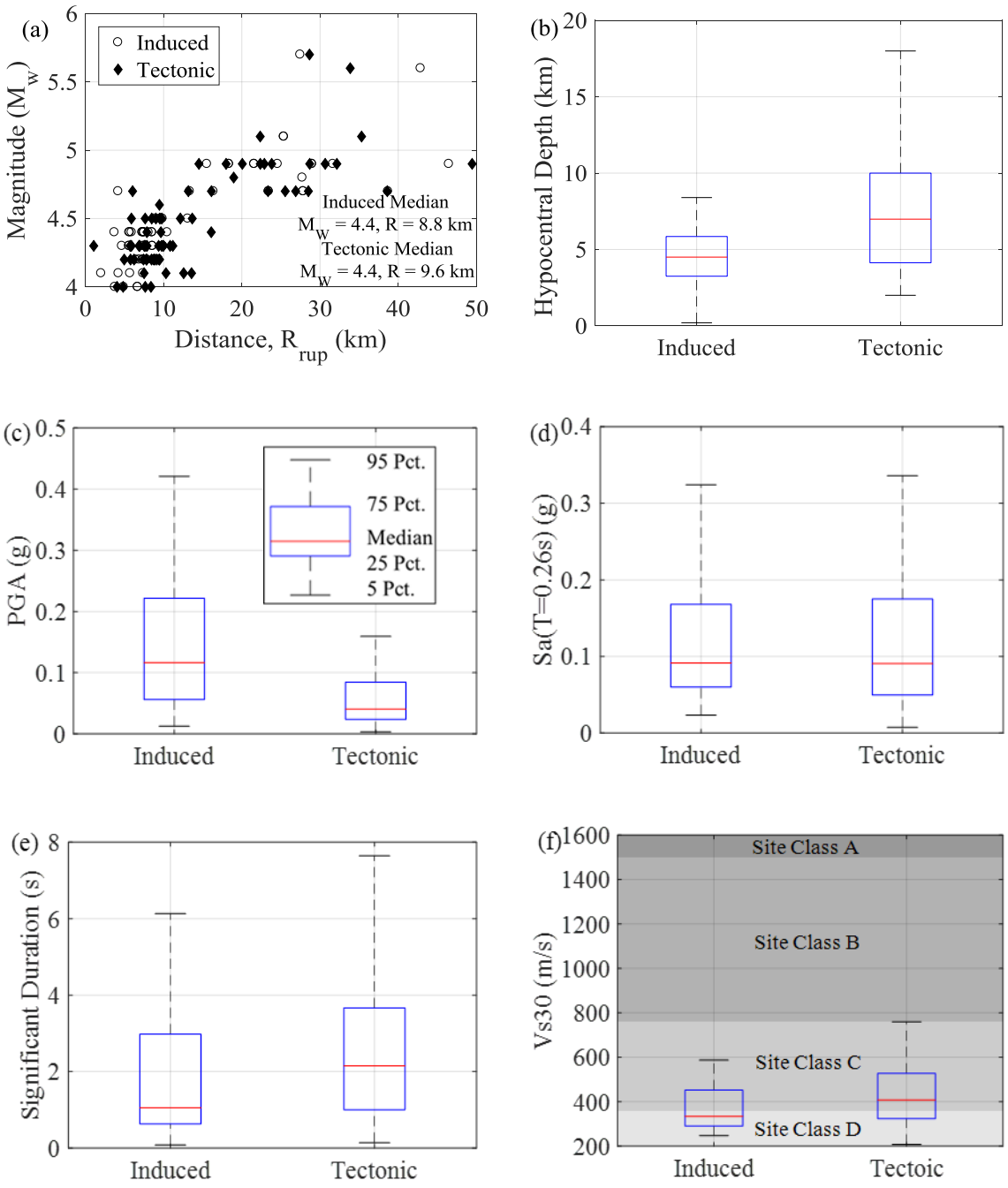

Figure 2.1. Characteristics of earthquakes and ground motions in induced and tectonic sets, including: (a) scatterplot of rupture distance (R_{rup}) versus moment magnitude (M_W), and boxplots showing (b) hypocentral depth, (c) PGA, (d) Sa(T=0.26s), (e) 5-75% significant duration, and (f) $V_{s,30}$. The legend for the boxplots is provided in (c).

2.3 Modeling of Brittle Structures

To quantify the influence of induced versus tectonic motions on structural response, we simulate the response of a set of nine brittle structures with varying characteristics. The first, baseline, model is calibrated to represent the dimensions and characteristics of a typical residential building chimney (The Donley Brothers Company, 1936), shown in Figure 2.2(a). The chimney is comprised of unreinforced conventionally-sized red clay bricks and mortar, and we analyze the response of the chimney shaking in the direction parallel to the exterior wall of the house. In this direction, the anchorage between the wood frame of the home and the chimney is often weak, and is assumed not to significantly impact the chimney's response, so the structure is modeled with a fixed base. These structures are brittle, but flexure critical (i.e. moment not shear governs the response of these slender structures) (TMS, 2011).

A diagram of the baseline model, and its key nonlinear properties, is provided in Figure 2.2(b) and (c). The model was created in the *OpenSEES* structural analysis platform (PEER, 2016b), employing a concentrated hinge approach (e.g., Consigilio Nazionale Delle Ricerche Commissione, 2013). As depicted in Figure 2.2(b), the *OpenSEES* model consists of a set of elastic elements connecting concentrated mass nodes, with a single nonlinear rotational spring at the base of the flue. The spring mimics the dominant failure mechanism expected, in which a horizontal (flexural) crack forms at the joint between the flue and the chimney base. It is possible for failure to occur in other regions of the chimney, however flexural cracking at the base of the flue was the observed failure mechanism in all simulations with an initial finite element model described in more detail in Appendix A.1. Therefore, the *OpenSEES* model was developed as shown in Figure 2.2(b). The spring is assigned a trilinear monotonic backbone (Figure 2.2(c)) using the "hysteretic" material model. In the elastic range, the spring is very stiff, and the elastic elements control the

response. The nonlinear properties (Figure 2.2(c)) of the spring are shown in Figure 2.3, and were obtained through calibration to a finite element model (described in detail below). The flexural strength is 4.7 kN, consistent with established strength calculations (TMS, 2011). The spring does not deteriorate cyclically, as is appropriate for brittle structures that do not undergo many cycles (Magenes & Calvi, 1997). The fundamental (uncracked) period of the model, T_1, is 0.26 sec. Five-percent Rayleigh damping was applied at the first and third modes considering the tangent (updated) stiffness for dynamic analysis. For the chimney, the first mode was by far the most dominant in seismic response and higher mode effects, beyond the third mode, were negligible. In addition, corotational effects are incorporated.

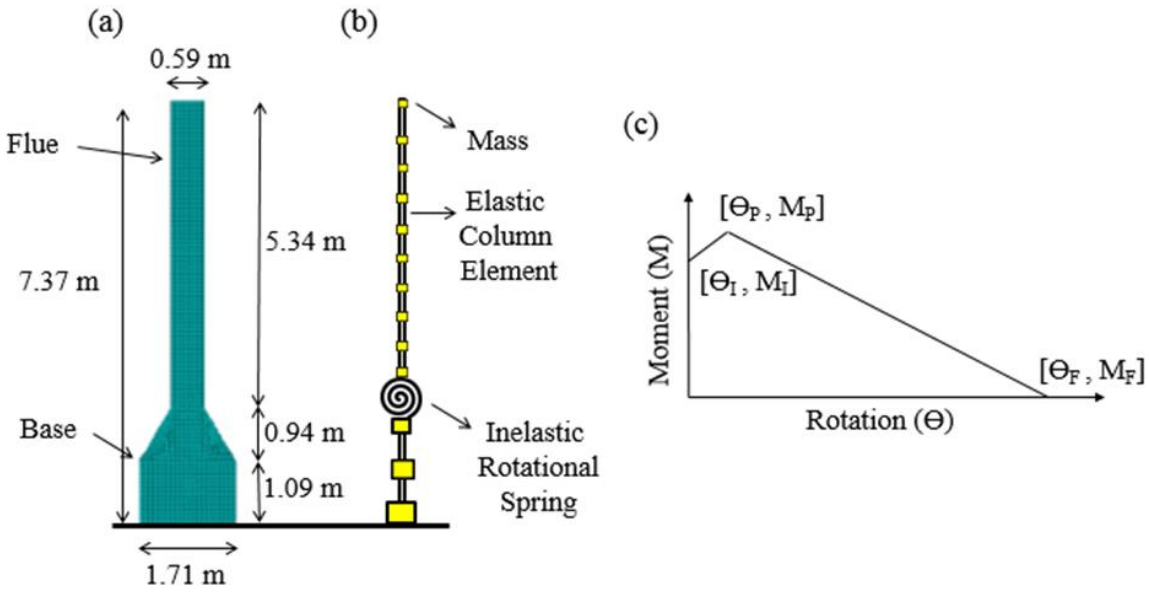

Figure 2.2. Model of baseline brittle structure showing (a) chimney dimensions, (b) *OpenSEES* modeling approach to capture flexural response, and (c) monotonic trilinear backbone of the nonlinear rotational spring.

We then examine variations of the baseline model to explore the influence of structural characteristics on the observed differences in response between the induced and tectonic motions, as outlined in Figure 2.3. Three of these variants are intended to examine the elastic properties of the structures and the effect of the structures' fundamental period on the response, as shown in

Figure 2.3(a). (Here, T_2 indicates the building for which the period, T, of the baseline model was multiplied by a factor of 2; similar identifiers are used for all structure variant cases.) We also vary the properties of the hysteretic spring to represent differences in the nonlinear characteristics (5 cases). $M_{0.75}$ and $M_{1.25}$ (Figure 2.3(b)) are examined to quantify the influence of the strength; strength is also explored by scaling ground motions, as described in more detail later. The rotation capacity, $\Theta_{P,}$ and post-peak rotation capacity, $\Theta_{F,}$ are investigated by the range of factors reported to quantify the response for structures with varying deformation (ductility) capacity (see Figure 2.3(c) and (d)). When one parameter is varied, all other cases remain at the baseline values, apart from $M_{0.75}$ and $M_{1.25}$, in which M_I and M_P are decreased or increased together.

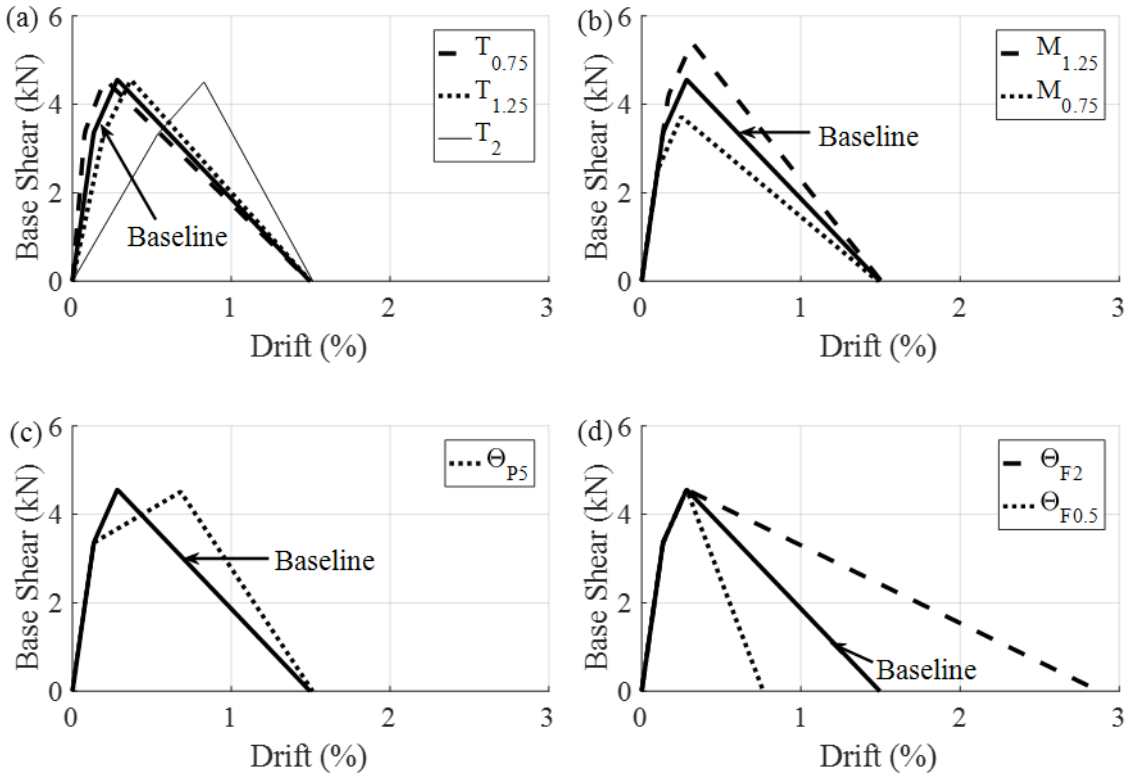

Figure 2.3. Pushover analysis results for the set of brittle structures examined, showing: (a) changes in natural period, (b) changes in strength, (c) changes in rotation capacity (Θ_P), and (d) changes in post-peak rotation capacity (Θ_F).

The nonlinear model parameters for the baseline model, shown in Figure 2.2(c) and Figure

2.3, were calibrated to the results of a finite element model of the chimney using the *ABAQUS* software. In this model, the masonry is modeled with an isotropic homogenous material, which is intended to capture the composite behavior of masonry, including the element stress-strain response of clay brick units, mortar between the bricks, and their interface, similar to (Lourenco, et al., 1998; Pallarés, et al., 2006; Calderini & Lagomarsino, 2008; Tarque, et al., 2014). In our model, this material was assigned the Lee & Fenves (1998) material model. The properties of this material were calibrated using a red clay brick and mortar wall specimen also modeled in *ABAQUS*, which could be compared to experiments from Lourenco (1996). Chase & Liel (2017) showed that the chosen material provided a reasonable match with the wall experiments, in terms of the static force-displacement curves and failure mechanisms. The calibrated masonry material model was then assigned to the *ABAQUS* chimney model. More detail is provided on the calibration of this material model in Appendix A.1. Figure 2.4 shows that there is reasonable agreement between the force-displacement responses of the *OpenSEES* model and the more detailed finite element model in pushover analysis.

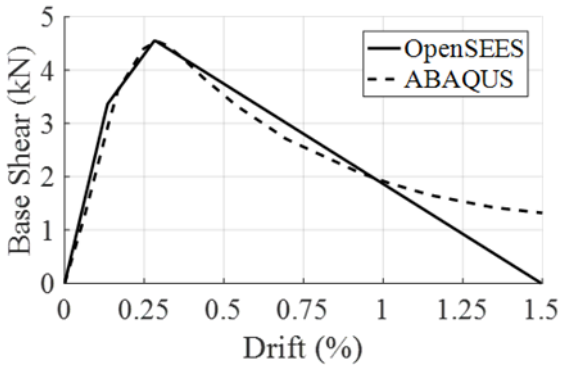

Figure 2.4. Pushover results for the finite element (*ABAQUS*) and *OpenSEES* models due to mass-proportional monotonic lateral loading. Drift is defined as the top displacement, divided by the height of the flue (5.34 m), quantified as a percentage.

2.4 SEISMIC RESPONSE OF BRITTLE STRUCTURES

The seismic response and fragility of the baseline chimney was quantified through incremental dynamic analysis (IDA) of the *OpenSEES* model. IDA (Vamvatsikos & Cornell, 2002) is a well-established technique in which a ground motion is applied to the structural model, recording the structure's peak response (*e.g.,* drift) as a function of the ground motion intensity (quantified by, for example, spectral acceleration or PGA). That motion is then scaled to higher intensities until the structure fails or collapses. The process is subsequently repeated for multiple ground motions to capture the record-to-record variability in structural response. IDA is widely used in structural engineering seismic risk assessments for which strong motion recordings for the earthquake scenario of interest is not available. In particular, IDA can be an appropriate choice where there are a limited number of recordings intense enough to cause collapse without scaling and facilitates, with a single analysis, variations of the ratio of ground motion intensity to building strength. There is substantial research in the earthquake engineering about the potential pitfalls of this approach. In particular, bias can be produced by record scaling if the spectral shape of scaled records is not consistent with the seismic hazard at a site of interest (Baker, 2011), but the implications of this bias can be considered in interpretation of the results. We select spectral acceleration at the fundamental period of the chimney, Sa(T=0.26 sec) as the ground motion intensity measure in this study.

In this study, structural responses from the 68 induced motions and 68 tectonic motions are assessed through separate IDAs to compare response between the two suites of motions, as shown in Figure 2.5 for the baseline model. When comparing the IDA results from the induced and tectonic motions, there is (unsurprisingly) good agreement when the baseline structure responds in the elastic range (*i.e.*, when the drift is below approximately 0.25%). In this range, the response

is governed by the elastic intensity measure demand. When the drift exceeds about 0.25%, the response becomes nonlinear in both cases. Collapse, or chimney toppling failure, was defined to occur when the structural response reaches 1.5% drift, and corresponds to the point at which the chimney has no lateral resistance (base shear is zero) in the pushover analyses (Figure 2.4). This value is consistent with estimates of drift capacities of 1.5-2% for tall, slender masonry elements failing in flexure (Consigilio Nazionale Delle Ricerche Commissione, 2013). When Θ_F is varied, the failure criterion was adjusted according to the pushovers in Figure 2.3(d). In addition, we note that as the IDA curves are very flat around this drift value, the collapse capacities are not sensitive to the value selected. Drift is defined as the top displacement divided by the height of the flue (5.34 m), quantified as a percentage.

IDA results are summarized in Figure 2.5(c) through collapse fragility curves, which describe the probability of collapse as a function of ground motion intensity. A lognormal probability model was fit to the IDA results using the method of moments to define the median collapse capacity and the variation therein, separately for the induced and tectonic ground motion sets. Comparing the fragility curves shows that, for the intensity measure considered, the tectonic ground motions have a higher probability of collapse for a given intensity of shaking, *i.e.*, lower median collapse capacities.

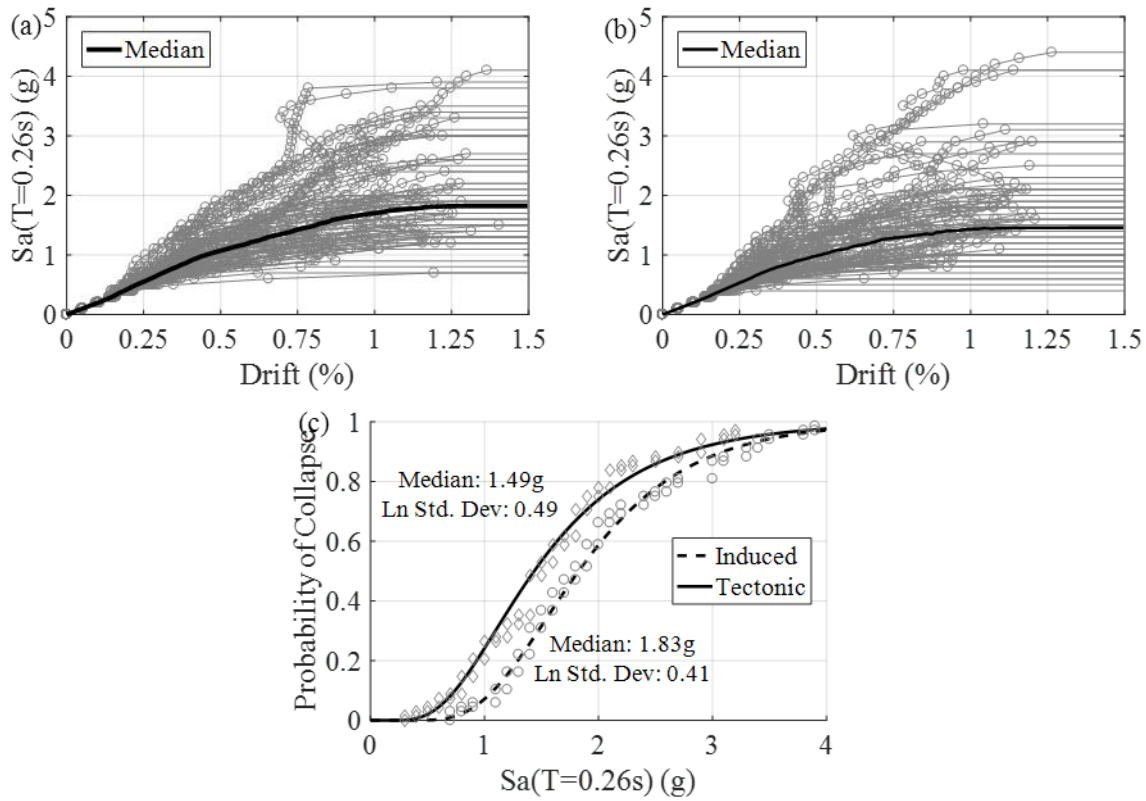

Figure 2.5. Dynamic response when baseline structure is subjected to (a) induced and (b) tectonic ground motion sets. Each gray line represents the results from an individual ground motion. In (c), collapse fragility curves obtained are compared between the induced and tectonic ground motion sets, with ground motion intensity quantified by spectral acceleration at 0.26s.

2.5 EFFECT OF STRUCTURAL CHARACTERISTICS

Figure 2.6 compares the effect of the induced and tectonic motions on the collapse capacity of the other brittle structures (Figure 2.3). As expected, the results of the sensitivity analysis show that as a structure becomes more ductile, higher ground shaking intensities are required for collapse to occur (see cases Θ_{F2} and Θ_{P5} in Figure 2.6), and conversely when ductility is reduced ($\Theta_{F0.5}$). These trends are observed for both induced and tectonic motion sets.

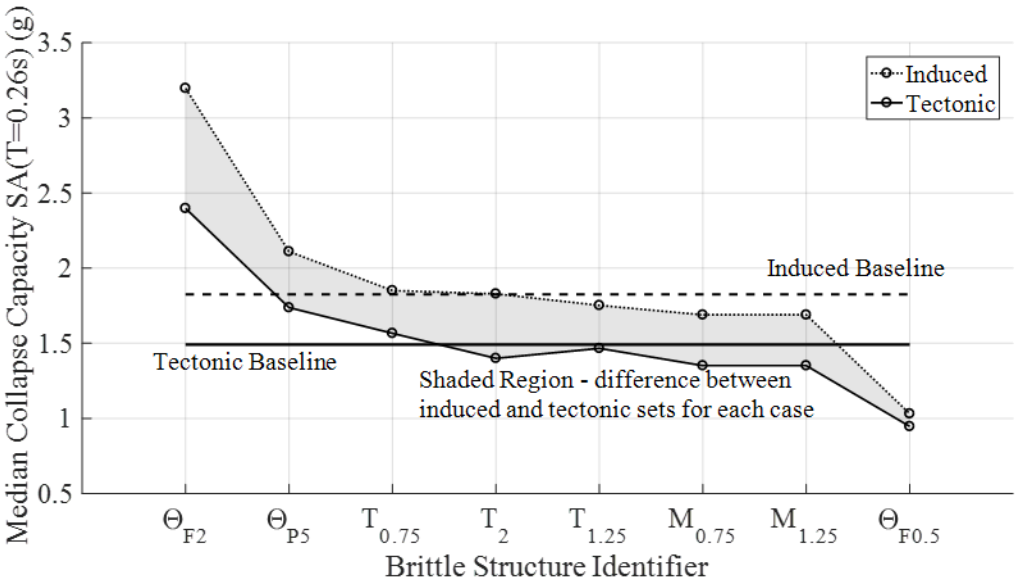

Figure 2.6. Median collapse capacities for the set of brittle structures, comparing results from induced and tectonic motions.

Of crucial importance here, however, is that the gap between the induced and tectonic collapse capacities also increases when the structure is more ductile (Θ_{F2} and Θ_{P5}), such that induced motions appear relatively more benign in comparison to the tectonic motions. In other words, when subjected to induced motions, the structures benefit more from the added ductility than when subjected to tectonic motions, due to the differences in frequency content between the ground motion sets. To illustrate this point, Figure 2.7(a) shows the median response spectrum from the motions causing collapse of the baseline model, for both induced and tectonic sets. This figure also indicates the range of periods, represented by the fundamental (elastic) and elongated (damaged) structural periods, and thus showing the spectral accelerations the baseline structure is subjected to during ground shaking that brings it to collapse. The damaged period is obtained from eigenvalue analysis just before collapse during collapse-level ground motions. Figure 2.7(a) reveals that in the period range affecting the chimney, the spectra from the induced motions is slightly steeper than the tectonic motions; as a result, these motions are relatively less damaging

than the tectonic motions. Since ductile structures exhibit more period elongation, these differences in frequency content have a bigger impact on the more ductile structures. The reverse is true for the less ductile structures.

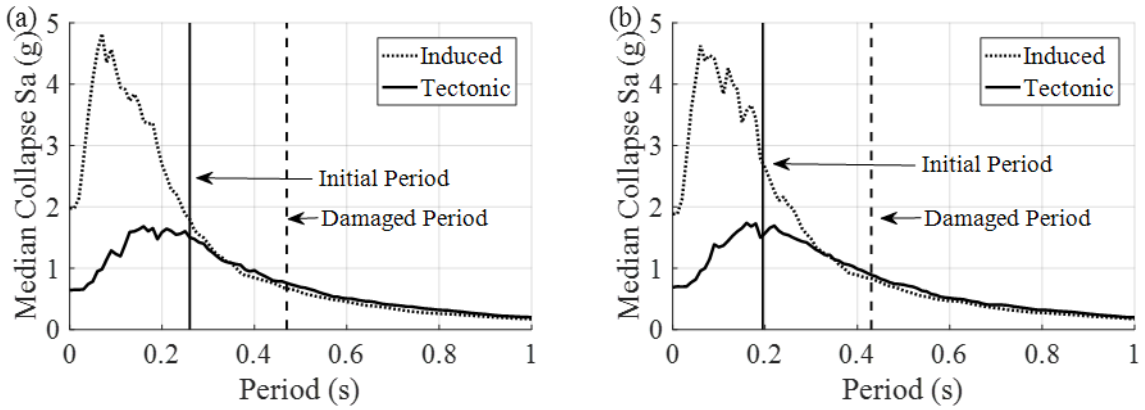

Figure 2.7. Median response spectrum when ground motions are scaled to collapse for tectonic and induced ground motion sets for (a) the baseline model and (b) the stiffer $T_{0.75}$ model. The initial (fundamental) period and the elongated (damaged) period are also shown on each plot.

Figure 2.6 also reveals little difference in collapse capacities, or the relative influence of the induced and tectonic motions, when the strength or the fundamental period of the structure are varied. Even for these relatively brittle structures, the collapse response is dominated by ductility capacity, and changes in ductility. However, for the stiffest structure, $T_{0.75}$, there is a subtle increase in the difference between the induced and tectonic collapse capacities. This increase is examined in Figure 2.7(b), where the median response spectrum for each ground motion set, at the collapse level, are compared. The differences between induced and tectonic collapse spectra between the initial and damaged periods is greater than the comparable spectra for the baseline case (Figure 2.7(a)), explaining the increase in difference between the median collapse capacities in Figure 2.6. If the baseline model were more brittle, then strength and fundamental period would likely show more of an impact in the sensitivity analysis. A more brittle structure would be less

sensitive to higher spectral energies when experiencing period elongation, thus its structural response would be more sensitive to the ultimate strength and intensities experienced at its fundamental period.

2.6 EFFECT OF GROUND MOTION AND EARTHQUAKE CHARACTERISTICS

These results suggest that induced ground motions are less damaging than tectonic motions, given the same spectral intensity of shaking. This result may be consistent with the findings of Hough (2014), who used public responses to the USGS's *Did You Feel It?* web portal from 11 events to suggest that shaking intensities, as quantified by Modified Mercalli Intensity, were less severe in induced events when compared to tectonic events of similar magnitude. Atkinson et al. (2018) further examined trends in *Did You Feel It?* responses and found that intensities from induced motions were lower than tectonic motions beyond 10 km from the epicenter, but were similar at closer sites. The lower intensities were attributed to focal-depth effects from these shallow events (Hough, 2014; Atkinson, et al., 2018).

Here, the ground motion characteristics and the earthquakes that produced the records in our two suites are examined to understand why the induced motions appear to be less damaging. First, the influence of ground motion frequency content and significant duration is explored. We also examine earthquake and tectonic factors that may explain differences in frequency content between the induced and tectonic motions, such as focal depth, stress drop, and attenuation.

2.6.1 Ground Motion Parameters

The extent to which ground motion characteristics can explain the differences in collapse response of the baseline model between the two ground motion sets is investigated using

multivariate regression and analysis of variance (ANOVA) procedures. The Akaike Information Criteria (AIC) is used for model comparison in the ANOVA. AIC measures the relative quality of a regression model based on the goodness-of-fit, with a penalty for the number of variables included in the regression, and ultimately recommends the model with lowest AIC value (Sakamoto, et al., 1986). Therefore, this analysis can be used to identify variables that do not aid significantly in the multivariate regression. (Note that this analysis is pursued to examine trends in collapse capacity with respect to ground motion characteristics, not for the purpose of developing a predictive statistical model.)

The primary ground motion parameters considered are frequency content and significant duration, due to their well-documented effect on structural response, e.g. (Mahin, 1980; Baker & Cornell, 2006; Baker, 2011; Raghunandan & Liel, 2013; Chandramohan, et al., 2016). In addition, we introduce a binary flag indicating if the ground motion is induced or tectonic, to investigate whether this distinction has a significant influence on the observed collapse capacities. Frequency content of each records is quantified by the ratio of Sa(T=0.3s) to Sa(T=0.5s), which effectively measures the decrease in spectral energy from T=0.3 seconds to T=0.5 seconds. This parameter captures the frequency content in the range of interest when the chimney period elongates under inelastic response. A larger Sa(T=0.3s)/Sa(T=0.5s) value indicates a steeper spectrum, and the induced motions are steeper (this difference is illustrated in Figure 2.7). Recall Figure 2.1(e) that the significant durations of the induced set are slightly shorter.

The first significant result of the statistical analysis is that the ANOVA excludes the binary flag variable differentiating between induced and tectonic motions from the statistical model for predicting collapse capacity (also, the p-value for the flag in multivariable regression was 0.44). Thus, the ANOVA indicates that the distinction between the induced and tectonic motions is not

important from the perspective of structural response, except to the extent this distinction affects ground motion frequency content and duration.

Accordingly, for further investigation we combine the data sets from the induced and tectonic motions. Figure 2.8(a) shows the collapse capacity assessed for each ground motion, quantified at Sa(T=0.26s), as a function of the frequency content parameter for that same ground motion. The trend line is the multivariate linear regression from a model including frequency content and significant duration, showing that motions with steeper spectra (higher Sa(T=0.3s)/Sa(T=0.5s)), primarily the induced motions, have greater collapse capacities because of lower spectral energy affecting the structure's nonlinear response.

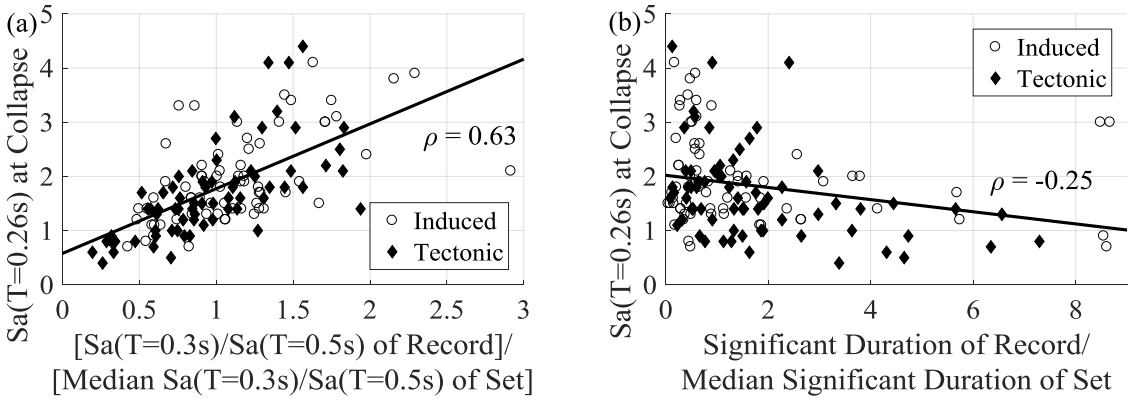

Figure 2.8. Collapse capacity at Sa(T=0.26s), plotted against (a) frequency content (normalized as shown) and (b) significant duration (also normalized) for induced and tectonic motions. The solid line is the linear regression model for induced and tectonic results together.

The best model identified by the AIC included Sa(T=0.3s)/Sa(T=0.5s) and significant duration. In the ANOVA analysis, both Sa(T=0.3s)/Sa(T=0.5s) and significant duration are normalized by their medians. In Figure 2.8(b), the collapse capacity of each record is plotted as a function of significant duration. Longer duration motions are associated with slightly lower collapse capacities, as illustrated by the negative slope of the trend line. The correlation coefficients between Sa(T=0.3s)/Sa(T=0.5s) and significant duration compared to Sa(T=0.26s) at

collapse are 0.63 and -0.25, respectively, indicating that frequency content is a much more important predictor of collapse. Other studies, e.g. (Raghunandan & Liel, 2013; Chandramohan, et al., 2016), have demonstrated that extended shaking durations produce more cycles of vibration, and can lead to failure at lower intensities. Since the structures considered are brittle, cyclic deterioration was not considered in models; more ductile structures showing more significant deterioration may be more sensitive to ground motion duration.

Earthquake magnitude is found to be the strongest predictor of Sa(T=0.3s)/Sa(T=0.5s). This signifies that the magnitude of the earthquake is the most significant source parameter to consider when investigating expected collapse capacity for a brittle structure. Larger earthquakes will result in a higher probability of collapse. However, since both the induced and tectonic ground motion suites have the same median magnitudes (Figure 2.1), further investigation into other earthquake source characteristics is needed to examine their impact on the observed differences in frequency content.

The question remains, why do the induced ground motions selected have different frequency content than the tectonic ground motions? Recall that these sets were selected to have similar magnitude and distance distributions, and these factors do not explain the different frequency contents. Rather, these differences appear to stem from two other differences between the ground motion sets: between induced and tectonic motions, and between ground motions from the central and eastern U.S. (CEUS) (represented in the induced set) and those from the western U.S. (represented in the tectonic set). Induced motions tend to be somewhat shallower than tectonic earthquakes; this depth variation is evident in our record set (Figure 2.1) and has also been observed in broader ground motion datasets (Assatourians & Atkinson, 2018; Atkinson, et al., 2018). In addition, there is some evidence that stress drop, which controls the strength of high-

frequency ground motion, differs between induced and tectonic motions. For the CEUS, induced earthquakes tend to have a lower stress drops than tectonic records with similar depths (4-8 km range) (Atkinson, et al., 2018). The difference from stress drop considering induced and tectonic motions in the CEUS are compared in Figure 2.9 by examining two response spectra: one generated using Yenier & Atkinson (2015b) for tectonic motions in the CEUS and a second generated using Novakovic & Atkinson (2018) for induced motions in Oklahoma. The tectonic CEUS spectrum has more energy at all periods due to a larger expected rupture depth and therefore a larger stress drop. In addition, there are important documented differences in stress drops between the western U.S. and the CEUS, with the western U.S. tending to be lower than the either CEUS tectonic or induced events (Yenier & Atkinson, 2015b). This comparison is also examined in Figure 2.9 by comparing the two CEUS spectra to the Yenier & Atkinson (2015b) developed for California. Here, the differences in spectral shape can be attributed to the regional tectonic environments, rupture depths and stress drops. Comparing Yenier & Atkinson (2015b) for California and Novakovic & Atkinson (2018) for Oklahoma in Figure 2.9 provides representative spectra of the two ground motion sets used for dynamic analysis in this study and align well with the corresponding spectra shown in Figure 2.7.

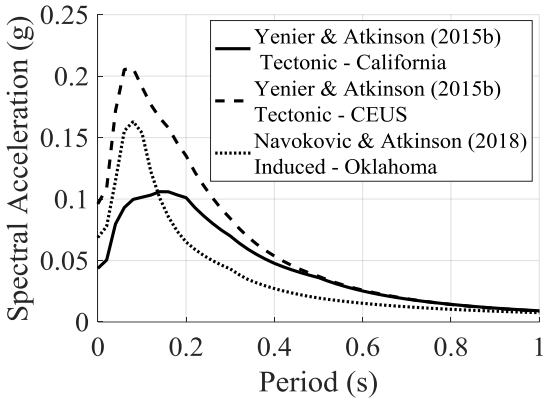

Figure 2.9. Example response spectra for induced and tectonic motions using Novakovic & Atkinson (2018) and Yenier & Atkinson (2015b) ground motion prediction equations (GMPEs), respectively. In both cases, we used M_W 4.4 and R_{rup} = 10 km as input. GMPE inputs such as depth and $Vs_{,30}$ are taken as the values described from the properties for the induced and tectonic sets in Figure 2.1. Stress drops are calculated using the recommended equations in Novakovic & Atkinson (2018) (66 bars), Yenier & Atkinson - California (2015b) (36 bars) and Yenier & Atkinson - California (2015b) (109 bars).

Additionally, another potential factor for differences observed in frequency content is induced earthquakes tend to have faster energy attenuation with distance than tectonic motions (in either CEUS and western U.S.). Yenier & Atkinson (2015b) note attenuation to be a significant factor when describing the differences between the western U.S. and CEUS calibrations for their GMPE. Furthermore, Novakovic & Atkinson (2018) also note a modified attenuation model for their GMPE which was based on the same framework as Yenier & Atkinson (2015b). The modifications between these different GMPE models suggest that geometric attenuation varies between the western U.S. and CEUS, as well as between induced and tectonic earthquakes. This energy decay also is observed comparing induced and tectonic earthquakes considering PGA and MMI (Atkinson, et al., 2018), and at Sa(T=0.2s) and Sa(T=2.0s) (Moschetti, et al., 2018). Although, Moschetti et al. (2018) found the decay to be more significant for shorter spectral periods, the lesser energy at both periods for induced earthquakes can still explain some differences in frequency content. In total, these trends seem to indicate that there are quantifiable differences

between tectonic western U.S. motions and induced CEUS motions that indicate slightly less damageability from the induced motions. However, more research is needed to separate the influence of region seismological environment factors from the distinction between induced and tectonic ground motions on structural fragility.

2.7 DISCUSSION AND IMPLICATIONS

This study quantifies the differences in seismic response of brittle structures, subjected to ground motions from induced and tectonic (natural) earthquakes. The study employs a nonlinear simulation model based on the flexural response of an unreinforced masonry residential chimney, which is subjected to two sets of ground motions: a set of motions recorded from induced earthquakes in Oklahoma and Kansas, and a set of tectonic (not induced) motions selected to be as similar as possible to the induced set. In addition, a set of eight other brittle structures, differing from the baseline model in terms of stiffness, strength and deformation capacity, are also analyzed under the two sets of motions. Structural response is assessed using incremental dynamic analysis and quantified primarily by collapse capacity.

The findings show that, given the same spectral shaking intensity level, the induced motions are associated with a 23% smaller probability of collapse of a brittle structure than the tectonic motions. Sensitivity analyses indicate that the differences between the effects of induced and tectonic motions are more significant for the more ductile structures, suggesting that different frequency content of the induced and tectonic motions contributes to the different collapse capacities obtained. Statistical analysis confirms that differences in frequency content is the primary factor contributing to the trends in collapse capacities, with differences in duration of shaking being of secondary importance.

The differences in frequency content between induced and tectonic records seem to stem from the differences in focal depth, stress drop, geometric attenuation and tectonic environment between the two record sets. In particular, the induced motions have higher stress drops than the tectonic set, which are primarily from the western U.S., and faster attenuation with distance. Furthermore, differences between the tectonic environments in the western U.S. and CEUS contribute largely to the observed differences in frequency content as shown in Figure 2.9. Lastly, differences in geometric attenuation between induced and tectonic earthquakes could also be responsible for differences in spectral intensities. Earthquakes producing future ground motions with these characteristics may also be somewhat less damaging than ground motions from crustal environments that have been more researched. However, more work is needed to confirm these trends.

CHAPTER 3

3 SEISMIC LOSS AND DAMAGE IN LIGHT-FRAME WOOD BUILDINGS FROM SEQUENCES OF INDUCED EARTHQUAKES

3.1 INTRODUCTION

Activities related to oil and gas production, especially the deep disposal of wastewater, have been responsible for an uptick in seismicity in parts of the U.S. In particular, induced seismicity in Oklahoma and southern Kansas has dramatically increased the seismic hazard, e.g. (Petersen, et al., 2016), and, correspondingly, the risk to infrastructure in the region, e.g. (Liu, et al., 2017). This increase in seismic activity is of concern due to the region's building stock, much of which was not designed with seismic design principles, as well as evidence that even relatively small magnitude events can produce damage and economic impacts (Barba-Sevilla, et al., 2018). The largest event to date in Oklahoma, the September 3rd, 2016, Pawnee earthquake (M_W 5.8) caused damage that included cracking and partial collapse of an unreinforced masonry and brick façade, as well as minor damage to light-frame wood residential homes (Knife Chief, 2017). The town experienced a number of smaller earthquakes after the mainshock, including 63 earthquakes with magnitudes ranging from M_W 2.5 - 3.6 (12 earthquakes with $M_W > 3.0$) in the next month (USGS, 2017).

The induced seismicity observed in Oklahoma and southern Kansas differs from the earthquakes more generally studied by earthquake engineers. The induced earthquakes, occurring since about 2009, have been generally of low magnitude (no greater than M_W 5.8 to date), but relatively frequent. Earthquake rates increased substantially from 2009 until 2015, with 888 $M_W \geq$ 3.0 earthquakes occurring in 2015, compared to only 130 experienced in California in the same year (USGS, 2017). More recently, earthquake rates have decreased somewhat, with over 400 M_W

≥ 3.0 earthquakes in Oklahoma in 2017. Unlike tectonic events, these earthquakes typically occur in swarms, i.e. seismic sequences where multiple earthquakes occur in a short time frame (Keranen, et al., 2008; Llenos & Michael, 2013). These sequences occur due to the migration of injected fluids and associated pore water pressures along already critically stressed faults. The response of buildings and infrastructure to low magnitude earthquake sequences, and the potential for damage accumulation, is not well understood.

Yet, a recent survey of 233 Oklahoma homeowners found that 43% of Oklahoma residents have reported some amount damage from induced earthquakes, with 18% reporting damage costing $1000 or more (Tracy & Javernick-Will, 2018). 33% of those surveyed reported that they believed their residences experienced accumulated damage over multiple earthquakes. Homeowner and activist groups have also asserted that damage is accumulating in these series of smaller earthquakes more than might be expected, expressing concerns about each earthquake increasing vulnerability of the structure in subsequent events (Kansas Sierra Club, 2017). For example, one respondent to the U.S. Geological Survey 'Did you feel it?' site wrote "The cracks just keep getting bigger… They are destroying my house little at a time" (Quitoriano & Wald, 2017). Another resident stated: "I'm worried the next one would bring my house down on top of me." (Trapasso, 2017). Insurers have also acknowledged that "accumulation of loss from property…. for earthquake scenarios" is now a "realistic possibility" (Barrett, 2016).

This study aims to quantify damage to and seismic losses for light-frame wood buildings when subjected to sequences of smaller magnitude events. Three research questions are investigated. First, what damage can we expect in light-frame wood construction in induced earthquakes? Second: how does this damage change if the building experiences an earthquake sequence? Finally, are these results consistent with observations from Oklahoma to date? To

conduct this investigation, one and two-story multifamily wood frame buildings are designed, and their seismic response dynamically simulated using three-dimensional (3D) nonlinear models subjected to recorded ground motion sequences from induced earthquakes. Damage is quantified through seismic losses, which are estimated using the FEMA P-58 methodology (FEMA, 2012), in order to quantify damage and losses to the building even when damage to the structural system itself may be limited. To address the impact of earthquake sequences, we also examine how expected losses and building vulnerability will accumulate and/or change over a sequence of earthquakes, and compare damages observed in past events to the simulation results.

3.2 LITERATURE REVIEW

3.2.1 Effect of Induced Earthquakes on Buildings and Infrastructure

Research has shown that induced seismicity increases the seismic hazard, and that this increase can be meaningful in the range of ground shaking intensities that matter for building response. For example, Petersen et al. (2018) show a 130-fold increase in likelihood of shaking of Sa(T=0.5s) = 0.25g compared to a seismic hazard forecast that does not include induced seismicity. In another study of Oklahoma using a different hazard model framework, Grigoratos et al. (2018) found elevated seismic hazard for the region, due to the contribution from induced earthquakes. Similar trends have been observed elsewhere, for induced seismicity associated with hydraulic fracturing and gas production (Schultz, et al., 2017; Bommer, et al., 2017). By convolving the hazard model from Petersen et al. (2016) with assumed fragility models for collapse and the threat to life safety from falling hazards, Liu et al. (2017) found that this increased seismic hazard also elevated these risks substantially compared to the baseline natural seismicity.

There have been fewer studies examining the fragility and response of buildings in induced earthquakes, because of the smaller magnitude of the events that have been experienced to date. Chapter 2 found that, for brittle structures such as residential brick chimneys, induced motions were less damaging when compared to similar tectonic records for a given spectral intensity. However, this study also suggested that these differences stem largely from differences in frequency content. Hence, they conclude that a large magnitude induced earthquake could invoke a similar response to a tectonic earthquake. Potential damage to bridges in Oklahoma and Texas have been investigated by Harvey et al. (2018) and Khosravikia et al. (2018), respectively. Harvey et al. (2018) concluded that slight to moderate damage is possible to bridges in induced earthquakes by subjecting a finite element bridge model to scaled records of the 2016 Pawnee Earthquake. Khosravikia et al. (2018) developed fragility curves for different damage states of Texas bridges subjected to both induced and tectonic motions. The study found that there was a greater chance of experiencing slight or moderate damage in Texas bridges when induced seismicity is considered, compared to considering just the natural seismicity

3.2.2 Seismic Response of Light-Frame Wood Buildings

Light-frame wood construction comprises the majority of the building stock across the United States. Historically, light-frame wood buildings have performed well in earthquakes with a relatively low risk of catastrophic collapse and life endangerment. However, there is potential for high seismic losses; the 1994 Northridge Earthquake caused an estimated property loss of $20 billion to light-frame wood construction (in 1994 dollars) (Kircher, et al., 1997).

In part as a response to this damage, there have been multiple large efforts, including the CUREE Caltech Woodframe Project (Folz & Filiatrault, 2004) and the NEESWood Capstone Test

(Pei, et al., 2010), to improve understanding of seismic response of these structures and develop tools to aid in the quantification of their seismic response. For example, in NEESWood, Van de Lindt et al. (2010) tested a full-scale six-story light-frame wood residential building on a shake table at the University of Buffalo - SUNY. The study quantified damage in a structure which also included nonstructural finishes such as gypsum wallboard. Damage was observed in the form of cracks to the gypsum wallboard, but no structural damage was observed, even at the maximum considered earthquake (MCE) level. Likewise, Ellingwood et al. (2008) investigated the performance of residential light-frame wood construction in regions of low to moderate seismicity. They concluded that: "typical residential building construction in the central and eastern U.S. is quite robust under significant earthquake ground motions and that … economic losses are likely to be of more concern than threat to life safety." Filiatrault et al. (2002) showed that it is critical to incorporate the effects of nonstructural components in seismic performance assessments of these buildings, as they can significantly change the expected stiffness, strength, and fundamental period of the building. More recently, projects such as the Applied Technology Council (ATC) 116 (2018), have investigated the performance of many short period structures, including light-frame wood construction, in areas of high seismic hazard. That study shows that light-frame wood buildings have good collapse resistance.

Analytical tools have also been developed from experimental testing, through the CUREE Caltech Woodframe Project and the NEESWood Capstone Test and others. Software such as Cyclic Analysis of Shear walls (CASHEW) (Folz & Filiatrault, 2001) and Seismic Analysis of Woodframe Structures (SAWS) (Folz & Filiatrault, 2004) were developed as part of the CUREE Caltech Woodframe Project. More recently, SAPWood (van de Lindt, et al., 2009) and Timber3D (Pang, et al., 2012) has improved upon the earlier tools. Christovasilis (2010) also developed

numerical models from the NEESWood testing for two-dimensional shear walls. SAPWood and Timber3D feature nonlinear shear wall elements with model parameters calibrated to experimental testing results in order to capture the hysteretic response of the shear walls and can capture large deformations of near collapse level response. They have been shown to reasonably capture the response of light-frame wood buildings in full-scale shake table tests (van de Lindt, et al., 2009).

3.2.3 Damage Accumulation

Earthquake engineering performance assessments are often based on the assumption that the building is in an undamaged state when an earthquake occurs. However, this assumption may be unrealistic in certain context. For example, in cases of seismic swarms and mainshock-aftershock sequences, there may not be enough time for retrofit or repair of the structure before the next shaking event, and so the building's damage and response may be influenced by what happened in a preceding event. As a result, there are some documented historical cases in which a building withstood an initial larger magnitude earthquake only to collapse in a smaller magnitude at a later time (Decanini, et al., 2000; Çelebi, et al., 2010).

Structural damage accumulation has been researched extensively. Both Ballio and Castiglioni (1994) and Amadio et al. (2003) examined multiple earthquake loadings on linear and nonlinear numerical models of single-story steel structures and single-degree-of-freedom (SDOF) structures, respectively. Both studies quantified damage using a q-factor (ductility) and compared ductility demand between varying earthquake loadings, finding that damage accumulation was greater for systems with a higher ductility capacity. More recently, Ghosh et al. (2015) developed a probabilistic framework for predicting damage accumulation in highway bridge columns, using the Park & Ang (1985) damage index to quantify damage. Considering cases of multiple

mainshocks and a mainshock followed by aftershocks, the study found that there was a significant increase in damage index exceedance probabilities within each scenario's time frame. Jalayer & Ebrahimian (2017) conducted a similar study which investigated cumulative damage to aftershocks in reinforced concrete buildings while considering the time-dependent rate of aftershock occurrence. The study found significantly higher damage risk estimates when considering a structure damaged initially by a mainshock or a mainshock plus an additional aftershock.

Mainshock-aftershock studies have also examined damage accumulation, and the effect of a first event increasing vulnerability in subsequent events. For example, Hatzigeorgiou and Liolios (2010) examined the impact of mainshock-aftershock sequences on reinforced concrete frame structures. Ultimately, the study observed more cumulative damage from earthquake sequences when compared to singular events of the same intensity. Likewise, Raghunandan et al. (2015) examined multiple reinforced concrete moment frame structures designed to current code standards subjected to mainshock-aftershock sequences. Their work showed that collapse capacity of a structure was not significantly influenced if a mainshock did not significantly damage the structure. However, if the building was extensively damaged in the mainshock, the collapse capacity dropped significantly. These findings have been confirmed by a number of others (Tesfamariam, et al., 2015; Shokrabadi & Burton, 2018). Simulations by Shokrabadi and Burton (2018), also applying to reinforced concrete frames, but looking at other limit states, found that even a slightly damaging mainshock could decrease a structure's ability to remain occupiable by up to 75% in the subsequent event. Looking specifically at light-frame wood buildings, Nazari et al. (2013) simulate response of a two-story residential frame structure subjected to artificial mainshock-aftershock sequences. They showed that the structure's fragility increased when

subjected to multiple seismic pulses, but not to the extent that has been observed with other studies focusing on other structure types (i.e. steel or reinforced concrete). Goda and Salami (2014) also investigated mainshock-aftershock sequences on light-frame wood construction, showing that aftershocks led to 5–20 % increase of the median inelastic seismic demand curves when the structure was initially subjected to a moderate damage state. The literature on this topic also emphasizes the need to carefully model in-cycle and cyclic deterioration and P-Δ effects to accurately capture these effects (Chandramohan, et al., 2016; Raghunandan & Liel, 2013).

These results show that damage accumulation in multiple earthquake sequences plays a major role in quantifying damage and seismic loss. Seismic loss has been identified as the key seismic performance measure for light-frame wood construction. This study aims to investigate how sequences of induced earthquakes may impact performance of light-frame wood construction.

3.3 GROUND MOTION SELECTION

This study incorporates recorded ground motions from confirmed induced earthquakes in Oklahoma and southern Kansas for dynamic analysis. These ground motions are obtained from the Rennolet et al. (2018) database. Real seismic sequences are selected to better capture the effects of these earthquakes on buildings. In particular, Ruiz-Garcia & Negrete-Manriquez (2011) found that mainshock-aftershock studies that generate synthetically-created sequences can overestimate the damage observed from the multiple motions.

The Rennolet et al. (2018) database includes more than 300,000 motions recorded in the region. These motions were filtered and processed according to the recommendations of NGA-West2 (Ancheta, et al., 2013). For engineering analysis, we were interested in identifying the highest intensity records that form two or three motion sequences in this dataset. To do so, first, a

record with a high (i.e. highest available in database) geometric mean of peak ground acceleration in the two orthogonal directions (or PGA) is selected as a target, and a time window of 15 days before and 15 days after is defined. All earthquakes within this time window and with an epicenter within a 25 km radius of the event producing the target record are then considered for selection of motions to form a sequence. These temporal and spatial constraints are intended to ensure that these sequences are consistent with the observed seismicity, but we place no restrictions on the recording station being the same, due to practicality and the need for records of interest for engineering analysis. Ultimately, the two records with the largest (1) earthquake magnitudes and (2) PGAs in the window are selected to combine with the first target record to create a three-record sequence, maintaining the same order as the events occurred. All of the selected motions in each sequence are from earthquakes with $M_W > 3.0$ and have geomean PGAs > 0.05g. There is no overlap of motions between different sequences. Following this search criteria, 19 sequences each comprised of three motions are selected, or 57 total motions, with each motion having two horizontal components.

Figure 3.1 provides a summary of the ground motion suite characteristics. For the entire ground motion set, the median earthquake magnitude is M_W 3.46, the median PGA is 0.10 g, and the median significant duration (5-95% Arias Intensity) is 1.91 seconds. *SaRatio*, which quantifies spectral shape (Eads, et al., 2016) as a ratio of the spectral acceleration at the first mode period divided by the average Sa over a period range, is shown for two period ranges 0.3s to 0.9s and 0.5s to 1.5s.

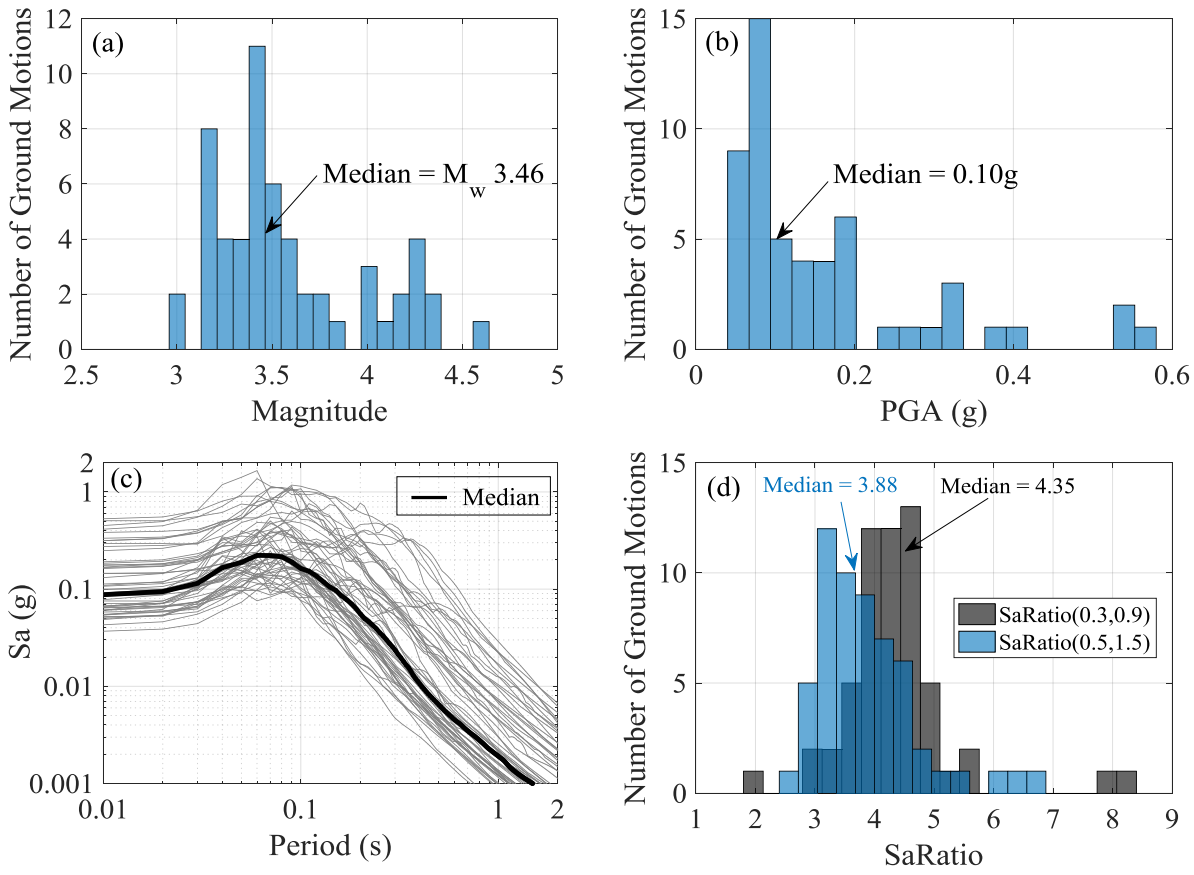

Figure 3.1. Summary of the ground motion characteristics for all 57 induced motions collected showing (a) earthquake magnitudes, (b) geomean PGA, (c) geomean acceleration response spectra for all motions, and (d) histograms showing the range of *SaRatios* for two period ranges, i.e. *SaRatio(0.3,0.9)* and *SaRatio(0.5,1.5)*.

3.4 BUILDING ARCHETYPES AND DESIGN

Light-frame wood construction is prevalent across Oklahoma, and the one and two-story building archetypes analyzed here are chosen to be representative of the typical building stock in the Oklahoma region. The buildings examined in this study was originally designed for "moderate seismicity" in accordance with ASCE 7-10 for the ATC 116 project by that project team (ATC, 2018). Here, "moderate seismicity" refers to locations at the upper limit of seismic design category (SDC) C, referred to as "C_{max}", and corresponding to a short-period response acceleration parameter (S_{DS}) of 0.50g (ASCE, 2010; FEMA, 2009). Oklahoma and southern Kansas fall in SDC

B, so we redesigned the buildings for a location with S_{DS} of 0.26g using the same wall layouts (for both shear walls and nonstructural partitions) as the original models. In the redesign, shear wall lengths were decreased and nail spacing was increased to reduce the building strength. In addition, we compared design wind forces for Edmond, OK to the SDC B seismic forces, and we designed for the larger (controlling) seismic forces.

The design of each multifamily residence covers a 14.6 m by 29.3 m (48 ft by 96 ft) footprint; this design accommodates six 7.3 by 9.8 meter (24 by 32 foot) apartment units adjacent to one another in the one-story building, as shown in Figure 3.2 and Figure 3.3. The layout of shear walls in the two-story archetype accommodates four two-story 7.3 m by 14.6 m (24 ft by 48 ft) townhouses adjacent to each other. The exterior walls (both archetypes), shown in Figure 3, are framed with 5x15 cm (2x6 in) lumber and have OSB sheathing. The exterior faces are clad in siding. We assumed James Hardie type siding, rather than the stucco assumed in ATC 116, because stucco is an uncommon finish material in Oklahoma (Authentic Custom Homes, Homes by Taber LLC, Silver Custom Homes, & Sun Custom Homes, 2018). This decision is important, as finishes and siding materials can have a pronounced impact on the seismic response of the structure (Filiatrault, et al., 2002). In particular, stucco is stiffer and heavier than siding. The interior face of the exterior walls is clad with 1.3 cm (1/2 in) gypsum wallboard. The interior shear walls (party walls) are actually two lines of 5x10 cm (2x4 in) framing separated by a 2.5 cm (1 in) gap, which would in reality be a larger corridor, finished with gypsum wallboard on the face of the wall toward the interior of the unit, but with no sheathing applied to the corridor face, to represent a typical framing scenario. The foundation for both archetypes is a 5 cm (4 in) concrete slab on grade, with spread footings at the interior posts and reinforced grade beams integral with the slab at the perimeter and along all interior load bearing walls. For the 2-story archetype, the floor system is

framed with 5x10 cm (2x4 in) in parallel chord trusses, spaced at 61 cm (24 in) on center. More detailed descriptions of the SDC C_{max} building designs are provided in ATC 116 (ATC, 2018).

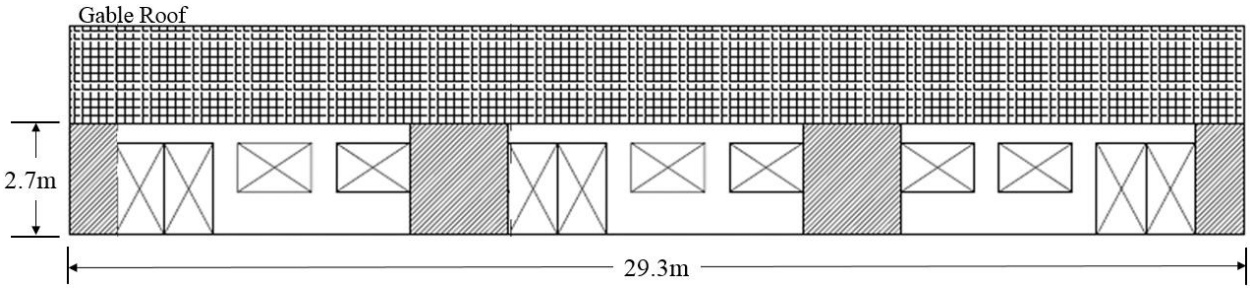

Figure 3.2. Elevation view of the one-story multifamily wood frame archetype used in this study (modified from ATC 116 (ATC, 2018).

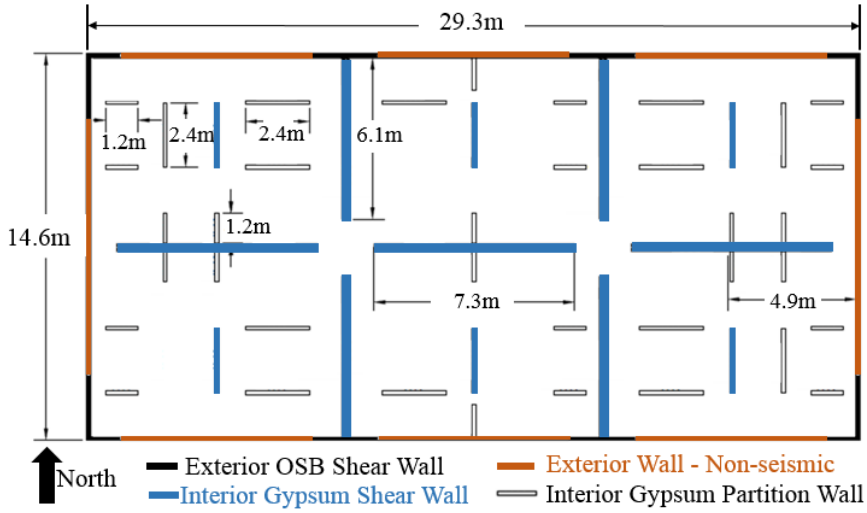

Figure 3.3. Plan view of the shear wall and bearing wall layout for the one-story multifamily wood frame archetype (modified from ATC 116 (2018)).

3.5 BUILDING MODELING

The building is modeled using Timber3D, a nonlinear structural analysis software for wood frame construction based in MATLAB that was developed by Pang et al. (2012) and Pang & Shirazi (2013). The software is intended for simulating seismic responses of 3D light-frame wood construction systems by representing individual wood frame elements and the interaction of their responses. Timber3D is capable of providing estimates of collapse level horizontal and vertical

displacements. Timber3D improves upon the so-called lumped parameter approach *SAWS* (Folz & Filiatrault, 2004) and *SAPWood* (Pei & van de Lindt, 2011), by employing a finite element methodology with nodal condensation and shape functions to decrease the required computational energy. In addition, Timber3D is formulated to capture vertical uplift forces present in light-frame wood shear walls, as well as large displacements in flexible diaphragms. The goal of this study is to simulate seismic response of wood light frame construction and examine the sensitivity of response to sequences of earthquakes, i.e. effects of multiple loading cycles. Thus, it is particularly important to capture cyclic and in-cyclic degradation to quantify loading cycle effect (Chandramohan, et al., 2016; Raghunandan & Liel, 2013; Raghunandan, et al., 2015; Amadio, et al., 2003). It is also important to capture large deformations and geometric (P-delta) effects, e.g. (Mahin, 1980), in order to simulate side-sway collapse in the first story, the predominant failure mechanism in light-frame wood structure (Pang, et al., 2012; Ghehnavieh, 2017). These models are adapted from models from ATC 116, provided by Ghehnavieh (2017).

In our models of the building archetypes, nonlinear behavior is modeled only in the wall elements. Wall elements include both the shear walls, which in the design are taken to be the sole lateral force resisting system in the structure, and the interior partition walls. Figure 3.4(a) and (b) show the hysteretic characteristics for 1.2 m by 3 m (4 ft by 10 ft) sections of an exterior shear wall and interior shear wall, respectively, illustrating the model's treatment of strength and stiffness deterioration, in-cycle and cyclic deterioration, and pinching effects. These hysteretic plots show the nonlinear response for the wall without any nonstructural finishes, the effect of which are shown in Figure 3.4(c) for the nonstructural exterior (James Hardie) siding. In Timber3D, these elements are assigned at the same location such that the composite wall response accounts for structural and nonstructural contributions. The hysteretic model that defines the

response of the nonlinear wall elements and finishes (except for the siding) is a modification to the Modified Stewart Hysteretic Model developed by Ghehnavieh (2017). The model parameters for each individual wall element represents cyclic wall behavior as a function of wall length, nail spacing, and stud spacing, and are based on parameters calibrated to experimental results. The Modified Stewart Hysteretic Model was developed during the CUREE tests (Folz & Filiatrault, 2001) based on experimental testing of wood shear walls under quasi-static loading. The modified model (Ghehnavieh, 2017) employed here follows the same hysteretic behavior, but fits an "S" curve to the post peak response, instead of a linear degradation, to capture a nonlinear strength decay and better represent residual strength observed at large displacements in wood-frame shear walls. The difference between the two models can be seen by comparing Figure 3.4(a) and Figure 3.4(c). Siding was modeled using the original Modified Stewart Hysteresis Model.

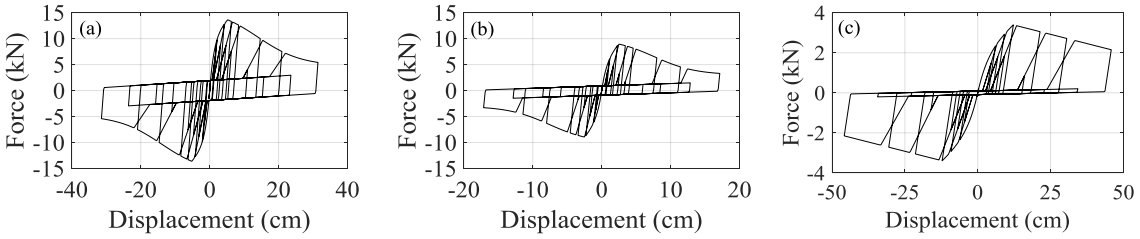

Figure 3.4. Force vs. displacement hysteresis of 1.2 m wide by 3 m tall (4 ft by 10 ft) sections of (a) an exterior OSB shear wall, (b) an interior gypsum shear wall, and (c) nonstructural exterior siding found in the one and two-story buildings.

The concrete foundation, sill plates, stud elements, and floor diaphragms are modeled as elastic elements, while the hold downs, anchor bolts, and soil elements are all modeled to be rigid. Koliou et al. (2016) showed that modeling the diaphragm of a single-story wood-frame structure was essential in accurately capturing some buildings' responses in terms of drifts and accelerations. In this study, the diaphragms are modeled to be elastic, but very stiff (consistent with ATC 116). We judge a near rigid diaphragm to be reasonable here because of the large number

of walls (structural and nonstructural), which limit the role of a flexible diaphragm. The base of the structure is modeled with multiple elements to simulate the effects of hold downs, anchor bolts, sill plates, the concrete foundation, and even the surrounding soil, as shown in Figure 3.5. Here, the result is an effectively fixed base. This condition is consistent with the base of the models used in ATC 116.

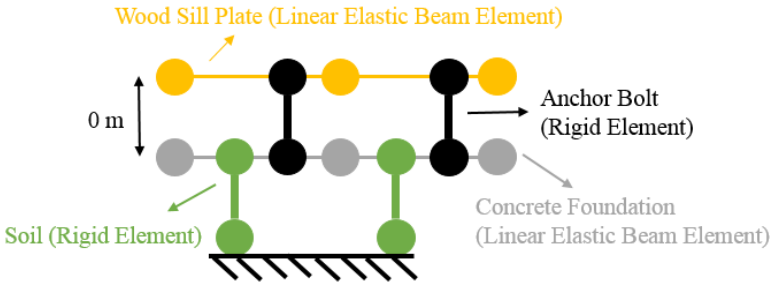

Figure 3.5. Base elements for archetype models, showing the wood sill plate, hold downs, anchor bolts, concrete foundation, and soil elements.

Timber3D's formulation also captures large geometric deformations and corotational effects, which together with modeling of hold down and contact forces between the framing members (Pang & Shirazi, 2013) enables simulation of large vertical displacements as side-sway collapse occurs. We define collapse by the downward (vertical) displacement of the second floor exceeding 25 cm (10 in). Results are not very sensitive to the exact definition of vertical displacement corresponding to collapse, as at this point, lateral and vertical displacements are increasing without bound.

In accordance with other previous studies, e.g. (Pang & Shirazi, 2013; van de Lindt, et al., 2009), we applied 1% Rayleigh damping to the first and second modes (E-W and N-S lateral directions) of the buildings. This damping is applied to represent linear damping and ensure that movement of the structure from the first motion in the sequence dies out before the next ground motion was applied, and to capture elastic damping. However, in Timber3D, damping can only be

applied to all or none of the elements, so the value is kept low to avoid overdamping in the nonlinear range.

The fundamental periods of the one and two-story archetypes are 0.29 and 0.45 seconds, respectively. Figure 3.6 compares the pushover curves for both buildings, compared to the design base shear. The design base shears differ in the two directions because OSB shear walls (R = 6.5) comprise the lateral force resisting system in the E-W direction and gypsum shear walls (R = 2) govern the N-S direction (ASCE, 2010). The two-story building is stronger than the one-story building, but also somewhat less ductile. As Figure 3.6 also reveals, the ultimate strength of the buildings is much higher than the design base shears. This overstrength stems from the contribution of nonstructural partition walls and nonstructural finishes in the models.

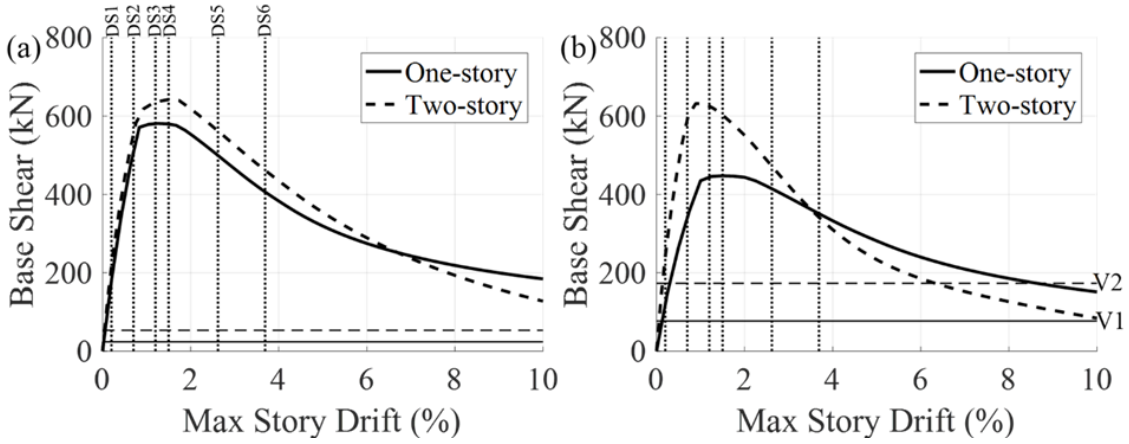

Figure 3.6. Pushover curves for the one and two-story buildings considering a distributed loading according to first mode shape in (a) the E-W direction and (b) N-S direction. The drifts corresponding to the global damage states are labeled in (a) and described in more detail in Table 3.1. V1 and V2 in (b) represent the design base shear for the one and two-story buildings, respectively.

3.6 DAMAGE ASSESSMENT METHODOLOGY

3.6.1 Damage and Loss Definitions

We define damage as any seismic loss. Structural damage is associated with losses to structural components, i.e. interior and exterior shear wall elements. The nonstructural components

considered include electrical, HVAC, and plumbing among others. Seismic loss is quantified using the Seismic Performance Prediction Program (SP3) (Haselton Baker Risk Group, LLC, 2018). SP3 adopts the FEMA P-58 (2012) methodology to organize building fragilities, component fragilities, population information, and other inventories to probabilistically estimate seismic losses.

3.6.2 Damage in Single Event

To examine damage and losses in induced earthquakes, we first run all 57 individual motions in an incremental dynamic analysis (IDA) of the undamaged buildings (Vamvatsikos & Cornell, 2002). In this IDA, each record is scaled up by increasing the spectral acceleration at the fundamental period of the structure, $Sa(T_1)$, and rerunning the motion until collapse occurs. Motions are scaled based on the maximum $Sa(T_1)$ of the two horizontal components of the ground motion. The peak story drift ratios (SDR), floor accelerations, and residual drifts are recorded at nine nodes at each floor to capture torsional effects. A one-second cushion of zero acceleration was added to the end of each ground motion, and residual drifts were calculated as the average over that second. This residual drift calculation allowed for residual drift to be calculated after the earthquake motion had ceased; although the building does not completely come to rest in this second, the average provided very similar results to test cases with a longer buffer at the end, while saving computational time. In this 3D analysis, the intensity measure (IM) is the maximum $Sa(T_1)$ of the two components of each record. We randomly assign one of the motions to the N-S direction, and the other to the E-W.

3.6.3 Damage in Sequence of Events

To explore how damage and seismic loss occur in sequences of motions, we create artificial sequences from the identified ground motions with different scaling combinations, as illustrated in Figure 3.7. For each sequence, the first motion is scaled such that the building just reaches damage state (DS) *i*. These damage states (DS), are defined to correspond to different story drift ratios (SDR), as shown in Figure 3.6, similar to Raghunandan et al. (2015) and Ryu et al. (2011). The definitions of these damage states are taken from SP3 (Haselton Baker Risk Group, LLC, 2018), and correspond to the median SDR at which damage occurs for the two shear wall types that are present in each archetype, as defined in Table 3.1. These damage states are used solely for defining the scale levels for the first motion in the sequence.

Table 3.1. Global damage state and associated SDRs, together with a qualitative damage description.

Damage State	Structural Element	SDR (%)	Qualitative Description
DS1	Exterior Shear Walls	0.2	Screws popping out, minor cracking of wallboard, warping or cracking of wallpaper
DS2	Exterior Shear Walls	0.7	Moderate cracking or crushing of gypsum wallboards (typically in corners and in corners of openings)
DS3	Exterior Shear Walls	1.2	significant cracking and/or crushing of gypsum wallboards and the buckling of studs and tearing of tracks
DS4	Interior Shear Walls	1.5	Slight separation of sheathing or nails that come loose
DS5	Interior Shear Walls	2.6	Permanent rotation of sheathing, tear out of nails or sheathing
DS6	Interior Shear Walls	3.7	Fracture of studs, major sill plate cracking

This first scaled motion is combined with a second motion that is scaled in an IDA to create a sequence, with a 20 second buffer between the motions to allow the structure to come to rest. The second motion in the sequence is scaled by $Sa(T_1)$ as described above, creating a family of sequences, each reaching the same DS in motion 1, but with different scale factors on motion 2. We note here that studies have shown that the polarity of the two motions can change the results of analysis in sequences due to the interactions between the directions of maximum response, nonlinear deformations, and residual drifts with the polarity of the subsequent motion (Luco, et al., 2004). We applied the motions as recorded, assuming polarity was random.

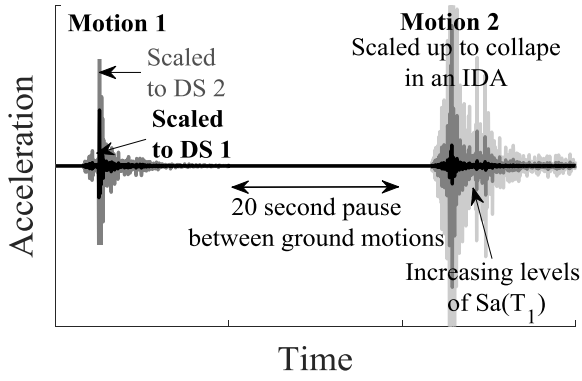

Figure 3.7. Illustration of sequences of motions examined, showing scaling of motion 1 to a DS of interest, and the IDA applied to motion 2.

We also created some three-motion sequences, following a similar procedure to that shown in Figure 3.7. In this case, the first motion is scaled such that the building just reaches DS *i*. The second motion is scaled such that the building just reaches DS *i+1*. The third motion is scaled through IDA, and 20 second pauses are added between the motions. Only the two-story building was subjected to the three-motion sequences. For that building, results were very similar for the two and three-motion sequences, which is consistent with findings from Raghunandan et al. (2015), who found that the path to a particular damage state is not critical in considering multiple sequences. For this reason, only the single and two-motion sequences were applied to the one-

story building. Building response in two-motion and three-motion sequences are investigated in more detail later in this study.

3.7 HAZARD-CONSISTENT IDA METHODOLOGY

One shortcoming of IDA is the bias in terms of spectral shape that can be produced from scaling ground motions above the level at which they were recorded, producing ground motions that are inconsistent with the hazard and have unrealistic frequency content (Vamvatsikos & Cornell, 2002; Baker & Cornell, 2006). This presents a difficulty here, because of our interest in examining earthquakes and ground motions beyond the levels that have been experienced. Methods such as multiple stripe analysis (MSA) use different ground motion sets for different intensity levels to account for this inconsistency with respect to seismic hazard (Jalayer F. , 2003). Recently, Chandramohan (2016) developed a structural reliability framework that can produce hazard-consistent results while using a generic set of ground motions in an IDA. In this methodology, spectral shape and ground motion duration are used to adjust the results of a generic IDA to represent realistic ground motion characteristics. This study employs the framework developed by Chandramohan (2016) to adjust engineering demand parameters or EDPs (namely, SDR, floor accelerations, residual drifts and collapse capacities) obtained from the IDA to account for the expected spectral shape at a typical Oklahoma site. We adjust EDPs to account only for spectral shape, which is quantified the dimensionless parameter, *SaRatio* (Eads, et al., 2016); we do not account for ground motion duration because this parameter was not found to be critical for the EDPs of interest (Chapter 2). *SaRatio* is defined as $Sa(T_1)$, normalized by Sa_{avg}. where Sa_{avg} is the average of the spectral accelerations across a range of periods (Eads, et al., 2015). Although Eads et al. (2015) recommend a period range of $0.2T_1$ to $3T_1$, we instead use T_1 to $3T_1$ because

higher modes are not important for our short period buildings of interest. A higher *SaRatio* indicates a more peaked spectrum at the T_1 of interest, meaning that a ground motion with a lower *SaRatio* is often more damaging to a structure responding in the nonlinear range. *SaRatio* is selected as the parameter to represent spectral shape due to its higher efficiency compared other metrics, such as epsilon, as shown in Chandramohan (2016). Furthermore, hazard information for *SaRatio* is easily attainable from spectral acceleration based ground motion prediction tools and Sa-based hazard tools are easily adaptable for *SaRatio*.

The hazard-consistent IDA methodology involves, first, quantifying the expected spectral shape at a site of interest, and then adjusting the generic IDA results to be consistent with that expected shape (Chandramohan, 2016). To quantify the expected spectral shape, we examine the deaggregated hazard from the USGS's 2018 one-year forecast, which includes induced seismicity (Petersen & Shumway, 2018), for Edmond, Oklahoma. This deaggregation information includes magnitude (M), rupture distance (R), epsilon (ε), and percent contribution for different earthquake scenarios at nine different hazard levels of interest at Sa(T=0.3s) and Sa(T=0.5s) (geometric mean of horizontal components). For this purpose, we assume site conditions are at the boundary between site class B and C (V_{s30} = 760 m/s). One note of inconsistency is the Sa(T_1) taken from USGS deaggregation are for the geomean of the two horizontal components while the IDA scaling in this study was scaled by the maximum component to be consistent with the DS in Table 3.1. This inconsistency translates into a potential under estimate of EDP in the hazard-consistent analysis. We do not anticipate this discrepancy to have a significant influence on the results reported. At each hazard level, hazard-consistent target *SaRatios* were calculated for each archetype at multiple hazard levels using the procedure outlined in Chandramohan (2016) and the

Atkinson (2015) ground motion prediction equation (GMPE). Table 3.2 shows the calculated target *SaRatio* and associated $Sa(T_1)$ for each hazard level for the one and two-story buildings.

Table 3.2. Deaggregated hazard information and implications for $Sa(T_1)$ and SaRatios at periods corresponding to one-story and two-story buildings.

	One-Story Building					**Two-Story Building**				
Hazard Level Return Period [years]	**Mean M_W**	**Mean R [km]**	**Mean ε**	**Sa(0.3s) [g]**	**Median Target *SaRatio (0.3,0.9)***	**Mean M_W**	**Mean R [km]**	**Mean ε**	**Sa(0.5s) [g]**	**Median Target *SaRatio (0.5,1.5)***
75	5.7	16.8	0.7	0.51	4.1	5.9	21.7	0.6	0.27	3.7
275	5.8	13.8	1.1	0.97	4.5	6.0	16.0	1.0	0.51	3.8
475	6.0	13.1	1.1	1.2	4.6	6.1	14.6	1.0	0.65	3.9
975	6.0	12.4	1.3	1.6	4.8	6.2	14.2	1.2	0.88	4.1
2475	6.1	10.8	1.6	2.2	5.1	6.3	12.3	1.4	1.2	4.4
4000	6.2	10.9	1.6	2.5	5.3	6.4	12.1	1.5	1.5	4.7
6000	6.2	10.4	1.7	2.8	5.6	6.5	12.6	1.6	1.7	4.9
8000	6.2	10.3	1.8	3.0	5.8	6.5	12.5	1.7	1.8	5.0
10000	6.3	10.2	1.9	3.2	5.9	6.5	12.4	1.7	1.9	5.2

These results show that the expected spectral shape is very peaked in Edmond (as indicated by *SaRatios* >> 2); for comparison, a typical expected shape in San Francisco at the same periods would be *SaRatio(0.3,0.9)* = 2.1 and SaRatio*(0.5,1.5)* = 2.4 for the 2475-year return period. This peaked shape stems from the high values of epsilon, the number of standard deviations by which an observed logarithmic spectral acceleration differs from the mean logarithmic spectral acceleration produced by a GMPE (Baker & Cornell, 2006), which increase significantly for the longer return period hazard levels. Furthermore, the peaked spectra are a function of the Atkinson (2015) GMPE, which is calibrated for shallow crustal earthquakes in the eastern and central United States, and agrees well with the spectral shapes of the ground motions used in this study, shown in Figure 3.1(c) and (d). In this induced context, the expected magnitudes and distances remained relatively constant, so the more extreme shaking is driven from variability in the ground motion, given these earthquake characteristics. The mean *SaRatio(0.3,0.9)* of all 57 induced ground

motions is 4.35 for the one-story building and the mean *SaRatio(0.5,1.5) is* 3.88 for the two-story building, as shown in Figure 3.1(d). In general, the target SaRatios (either *SaRatio(0.3,0.9)* or *SaRatio(0.5,1.5)*) are larger than the SaRatios of the record set (with exception of the 75 and 275-year return periods). This trend indicates that the records used in the IDA are less peaked than the expected *SaRatio* for Edmond determined from deaggregation.

Although these *SaRatios* imply that the motions used are very peaked, the deaggregation shows that in fact the rarer events would be even more peaked than the motions used in our analysis. To obtain more records with lower *SaRatios*, we also ran the generic IDA with the FEMA P-695 Far-Field set (FEMA, 2009), consisting of 22 pairs of records, and combined the results with the 57 motions from induced events. The FEMA Far-Field set has a range of *SaRatio(0.3,0.9)* of 0.9 to 2.5 and *SaRatio(0.5,1.5)* of 1.1 to 4.5. Records with lower *SaRatio* were analyzed to provide a broader range of *SaRatio* to inform predictions of structural response considering records with a reasonable range of frequency content.

The hazard-consistent IDA approach adjusts EDPs of interest from the generic IDA results using regression analysis (Zhong & Deierlein, 2018). Specifically, a linear regression analysis is carried out between each EDP (at each hazard level) in natural logarithmic space between the EDP and the *SaRatio* parameter for the motions used in the IDA (including both the FEMA and induced motions in this case), as shown in Figure 3.8(a). The results of this regression, illustrated in Figure 3.8(b), are used to produce a median EDP prediction that is conditioned on the target *SaRatio* at each hazard level. An example of the multiple curves for all the hazard levels and their associated intensities is shown in Figure 3.8(b). The solid dots on each line in Figure 3.8(b) show the target *SaRatio(0.3,0.9)* and corresponding hazard-consistent EDP for that hazard level. We carried out

this regression for three EDPs in each of the two directions (SDRs for each story, residual drifts, and collapse capacities) at 9 hazard levels, for both buildings.

Floor accelerations were not adjusted to be hazard-consistent. Our results showed that the R^2 for regression of floor accelerations versus *SaRatio* are very low. These poor correlations occur because the peak accelerations from the induced records occur early in the time history, in the first few seconds of strong shaking, when the building is still elastic, due to the short duration and pulse-like characteristics of these motions, such that floor accelerations are not dependent on spectral shape. Interestingly, peak floor accelerations in the longer duration FEMA Far Field motions occurred at different points throughout the time history, sometimes after the structure had entered the nonlinear range, showing more dependency on *SaRatio*.

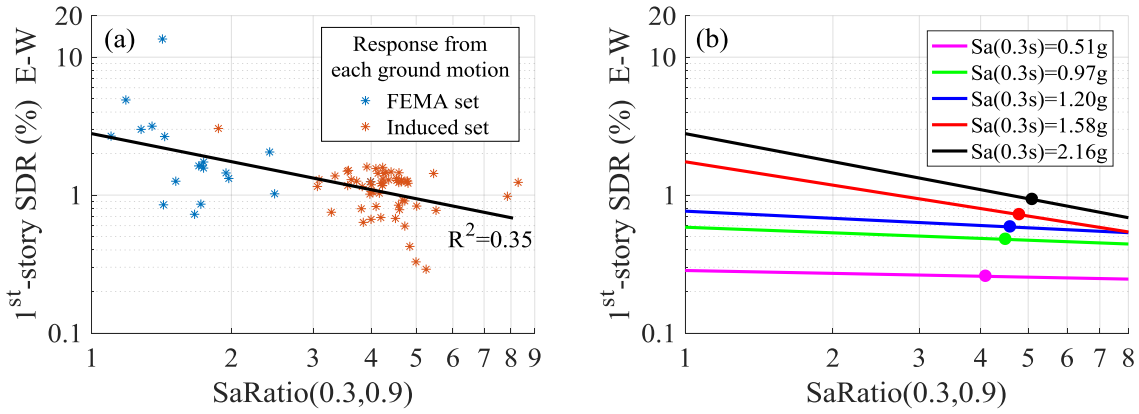

Figure 3.8. Illustration of hazard-consistent IDA adjustment for the one-story building showing (a) regression between first-story SDR (E-W direction) and *SaRatio* at the 2475-year hazard level (Sa(0.3s) = 2.16g), and (b) regressions for the same EDP at five different hazard levels (75 to 2475 years). The solid dots on each line in (b) show the target *SaRatio(0.3,0.9)* and corresponding hazard-consistent EDP for that hazard level.

We also quantify the uncertainty in the obtained EDP, considering the record-to-record variability, i.e. the uncertainty in the regression. As shown in Chandramohan (2016) and (Zhong & Deierlein, 2018), the uncertainty of the EDP conditioned on *SaRatio* for each hazard level is calculated using Equation 3.1:

$$\sigma = \sqrt{\frac{RSS}{N_{gm}-2}} \tag{3.1}$$

where RSS is the sum of the squares of the residuals, N_{gm} is the number of ground motions used in the analysis, and 2 represents the number of unknown coefficients in the regression equation. We also examined how the uncertainty in the target *SaRatio* might influence our assessment of the uncertainty in the EDP. Ultimately, the uncertainty in the target ratio (on the order of 0.2 for a logarithmic standard deviation) was small and not found to significantly influence the results.

The median IDA curves from the first story drift for the one and two-story buildings are shown in Figure 3.9. In both buildings, the hazard-consistent drifts are less than the predicted drifts for a given intensity. This trend occurs because the target *SaRatio* at almost all hazard levels is greater than the median *SaRatio* of the record set used in the IDA. The more peaked a spectrum is expected to be, the lower the estimated drifts.

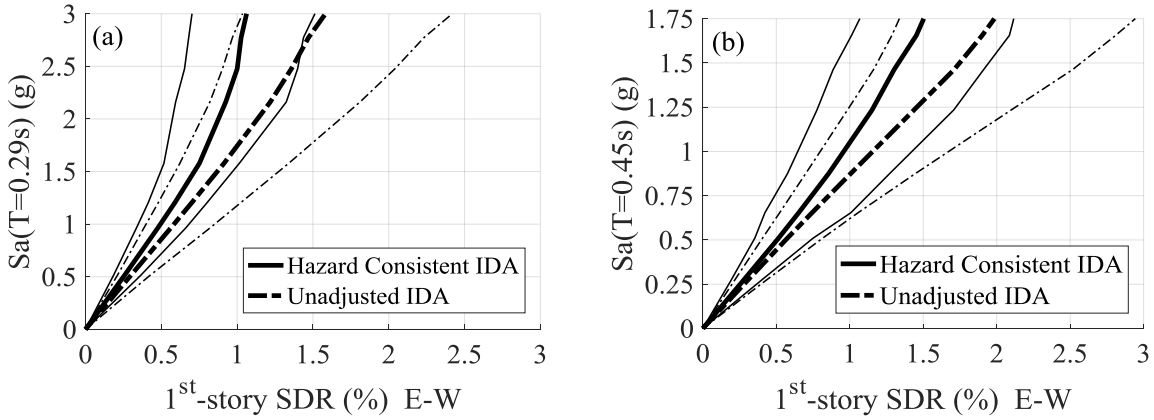

Figure 3.9. Median first-story SDR showing both the hazard-consistent IDA results and the unadjusted results for (a) the one-story building and (b) the two-story building. Median (bolded) and ± the standard deviation (thin) curves are shown in all cases.

For loss assessment, SP3 takes as input a vector of structural analysis results for each hazard level and EDP of interest. This vector traditionally includes the structural response results for each

ground motion run in the analysis. Here, the median EDP and σ are used to produce 1000 EDP realizations for each hazard level. These realizations provide the basis for SP3's Monte Carlo simulations.

3.8 DAMAGE TO BUILDINGS IN A SINGLE EVENT

Figure 3.10(a) shows the total expected seismic loss for the one-story building, normalized by the replacement cost of the building, for both the induced motion IDA (unadjusted) and the hazard-consistent IDA analysis. For the purpose of the normalization, the total replacement cost is taken to be approximately $788,000 and excludes the cost of demolition. Figure 3.10(b) breaks down this total loss by component category for both the analyses. The shear walls had the highest contribution to losses at all intensity levels. This damage sustained by shear walls is characterized by cracking of the gypsum wallboard at lower intensity levels and includes fracturing of the sill plates and studs at higher intensity levels. Nonstructural components, such as plumbing and HVAC systems, sustained the second most damage, in the form of leaks and piping support failures, at intensity levels below Sa(T=0.29s) = 2.5g. At intensity levels above Sa(T=0.29s) = 2.5g, losses due to residual drift became the second largest contributor to the total loss, after the losses sustained in the shear walls. When residual drifts exceed 1%, the analysis deems the building as needing to be demolished, producing a high contribution to the total seismic loss.

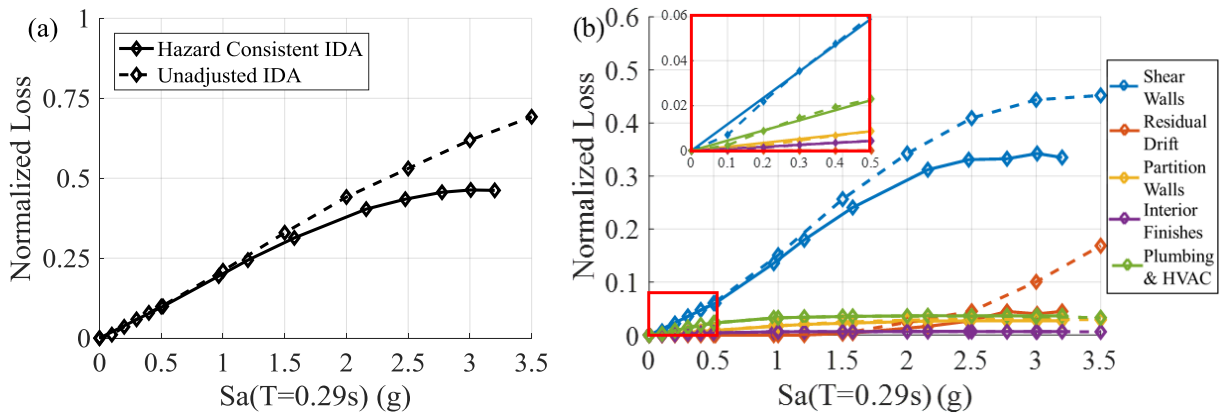

Figure 3.10. Normalized expected losses for the one-story building showing: (a) total expected loss and (b) breakdown of the total loss by component type.

At lower intensities (e.g., Sa <1.5), the hazard-consistent IDA and the unadjusted IDA provide similar results, as shown in Figure 3.10(a). This similarity occurs because the spectral shape (*SaRatio*) of the induced ground motion set is very close to the target *SaRatio*, and because the structure is not responding significantly in the nonlinear range, so results are not very dependent on *SaRatio*. However, at higher intensities, the hazard-consistent IDA predicts lower losses. This trend occurs because the target *SaRatios* calculated in Table 3.2 are all larger than the mean of the induced record set, suggesting that the expected spectra is less damaging than those used in the analysis, so the adjustment to hazard-consistency lowers the EDPs (Figure 3.9) and, as a result, losses.

Figure 3.11(a) shows the total expected seismic losses for the two-story building. For this plot, this total replacement cost is $1.5 million. Figure 3.11(b) shows the breakdown of this total losses by component category, which follows similar trends to those observed for the one-story building. At higher intensity levels (e.g., Sa(T=0.45s) > 1.5g), losses from residual drift became the highest contributor to the total loss. Residual drifts are much higher overall in the two-story model, due to the first-story's P-Δ driven response affected by loads in the upper story.

Losses in the one and two-story buildings are compared in Figure 3.12. At a given hazard level, the expected normalized seismic loss of the one-story building is higher than the two-story building at hazard levels below the 4000-year return period. In this range, drifts in the one-story building are very similar to the two-story building, but the variability is greater. At return periods above 4000 years, losses due to residual drift and collapse increase the potential losses for the two-story building. In particular, the higher seismic mass and multiple stories increases the chance for a first-story P-Δ driven collapse compared to the one-story building at these larger return periods.

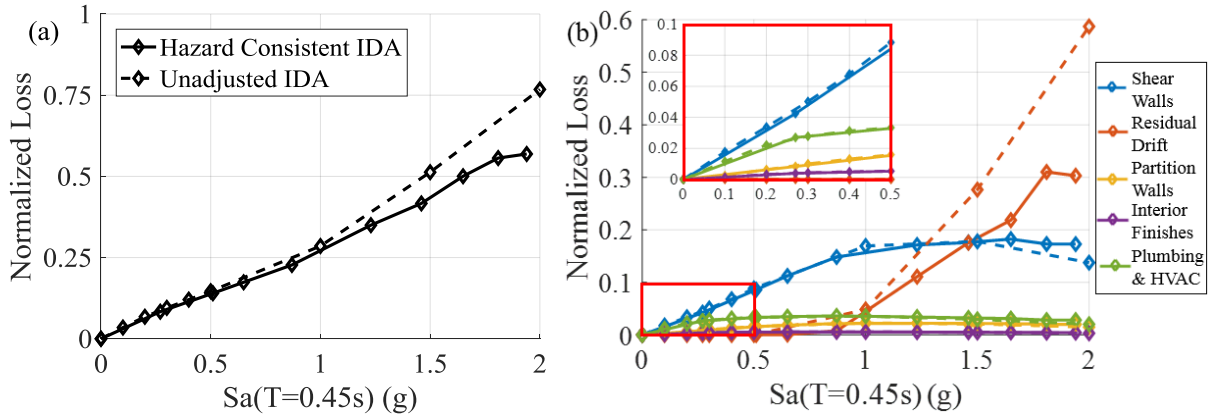

Figure 3.11. Normalized expected losses for the two-story building showing: (a) total expected loss and (b) breakdown of the total loss by component type.

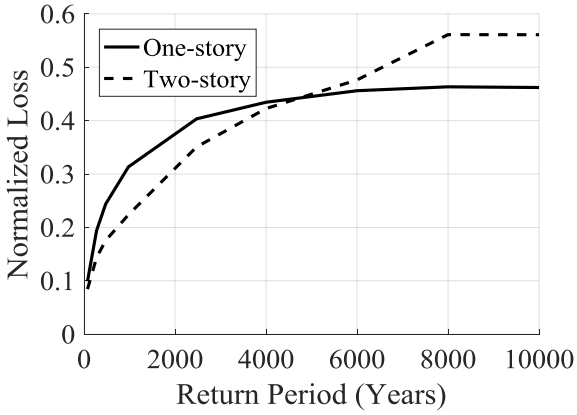

Figure 3.12. Normalized expected losses for the one and two-story buildings.

We can compare the simulation results to damage observed in two recent earthquakes in Oklahoma: the 2016 M_W 5.8 Pawnee earthquake and 2016 M_W 5.0 Cushing earthquake. In the first event, the USGS Shakemap estimated that Pawnee, OK experienced intensities between Sa(0.3s) = 0.28g and 0.35g (USGS, 2016). The Cushing earthquake was about two miles from Cushing, and the two closest stations, OK914 (One mile from the epicenter) and OK915 (2.5 miles from the epicenter), reported Sa(T=0.3s) of 0.2g and 0.5g, respectively (Taylor, et al., 2017). The damage reported to light-frame wood buildings in the two earthquakes was very similar. In the Pawnee Nation, which borders Pawnee, damage included cracking to shear walls and partition walls, ceiling cracks, broken windows, foundation damage, brick chimney failure, and damage to exterior finishes, such as mortar deterioration and cracking, brick façade cracks and spalling, and awning damage (Knife Chief, 2017). Additionally, in Pawnee, residents reported damage similar to that in Pawnee Nation (Sewell, 2017). In Cushing, Taylor et al. (2017) reported "damage was limited to nonstructural components, mainly partition wall cracks in corners and near openings… There were few observed instances of structural damage to light frame wooden structures". This report also documented damage to finishes in light-frame wood structures, such as gypsum wallboard, occurred at drifts at or below 0.2%. The damage reported by Taylor et al. (2017) is mapped in Barba-Sevilla et al. (2018).

Here, the observed damage to buildings in the Pawnee and Cushing earthquakes is compared to the results from this study's analysis. In Figure 3.13(a), expected seismic losses in the one-story building are superimposed with the USGS estimated intensities for the Pawnee earthquake, and the measured intensities in the Cushing earthquake. Our assessment predicts minor damage to the shear walls, plumbing, HVAC, and partition walls. For the same intensity range, Figure 3.13(b) shows the estimated percent of exterior shear walls in each DS, as calculated in the

loss assessment using SP3. These DS are described in Table 1. For the shaking intensities of interest in Pawnee, the model predicts that approximately 15 – 20% of the exterior shear walls are expected to be in DS 1, i.e. screws popping, minor cracking, etc., and a very small fraction of the shear walls would be expected to be in DS 2, i.e. moderate cracking or crashing of wallboards, or DS 3. Similarly, 10 – 27% of the exterior shear walls are expected to be in DS 1 if intensities similar to the Cushing earthquake are observed. These expected damage results again agree reasonably well with the reported damage from the Pawnee and Cushing earthquakes. In Pawnee, in the days immediately following the earthquake, four insurance claims totaling $24,000 had been paid out to homeowners, with the largest claim being $21,000 (Jones, 2016). These were for single family residential homes, which carry a median policy limit of $168,000 as determined by the Oklahoma Insurance Commission as of 3/17/2017 (Oklahoma Insurance Commisson, 2017). If this limit is approximated to be the total cost of the home, a total normalized loss of 5 – 15% ($8,000 – $24,000) is estimated for our models. This loss agrees reasonable well with initial payouts in Pawnee.

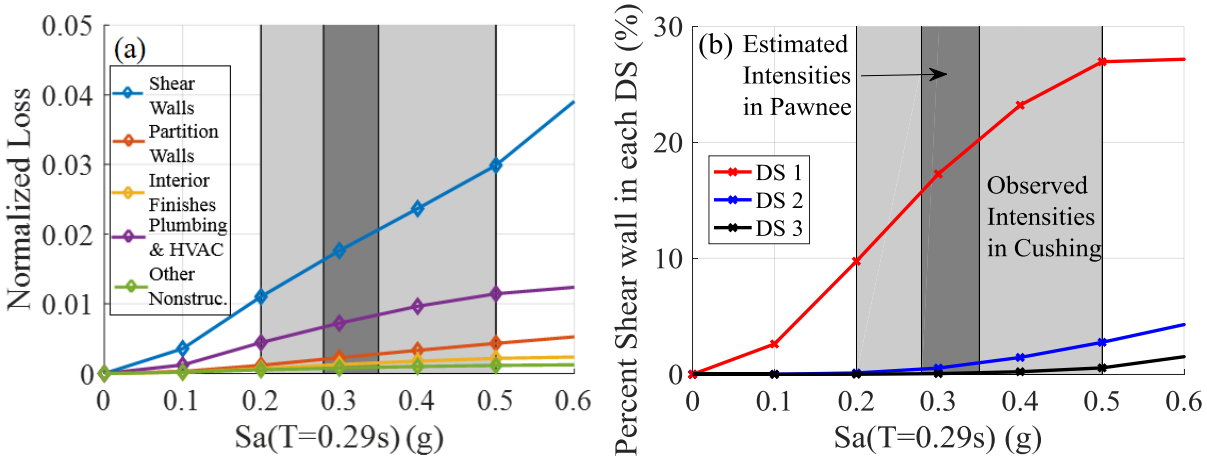

Figure 3.13. Expected losses for the one-story building showing (a) breakdown of the total loss to quantify contributions from different types of components and (b) percent of exterior shear walls in each damage state for the component, overlaid with estimated intensities observed in the Pawnee, OK M_W 5.8 and in the Cushing, OK M_W 5.0 Earthquakes.

3.9 DAMAGE ACCUMULATION AND RESPONSE OF BUILDINGS IN SEQUENCES OF MOTIONS

We next examine damage and responses of the buildings from the two- and three-motion sequences. For the purposes of this discussion, we define damage accumulation as additional damage (i.e., loss) that a building sustains in a second ground motion, compared to damage that is sustained from a ground motion of the same intensity when the building is undamaged (i.e., damage in the first motion). This accumulation, if it occurs, stems from additional seismic vulnerability of the already damaged building. SDR is used to investigate damage accumulation as it has been shown by numerous studies, e.g. (Raghunandan, et al., 2015; Ryu, et al., 2011; Nazari, et al., 2013), as a good indicator of increasing seismic vulnerability. Figure 3.14 provides the first set of insights into accumulating damage, comparing the average maximum SDR, as a function of spectral acceleration, for different levels of initial damage. When the building is initially damaged to DS4, the response is very close to the undamaged building; similar results (not shown) are observed for the lower DSs. However, a building that is initially damaged to DS5 or DS6 has a much different response in a second motion than the undamaged structure and showed some accumulation of damage in the following ground motion. This finding suggests that in order to see a difference in building response from the undamaged structure a building must be severely damaged in the prior event. Studies of other kinds of buildings, including concrete, steel, and light-frame wood, have also reached this same conclusion (Raghunandan, et al., 2015; Li & Ellingwood, 2007; Nazari, et al., 2013). Figure 3.15 shows fragility curves for the one and two-story buildings relating the probability of reaching DS1-4 to $Sa(T_1)$. DS3 and DS4 have a low probability to be reached given the observed intensities in Oklahoma (Figure 3.13), suggesting that accumulation of damage is unlikely for these structures. Figure 3.15(b) also shows the fragility curve for DS4

for the two-story building initially damaged to DS3 in a two-motion sequence (red curve). The fragility is very similar to the DS4 curve for the undamaged building and reflects the findings shown in Figure 3.14. (Note that these results and those that follow do not consider the hazard-consistent adjustments. Figure 3.10 and Figure 3.11 showed that the hazard-consistent adjustments did not make significant changes at the more frequent intensities of the most interest, i.e. the lower end of the curve.)

Figure 3.14 also compares the response from the two and three-motion sequences at varying initial damage states. There is very little difference in building response between the two- and three-motion sequences. This trend was true for buildings initially damaged to DS1-6 and is consistent with Raghunandan et al. (2015), who found that the preceding DS was critical for subsequent response, but not the path to the DS. Due to similarities in responses, we focus on results from two-motion sequences in the remainder of this section.

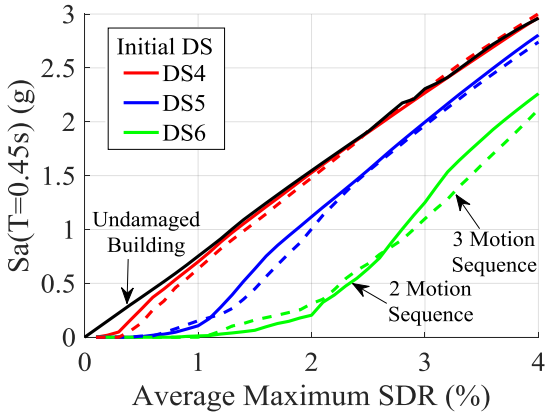

Figure 3.14. Effects of initial damage on response of the two-story building showing average maximum SDR for the last motion in the two- and three-motion sequences, as a function of ground motion intensity.

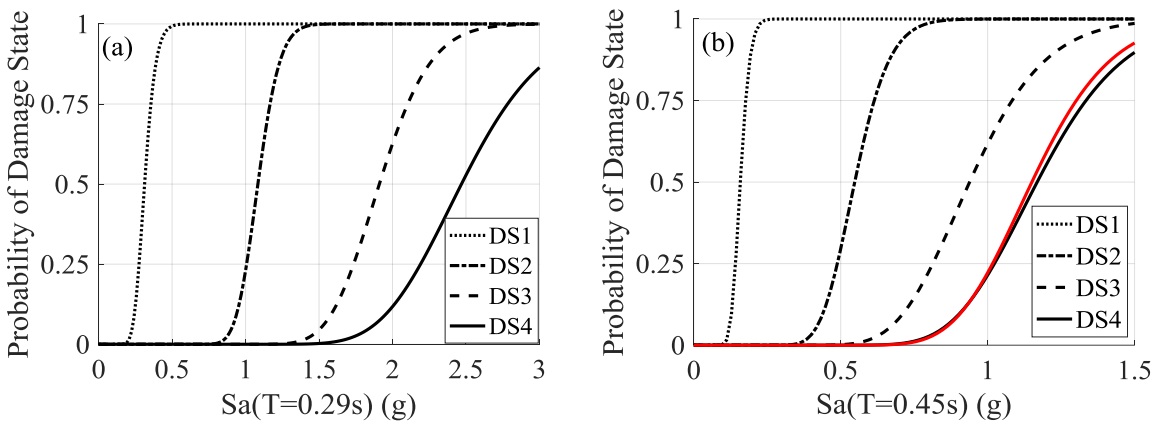

Figure 3.15. Fragility curves for the (a) one-story building and (b) two-story building showing the probability of reaching DSs 1-4, given $Sa(T_1)$. The red curve in (b) shows the fragility for DS4 for a the two-story initially damaged to DS3 in a two-motion sequence.

Figure 3.16(a) shows the expected losses for the one-story building in a two-motion sequence when the building is repaired at the end of the sequence, as a function of the ground motion intensity of the first and second motions. The symmetry of the surface about the horizontal axes shows that damage accumulation was not significant because a second motion of the same intensity as a first motion causes the same losses. Thus, Figure 3.16(a) shows that expected losses are a function only of the maximum intensity observed, rather than the sequence of intensities. We do not observe damage accumulation because buildings need to be pushed deep into the nonlinear range in the first motion before their vulnerability to seismic loss in subsequent motions is significantly affected. However, Figure 3.16(b) shows the expected losses if the building were to be repaired (to its undamaged state) after each motion in the sequence. As expected, if the building is repaired after each earthquake, the losses are much higher than if the building is repaired just once after the sequences. Even though damage is not amplifying vulnerability, homeowners affected by these sequences would be still be experiencing amplified seismic losses.

In addition, the absence of damage accumulation by this definition does not mean that cracks in walls do not grow during subsequent motions in the sequence. Van de Lindt et al. (2010)

found that cracks in gypsum wallboard lengthened and widened in successive earthquakes in a full-scale shake table test. Figure 3.17 shows the length and location of cracks in three successive shaking tests. The cracks increase in length in after each shaking event. Yet, the seismic loss may not increase because the cost of repairing gypsum wallboard with minimal cracking compared to slightly more cracking is the same (FEMA, 2012).

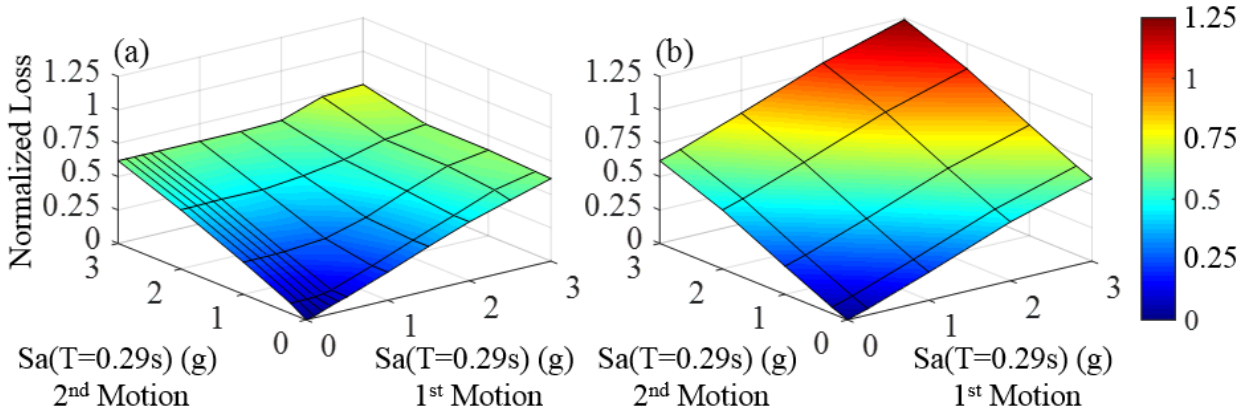

Figure 3.16. Expected normalized loss for the one-story building subjected to two-motion sequences considering (a) repair at the end of the sequence and (b) repair after each motion in the sequence.

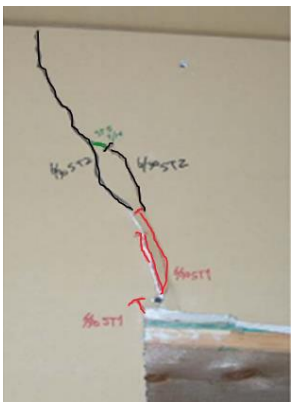

Figure 3.17. Photo from van de Lindt et al. (2010) showing elongation of cracks between first, second and third shaking tests. Red cracks are the first shaking test, black are the second test, and green is the third shaking test.

To investigate in more detail how the second motion may be altering the building's damage, Figure 3.18(a) shows an example two-motion sequence for the one-story building. The first motion is scaled to Sa(T=0.29s) = 0.35g and the second earthquake is scaled to Sa(T=0.29s) = 0.4g. This scenario was chosen because it is representative of a seismic sequence of two motions with similar intensities to those observed in Cushing and Pawnee. The largest drift (and loss corresponding to 7.4% of the building value of $788,000) was reached in the first ground motion. In the second ground motion, the building did not exceed the drifts in the first motion. The maximum response occurred in the first motion, so the total losses are unchanged (unless the building was repaired between the two motions). The largest contributor to loss is determined to be the cracking of paint over fasteners or joints at approximately $4000 in losses. For this same sequence, Figure 3.18(b) shows a damage index developed by Park and van de Lindt (2009), which is very similar to the Park & Ang (1985) damage index, but is calibrated for light-frame wood buildings, specifically with gypsum wallboard shear walls, through the NEESWood experimental tests. This damage index is a function of the maximum drift during loading, the ultimate drift during monotonic loading, the yield drift, the absorbed hysteretic energy, and properties of the shear walls such as nail spacing and height-to-width ratio. As shown in Figure 3.18(b), the damage index for the building increases in the second motion, indicating that the structure is more damaged. This result is largely a function of the inclusion of absorbed hysteretic energy in the damage index, which increases in the second ground motion. Nevertheless, this result shows that damage is worsening in subsequent events, even though assessment of vulnerability and repair costs (losses) do not pick this up. These patterns likely explain residents' concerns about multiple events. As one respondent reported to the USGS 'Did you Feel it?' site "there is a continuation of

cracks in walls from previous large quakes. I have repaired them only to have new ones appear 6 months later when another quake hits" (Quitoriano & Wald, 2017).

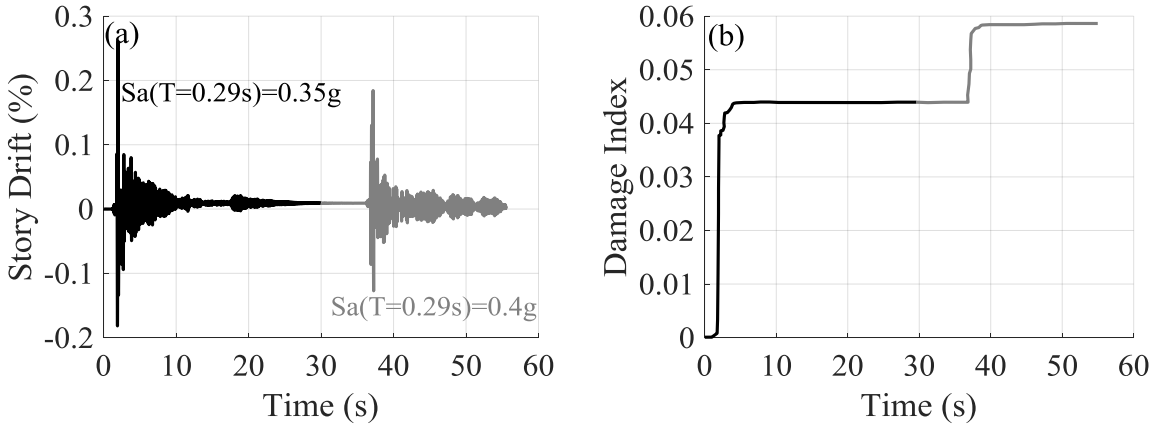

Figure 3.18. Example two motion sequence, showing evolution of (a) story drifts and (b) the Park and van de Lindt ((2009)) damage index over time for the one-story building.

3.10 CONCLUSIONS

This study quantifies damage to and seismic losses for light-frame wood buildings when subjected to induced earthquakes like those experienced in Oklahoma and Kansas, which have to-date been small to moderate magnitudes, but sometimes occur in swarms. One and two-story multifamily wood frame buildings are investigated by dynamically simulating their seismic response using three-dimensional (3D) nonlinear models which are subjected to recorded ground motion sequences from induced earthquakes. Damage is quantified through seismic losses, which are estimated using the FEMA P-58 methodology (FEMA, 2012). In order to avoid bias potentially created by scaling ground motions above the level they are recorded, the hazard-consistent incremental dynamic analysis methodology is employed. This methodology adjusts structural response and other parameters to reflect the dominant hazard contributors at a particular location.

Results show that at shaking levels experienced in recent earthquakes in the Oklahoma and Kansas, minor damage consisting of cracking of interior finishes and wallboards, and nonstructural

damage to plumbing and HVAC systems is expected, which is consistent with observed damage in these recent earthquakes. These losses correspond to approximately 6% of the replacement value of the structure (considering $Sa(T_1=0.3) = 0.3g$).

When considering multiple earthquakes in a seismic sequence, damage and vulnerability did not seem to be accumulating. In other words, damage was typically light enough that it did not alter the fragility of the building in the next event in the sequence. In addition, a second event did not change the estimated repair costs or seismic losses because the losses are driven solely by the maximum response in a sequence. This does not mean, though, that cracks are not growing or widening in a second event. We used the Park & van de Lindt (2009) damage index to show that hysteretic energy absorption and damage are accumulating; these changes are not significant enough to change peak responses and losses. In addition, the study shows that if repairs were implemented after each earthquake in the sequences, total seismic losses increase greatly, increasing the overall economic impact of these events. This choice of repair strategy is important for homeowners, who may not be able to or wish to consider future earthquake events in decision making to repair current damages to their homes.

In this case, the use of the hazard-consistent IDA methodology did not significantly alter the results. Although the motions used in the assessment are highly peaked (high *SaRatio*), the expected hazard in Edmond, Oklahoma is even more peaked. The hazard characteristics stem from the fact that we expect moderate magnitude close-in events to dominate the hazard.

CHAPTER 4

4 HAZARD-CONSISTENT SEISMIC LOSSES AND COLLAPSE CAPACITIES FOR LIGHT-FRAME WOOD BUILDINGS IN CALIFORNIA AND CASCADIA

4.1 INTRODUCTION

Even among the high seismic regions of the United States, there is significant variation in tectonic environment that influence seismic hazard, ground motion characteristics and seismic risk. For example, the Pacific Northwest or Cascadia region of the United States is impacted by both crustal and subduction earthquakes. The Cascadia subduction zone, which includes both interface and inslab events, contributes significantly to the seismic hazard for cities like Eugene, Portland, Seattle, and Anchorage. This subduction zone is capable of producing large ($M_W > 9$) earthquakes, with longer durations of shaking and enhanced frequency content at moderate to long periods compared to crustal earthquakes (USGS, 2018). Recently, the 2011 M_W 9.0 Tohoku, Japan earthquake, an interface event, produced ground motions with significant shaking lasting longer than one minute (Furumura, et al., 2011). Even at sites with contributions primarily from crustal earthquakes, there can be unique source or hazard characteristics that amplify frequency content or duration and alter our interpretation of seismic risks. For example, both Los Angeles and San Francisco's seismic hazards are similar and are comprised of only crustal earthquakes. However, expected durations and frequency content vary significantly between the two cities due to higher expected magnitudes at closer rupture distances in San Francisco (Petersen, et al., 2014). Current building standards and codes (International Code Council, 2018; ASCE, 2016) do not explicitly consider ground motion duration or spectral shape (i.e. frequency content at periods other than the first-mode period) in the typical design of new buildings. Thus, although ASCE 7 now explicitly targets specific risk goals, i.e. 1% probability of collapse in 50 years for ordinary, Risk Category

II structures, e.g. (ASCE, 2016; FEMA, 2009), these goals may not be uniformly achieved because of differences in seismic hazard and the resulting ground motions.

Recent studies, e.g. (Raghunandan & Liel, 2013; Chandramohan, et al., 2016), have shown that longer duration shaking increases collapse risk in reinforced concrete (RC) frame and steel frame structures. Spectral shape has also been well documented as a key ground-motion characteristic governing structural response. Baker & Cornell (2006) and Baker (2011) have shown that the selection of ground motions that reflect the expected frequency content at the site is critical for attaining reasonable predictions of nonlinear structural response in dynamic analysis. Recently, Chandramohan et al. (2018) proposed a methodology to account for ground motion duration and spectral shape to modify the design base shear in modern seismic provisions. This methodology involves estimating target durations and spectral shapes based upon the seismic hazard at sites of interest and developing modifications based on these factors to ensure more uniform risk across sites with different characteristics. Chandramohan (2016) has quantified these modification factors for RC and steel structures for select sites in Eugene, Seattle and California, but has yet to investigate light-frame wood buildings. In addition, research has shown that spectral shape and duration have a large impact on a structure's collapse risk and response, but the impacts from these ground motion characteristics on expected seismic loss have been less investigated.

Light-frame wood construction comprises the majority of the building stock in the United States and represents a significant portion of the potential seismic loss in a large earthquake. Indeed, the 1994 Northridge Earthquake caused an estimated property loss of $20 billion to light-frame wood construction (in 1994 dollars) (Kircher, et al., 1997). One recent study, Pan et al. (2018), found that longer shaking durations like those expected in the Pacific Northwest did

increase collapse risk in light-frame wood buildings, but did not consider changes in collapse risk from duration and spectral shape due to subduction earthquakes on these structures.

This study aims to quantify expected seismic risks, including losses and collapse, in light-frame wood buildings, considering region specific seismic hazard characteristics that can greatly influence duration and frequency content of shaking. Specifically, the study assesses one-, two-, and four-story multifamily residential and commercial light-frame wood buildings through dynamic simulations at locations in California, Oregon, Washington and Alaska to estimate seismic loss and collapse risk and show the influence of seismic environment. Results of these analyses are used to quantify seismic losses consistent with the expected hazard and to propose design base shear modification factors that promote uniform risk at each site location. This paper begins by describing the sites, buildings, and modeling techniques. Next, the hazard-consistent incremental dynamic analysis methodology, developed by Chandramohan (2016), is described, with details (selection of intensity measures, ground motion prediction equations, seismic hazard deaggregation, and recommended ground motions for use in dynamic analysis) provided about its adaptation here. First, results are presented describing the hazard-consistent collapse capacity of each building and the implications of these collapse capacities for design values and proposed modification factors. Finally, hazard-consistent seismic losses are quantified using FEMA P-58 (2012) methodology.

4.2 LITERATURE REVIEW

4.2.1 Influence of Duration and Spectral Shape on Structural Response

A region's seismic environment is intimately tied to ground motion characteristics, such as ground motion duration and spectral shape, that can greatly influence a building's structural

response and potential seismic loss. In particular, there have been a number of studies examining the effect of shaking duration and spectral shape on seismic response and risk. Previous research has shown that the duration of shaking has a significant impact on structure's seismic collapse fragility (Raghunandan, et al., 2015; Chandramohan, et al., 2016; Hancock & Bommer, 2007; Iervolino, et al., 2006; Marafi, et al., 2016). In particular, researchers have shown that duration has a significant influence on accumulating damage parameters (Raghunandan & Liel, 2013; Chandramohan, et al., 2016). However, there is some debate in the literature about duration's impact on peak damage parameters, such as story drifts (SDR). Hancock & Bommer (2007) and Iervolino et al. (2006) found that peak drifts did not increase with an increased ground motion duration, while Raghunandan & Liel (2013) and Chandramohan et al. (2016) showed that peak drifts did increase when a building was pushed deep into nonlinear response. Mohammed et al. (2015) experimentally tested RC bridge columns under short and long duration ground motions, finding that long duration motions were more damaging for the same intensity motion. However, peak displacements were not increased for the long duration motion. The literature on duration emphasizes the need to carefully model in-cycle and cyclic deterioration and P-Δ effects to accurately capture these effects (Chandramohan, et al., 2016; Raghunandan, et al., 2015). In terms of spectral shape, Baker & Cornell (2006) and Baker (2011), for example, have shown the necessity of selecting ground motions that reflect the expected spectral shape at the site under investigation. As a structure experiences nonlinear response and period elongation, spectral energies at periods other than the fundamental period of the building become more influential. Eads et al. (2016) showed that for ground motions with the same spectral acceleration at the fundamental period of a structure, the spectra with higher energy at periods around the fundamental period are more damaging than motions with low spectral energy at the same surrounding periods.

These trends can have significant effects on collapse risk that are tied to regional tectonic environment. For example, Raghunandan et al. (2015) found that the median collapse capacity of ductile (post-1970) and non-ductile buildings decreased by 36% and 12% respectively, when subjected to subduction versus crustal ground motions. This increased risk in collapse was attributed to increased durations and increased spectral energies at longer periods observed in ground motions from subduction earthquakes compared to crustal earthquakes. Chandramohan et al. (2016) concluded that the mean annual frequency of collapse values implied by modern seismic provisions are underestimated in Seattle, WA and Eugene, OR by 29% and 59%, respectively, due to the unique the effects of expected ground motion durations and spectral shapes at those sites. Likewise, Marafi et al. (2017) examined the collapse risk of structures in Seattle, considering the effects of subduction earthquakes and the Seattle basin. That study found that collapse capacities for RC buildings decreased when subjected to ground motions with higher spectral energy at long periods due to basin amplifications compared to motions outside of the basin. This underestimation of collapse risk is critical to understand from a building code perspective, in order to develop design rules that meet target uniform risk levels.

Seismic design codes are currently based on design spectral values (i.e. risk-targeted Maximum Considered Earthquake, MCE_R) that are calibrated to achieve an equivalent risk for collapse at different sites (Luco, et al., 2007). To preliminarily consider duration impacts in seismic design codes, Liel et al. (2015) deaggregated the seismic hazard and computed new MCE_R design values using subduction fragility curves that account for the duration and spectral shape of subduction events. This analysis suggested that increases of MCE_R Sa values on the order of 35% may be needed to account for duration and frequency content effects in Portland and Seattle. Structure-specific modification factors have also been developed to account for durations and

spectral shape. Chandramohan (2016) proposed modification factors that increased the design base shear of the structures in an effort to meet the target performance criteria as prescribed by the code. For a structure located in Seattle with a fundamental period of one second, Chandramohan (2016) suggested a duration modification factor which increased the design base shear by 18%, and a spectral shape factor which increased the design base shear by 9%. Combining the two factors totaled a 29% increase in design base shear. These estimates were conducted for RC and steel structures. Potential impacts on light-frame wood construction collapse capacities and seismic losses have yet to be investigated. Both Chandramohan (2016) and Raghunandan & Liel (2013) found that duration effects increased as building period decreased, suggesting that short period buildings, such as light-frame wood construction, may be more heavily impacted by long duration shaking.

4.2.2 Light-Frame Wood Structures

There have been multiple large efforts, including the CUREE Caltech Woodframe Project (Folz & Filiatrault, 2004) and the NEESWood Capstone Test (Pei, et al., 2010), conducted to improve understanding of seismic response of light-frame wood structures and to develop tools to aid in the quantification of their seismic response. For example, in NEESWood, Van de Lindt et al. (2010) tested a full-scale six-story light-frame wood residential building on a shake table. More recently, projects such as the Applied Technology Council (ATC) 116 (2018), have investigated the performance of many short period structures, including light-frame wood construction, in areas of high seismic hazard. That study shows that these buildings have good collapse resistance. Available software tools include the Cyclic Analysis of Shear walls (CASHEW) (Folz & Filiatrault, 2001) and the Seismic Analysis of Woodframe Structures (SAWS) (Folz & Filiatrault,

2004). More recently, SAPWood (van de Lindt, et al., 2009) and Timber3D (Pang, et al., 2012) has improved upon these earlier tools. Christovasilis (2010) also developed advanced models for two-dimensional shear walls during the NEESWood Capstone Project. Filiatrault et al. (2002) showed that it is critical to incorporate the effects of nonstructural components in seismic performance assessments of these buildings, as they can significantly change the expected stiffness, strength, and fundamental period of the building. These software tools have been shown to reasonably capture the response of light-frame wood buildings in full-scale shake table tests (van de Lindt, et al., 2009).

To consider the effects of multiple loading sequences on light-frame wood buildings, Nazari et al. (2013) simulated response of a two-story residential frame structure subjected to artificial mainshock-aftershock sequences. They showed that the structure's fragility increased when subjected to multiple seismic loadings, but not to the extent that has been observed with other studies focusing on other structure types (i.e. steel or reinforced concrete). Goda and Salami (2014) also investigated mainshock-aftershock sequences on light-frame wood construction, showing that aftershocks led to 5–20 % increase of the median inelastic seismic demand curves when the structure was initially shaken to a moderate damage state. These mainshock-aftershock studies suggest that light-frame wood construction is susceptible to strength and stiffness deterioration under prolonged seismic loading. Pan et al. (2018) found that longer shaking durations did decrease the median collapse fragility in light-frame wood buildings on the order of 26-61%, looking at two-story single-family dwellings with varying shear wall configurations. However, that study did not combine these fragilities with seismic hazard considerations to examine the overall impact on risk.

4.3 SITE LOCATIONS

This study examines seismic risk at six sites located in the western U.S.: Los Angeles, CA, San Francisco, CA, Eugene, OR, Portland, OR, Seattle, WA, and Anchorage, AK. These sites are selected to capture a broad range of subduction (interface and inslab) and crustal hazards. Figure 4.1 documents the percent contribution of crustal and subduction hazards for each site at the 2475-year hazard level for Sa(T=0.3s) (Petersen, et al., 2014), ranging from 100% crustal in Los Angeles to 98% contribution from subduction sources in Eugene. All sites fall in seismic design category (SDC) D as determined by ASCE 7-16 (2016). Table 4.1 shows each site's short period response acceleration parameter (S_{DS}), as determined by the 2015 NEHRP Provisions and adopted by ASCE 7-16 (2016) considering site class D soil conditions, as well as longitude and latitude coordinates used within each city.

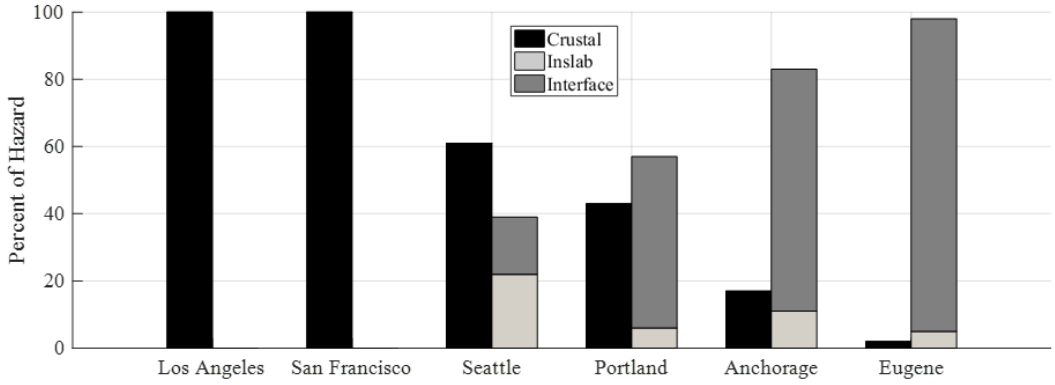

Figure 4.1. Contribution of crustal and subduction source types (inslab and interface) to seismic hazard for sites in Los Angeles, San Francisco, Seattle, Portland, Anchorage, and Eugene at the 2475-year hazard level for Sa(T=0.3s).

Table 4.1. Site locations and design values.

Site	Latitude [degrees]	Longitude [degrees]	SDC	S_{DS} [g]
Los Angeles	33.996	-118.162	D	1.47
San Francisco	37.78	-122.403	D	1.20
Seattle	47.6071	-122.3358	D	1.12
Portland	45.5207	-122.6789	D	0.71
Anchorage	61.2156	-149.8956	D	1.20
Eugene	44.05	-123.09	D	0.58

4.4 BUILDING ARCHETPYES AND DESIGN

This study investigates the seismic risk of one-, two-, and four-story multifamily residential and commercial light-frame wood buildings, considering a total of six different archetypes. The building archetypes are chosen to be representative of the typical building stock in the western United States. The building examined in this study were designed for "high seismicity areas", as described by the ATC 116 project (ATC, 2018). These buildings were designed according to ASCE 7-10 (ASCE, 2010). All building designs are intended for locations at the upper end of SDC D, referred to as D_{max}, and corresponding to a seismic response coefficient (C_s) of 0.154 and S_{DS} of 1.0g. (ASCE, 2010; FEMA, 2009). As all buildings are designed to the same S_{DS}, the buildings are over designed for Eugene and Portland, and are under-designed for Los Angeles, San Francisco, Seattle, and Anchorage.

4.4.1 Multifamily Residential Buildings

The design of each multifamily building lies on a 14.6 m by 29.3 m (48 ft by 96 ft) footprint. This design accommodates six 7.3 by 9.8 meter (24 by 32 foot) adjacent units per floor in the one- and four-story multifamily buildings. The unit and shear wall layouts for the one-story archetype are shown Figure 3.2 and Figure 3.3, respectively. The two-story archetype is different in its layout,

featuring four two-story townhouses attached to each other. Each townhouse units sits on a 7.3 m by 14.6 m (24 ft by 48 ft) footprint. The foundation for all multifamily archetypes is a 5 cm (4 in) concrete slab on grade, with spread footings at the interior posts and thickened, reinforced beams integral with the slab at the perimeter and at all interior load bearing walls. For the multistory archetypes, the floor systems are framed with 5x10 cm (2x4 in) parallel chord trusses, spaced at 61 cm (24 in) on center. The exterior walls, shown in Figure 4.3, are framed with 5x15 cm (2x6 in) lumber, with exterior faces are clad in stucco over 1.1 cm (7/16 in) thick oriented strand board (OSB). The interior face of the exterior walls is clad with 1.3 cm (1/2 in) gypsum wall board. The interior shear walls (party walls) are actually two lines of 5x10 cm (2x4 in) framing separated by a 2.5 cm (1 in) gap, which would in reality be a larger corridor, finished with gypsum wallboard on the face of the wall toward the interior of the unit, but with no sheathing applied to the corridor face, to resemble typical construction practices. For more detailed descriptions of the building designs, see the ATC 116 report (ATC, 2018).

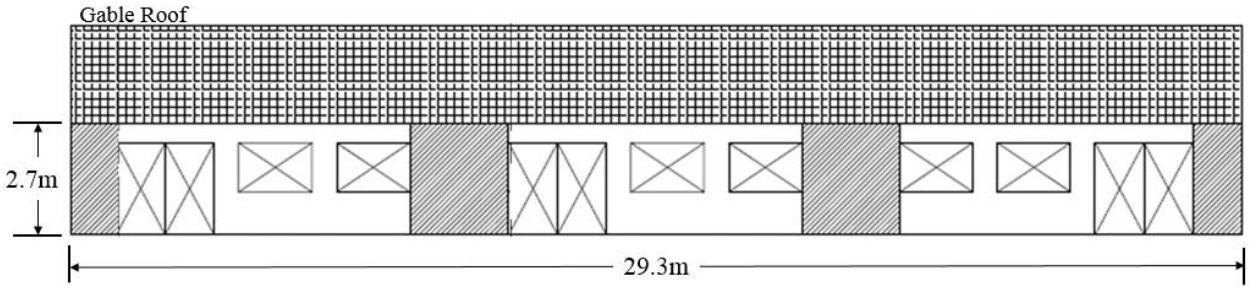

Figure 4.2. Elevation view of the one-story multifamily building used in this study, and designed for the purposes of ATC 116 (Image provided by D. Jared DeBock and modified here).

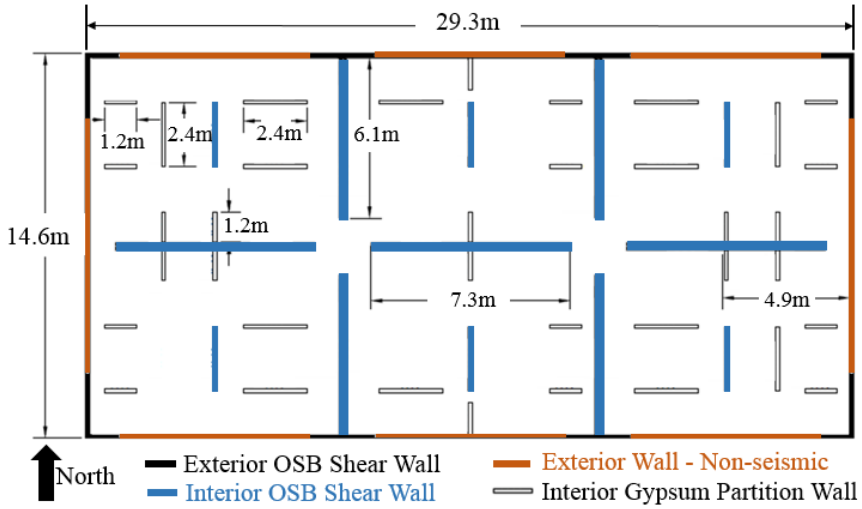

Figure 4.3. Plan view of the shear and bearing wall layout for the one-story multifamily building. (Original image provided by D. Jared DeBock and modified here).

4.4.2 Commercial Buildings

The commercial buildings also rest on a 14.6 m by 29.3 m (48 ft by 96 ft) footprint. The one-story design does not include any interior nonstructural partition walls to represent occupancies such as a repair shop or store. The two and four-story designs incorporate some nonstructural partition walls to represent occupancies such as office space. Shear walls are located around the perimeter of the building for all three archetypes. Like the multifamily designs, the exterior shear walls are framed with 5x15 cm (2x6 in) lumber. The exterior faces of the exterior shear walls are clad with stucco over 1.1 cm (7/16 in) thick OSB and the interior faces are clad with one-half inch gypsum wallboard. The floor and roof trusses are supported by wood bearing walls and by interior steel girders at 7.3 m (24 ft) on center, which span to steel posts. There are three interior steel posts and three steel posts along each long exterior wall (Figure 4.4). These steel elements do not contribute to the lateral force resisting system in the buildings. The foundation system is the same as for the residential archetypes.

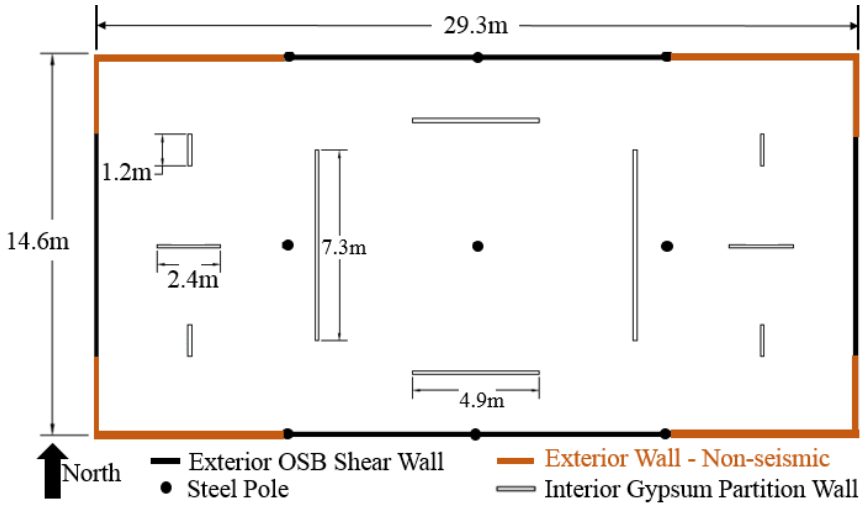

Figure 4.4. Plan view of the shear and bearing wall layout for the two and four-story commercial buildings. The one-story commercial archetype is the same, but without the interior gypsum partition walls (Original image provided by D. Jared DeBock and modified here).

4.5 BUILDING MODELING

The buildings are modeled using Timber3D, a nonlinear structural analysis software for wood frame construction based in MATLAB that was developed by Pang et al. (2012; 2013). The software is intended for simulating seismic response of 3D light-frame wood construction system to capture individual wood frame elements and the interaction of their responses, up to large horizontal and vertical displacements. Timber3D improves upon the so-called lumped parameter approach of *SAWS* (Folz & Filiatrault, 2004) and *SAPWood* (Pei & van de Lindt, 2011), by employing a finite element methodology with nodal condensation and shape functions to decrease the required computational expense. In addition, Timber3D is formulated to capture vertical uplift forces present in light-frame wood shear walls, as well as large displacements in flexible diaphragms. The goal of this study is to simulate seismic response of light-frame wood construction and examine the sensitivity of response to the duration and unique frequency content of different west coast sites. Thus, it is particularly important to capture cyclic and in-cycle

degradation to quantify loading cycle effects (Chandramohan, et al., 2016; Raghunandan & Liel, 2013; Raghunandan, et al., 2015; Amadio, et al., 2003), and large deformations and geometric (P-delta) effects (Mahin, 1980) to simulate side-sway collapse in the first story, the predominant failure mechanism in light-frame wood structures (Pang, et al., 2012; Ghehnavieh, 2017). These models from ATC 116, provided by Ghehnavieh (2017).

In these models, nonlinear behavior is modeled only in the wall elements. Wall elements include both the shear walls, which in the design are taken to be the sole lateral force resisting system in the structure, and the interior partition walls. Figure 4.5(a) and (b) show the hysteretic characteristics for 1.2 m by 3 m (4 ft by 10 ft) sections of an exterior shear wall and interior partition wall, respectively, illustrating the model's treatment of strength and stiffness deterioration, in-cycle and cyclic deterioration and pinching effects. These hysteretic plots show the nonlinear response for the wall without any nonstructural finishes, the effect of which are shown in Figure 4.5(c) for the nonstructural exterior stucco finish. In Timber3D, these elements are assigned at the same location such that the composite wall response accounts for structural and nonstructural contributions. The hysteretic model that defines the response of the nonlinear wall elements and finishes is a modification to the Modified Stewart Hysteretic Model developed by Ghehnavieh (2017). The model parameters for each individual wall element represents cyclic wall behavior as a function of wall length, nail spacing, and stud spacing, and are based on parameters calibrated to experimental results. The Modified Stewart Hysteretic Model was developed during the CUREE tests (Folz & Filiatrault, 2001) based on experimental testing of wood shear walls under quasi-static loading. The further modified model (Ghehnavieh, 2017) employed here follows the same hysteretic behavior, but fits an "S" curve to the post peak response, instead of a linear

degradation, to capture a nonlinear strength decay to better represent residual strength observed at large displacements in light-frame wood shear walls.

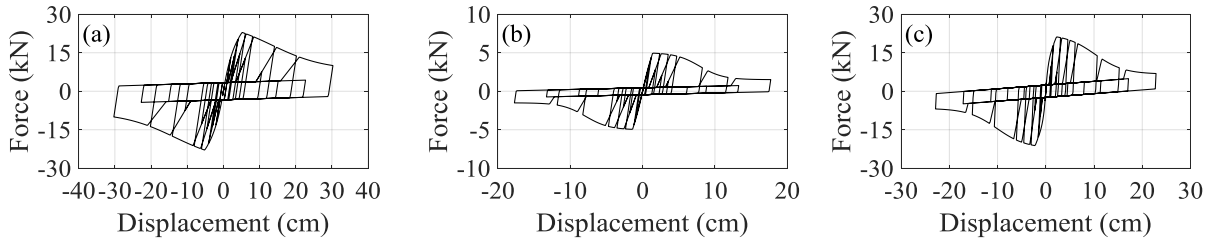

Figure 4.5. Force vs. displacement hysteresis of 1.2 m wide by 3 m tall (4 ft by 10 ft) sections of (a) an OSB shear wall, (b) an interior gypsum partition wall, and (c) exterior stucco siding found in all archetypes.

The concrete foundation, sill plates, stud elements, and floor diaphragms are modeled as elastic elements, while the hold downs, anchor bolts, and soil elements are modeled rigidly. In this study, the diaphragms are modeled to be elastic, but very stiff. The base of the structure is modeled with multiple elements to simulate the effects of hold downs, anchor bolts, sill plates, the concrete foundation, and even the surrounding soil, as shown in Figure 4.6. The result is an effectively fixed base.

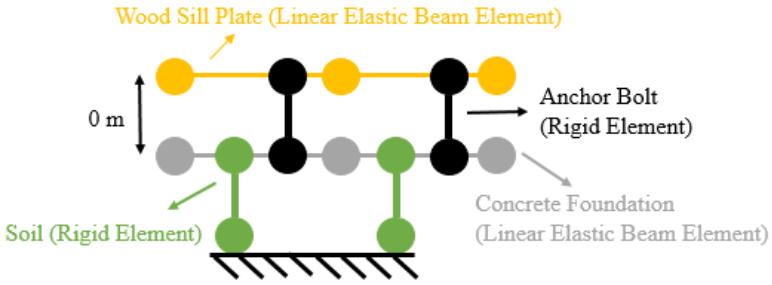

Figure 4.6. Base elements for Timber3D building simulation models, showing the wood sill plate, hold downs, anchor bolts, concrete foundation, and soil elements.

Timber3D's formulation also captures large geometric deformations and corotational effects, which together with modeling of hold down and contact forces between the framing

members, enables simulation of large vertical displacements as side-sway collapse occurs (Pang & Shirazi, 2013). Unlike ATC 116, we define collapse by the downward (vertical) displacement of the second floor exceeding 25 cm (10 in). Collapse capacities are not very sensitive to the exact definition of vertical displacement corresponding to collapse as, at this point, lateral and vertical displacements are increasing without bound.

In accordance with other previous studies (Pang & Shirazi, 2013; van de Lindt, et al., 2009), we applied 1% Rayleigh damping to the first and second modes (E-W and N-S lateral directions) of the buildings. Damping in light-frame wood buildings is largely controlled by the nonlinear response of the hysteretic components such as the shear walls (Filiatrault, et al., 2003). In Timber3D, this damping is already accounted for in the hysteretic calibration of the wall elements. However, because in Timber3D damping can only be applied to all or none of the elements, a low damping value is selected to avoid over damping in the nonlinear range. Although ATC 116 applied no elastic damping, the damping employed in this dissertation is intended to provide more reasonable predictions at lower shaking levels for seismic loss estimates; conversely, ATC 116 was only investigating collapse level shaking. Damping is Timber3D is applied as Rayleigh damping, based on the mass and initial stiffness. A brief investigation found that the implementation of 0% or 1% Rayleigh damping did not significantly impact the results at collapse levels.

Table 4.2. Archetype building characteristics.

Model ID	Occupancy	Stories	Fundamental Period, T_1 [s]	Seismic Weight [kN]	Design V/W	Ductility* μ_T	Overstrength* Ω_0
MFD1	Multifamily	1	0.19	630	0.154	4.8	7.9
MFD2	Multifamily	2	0.29	1450	0.154	4.5	4.7
MFD4	Multifamily	4	0.51	3830	0.154	6.1	2.6
COM1	Commercial	1	0.33	800	0.154	4.6	3.2
COM2	Commercial	2	0.39	1970	0.154	4.7	3.1
COM4	Commercial	4	0.62	4310	0.154	2.8	2.2

*Calculated as per FEMA P-695 (2009).

Figure 4.7 compares the monotonic force-displacement curves for all archetypes in both the horizontal directions, with other key details, such as period, design base shear and overstrength (Ω_0) provided in Table 4.2. In all archetypes, the ultimate strength of each building is much higher than the design base shear. This overstrength stems from the inclusion of nonstructural partition walls and nonstructural finishes on all the walls in the models. The design V/W is equal to 0.154 (seismic response coefficient - C_s) for all buildings. In both orthogonal directions, the 1-story multifamily building has the largest overall strength, while the 4-story multifamily building is the most ductile. The residential archetypes have higher overstrengths than the commercial archetypes of the same height, due to the much greater number of internal walls in the residential designs, due to architectural constraints. In particular, the 1 story multifamily building has a much higher overstrength than any other building due to its relatively low seismic weight and large number of internal walls. OSB shear walls comprise the lateral force resisting system for all buildings in both direction. Results also show that, despite modern design and detailing and a design R factor of 6.5, all of the buildings are relatively non-ductile when compared to modern ductile reinforced concrete moment frames ($\mu_T \approx 15$) (Raghunandan & Liel, 2013). FEMA P-695 developed similar light-wood frame archetypes reporting overstrengths between 2.2 and 3.4, and ductilities between 7.7 and 9.8.

The buildings used in this study have higher overstrengths and are less ductile when compared to similar building archetypes examined in FEMA P-695 (FEMA, 2009), likely due to the inclusion of nonstructural finishes such as stucco and gypsum wallboard in the modeling of the buildings in this study. Gypsum and stucco finishes are less ductile than OSB shear walls as shown in Figure 4.5, influencing the shape of the pushover curve (Figure 4.7), and resulting in a lower μ_T.

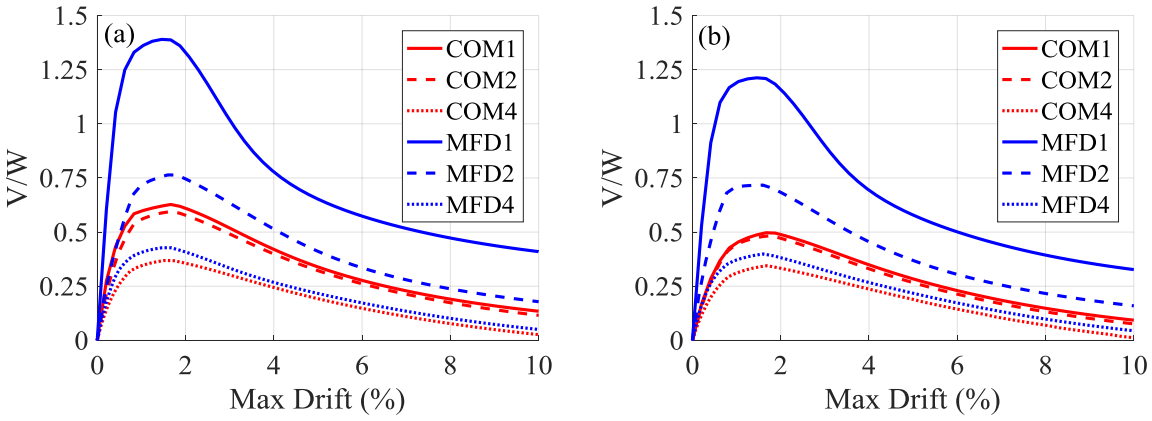

Figure 4.7. Pushover curves for the archetype buildings in the (a) E-W and (b) N-S directions, considering distributed loading according to the first mode shape.

4.6 HAZARD-CONSISTENT IDA METHOD

Incremental dynamic analysis (IDA) is a method developed by Vamvatsikos & Cornell (2002) dynamically simulates a structure under earthquake loading, scaling up a ground motion up incrementally and recording structural response until collapse is reached. IDA enables the use of a single set of earthquake ground motions to provide estimates of structural response at multiple intensity levels, not just the intensity of the recorded earthquake motion. One shortcoming of IDA is the bias in terms of spectral shape that can be produced from scaling ground motions above the level at which they were recorded, producing ground motions that are inconsistent with the hazard and have unrealistic frequency content (Vamvatsikos & Cornell, 2002; Baker & Cornell, 2006). This presents a difficulty here, because of our interest in examining earthquakes and ground

motions beyond the levels that have been experienced. Methods such as multiple stripe analysis (MSA) use different ground motion sets for different intensity levels to account for this inconsistency with respect to seismic hazard (Jalayer, 2003), but this can extend the computational effort. Recently, Chandramohan (2016) developed a structural reliability framework that can produce hazard-consistent results while using a generic set of ground motions in an IDA. In this methodology, spectral shape and ground motion duration are used to adjust the results of a generic IDA to represent realistic ground motion characteristics. This study adapts the framework developed by Chandramohan (2016) to adjust engineering demand parameters or EDPs (namely, story drifts (SDR), floor accelerations, residual drifts, and collapse capacities) obtained from the IDA to account for the expected spectral shape and duration at the site of interest. This framework utilizes the computational advantage of using a single set of records in an IDA, while still producing hazard-consistent results generated using methods such as MSA.

The hazard-consistent IDA methodology provides a procedure whereby generic ground motions can be utilized for all scaling intensities, but the hazard characteristics of a particular site can be considered. Seismic hazard deaggregation is performed at the site of interest to acquire the characteristics (magnitude, rupture distance, epsilon, and source type) that are most probable at the site, for each hazard level. The deaggregation components are then fed into ground motion predication equations (GMPE) to develop expected ground motion intensities, spectral shapes, and durations at the site. These intensity measures are the target values expected to occur at the site. A generic suite of ground motions with a wide range of spectral shapes and durations is used in an IDA on the model. Regressions are then developed to correlate structural response to spectral shape and duration. The target IM are then used to adjust the results of the IDA to be hazard-consistent for the site and shaking level of interest. For a more detailed description of the framework, the

reader is referred to Chapter 5 in Chandramohan (2016). More recently, Zhong & Deierlein (2018) built upon this framework to expand hazard-consistent building responses for a range of intensity levels below collapse.

4.6.1 Metrics for Duration and Spectral Shape

Here, spectral shape is quantified by the dimensionless parameter, *SaRatio* (Eads, et al., 2016), and ground motion is quantified by significant duration or time to accumulate 5-75% of the Arias Intensity ($Ds_{5\text{-}75}$) (Trifunac & Brady, 1975). Chandramohan (2016) evaluated numerous intensity measures for duration and spectral shape to find the best predictors of structural response. In that study, other duration measures (e.g., $Ds_{5\text{-}95}$) and spectral shape measures (e.g. epsilon) were also explored. Ultimately, Chandramohan (2016) suggested that *SaRatio* and $Ds_{5\text{-}75}$ were the best predictors based on comparing their efficiency to other intensity measures as suggested by Luco & Cornell (2007). This study uses slightly modified versions of these intensity measures in the hazard-consistent IDA procedures.

SaRatio is defined as the spectral acceleration at the fundamental period of the building, $Sa(T_1)$, normalized by $Sa_{avg.}$ Sa_{avg} is the average spectral accelerations across a range of periods (Eads, et al., 2015). A higher *SaRatio* indicates a more peaked spectrum near the period of interest. Therefore, a ground motion with a lower *SaRatio* tends to be more damaging to a structure when the structure is pushed into its nonlinear range. For the purpose of calculating *SaRatio,* the period range recommended by Eads et al. (2015) is $0.2T_1$ to $3T_1$; the same range is also employed by Chandramohan (2016). However, for this study, a period range of T_1 to $3T_1$ is adopted. *SaRatio* using this period range (i.e., $SaRatio(T_1,3T_1)$) is found to correlate much better with the structural response of the light-frame wood building models used in this study. Specifically, this *SaRatio*

does not depend on $T < T_1$, which does not significantly influence the response of these short-period structures. *SaRatio* is selected as the parameter to represent spectral shape due to its higher efficiency compared other metrics, such as epsilon, as shown in Chandramohan (2016). Furthermore, hazard information for *SaRatio* is easily attainable from spectral acceleration based ground motion prediction tools and Sa-based hazard tools are easily adaptable for *SaRatio*.

The traditional definition of $Ds_{5\text{-}75}$ is modified slightly based on Walling et al. (2018), and referred to as $Ds_{5\text{-}75,NGA}$. $Ds_{5\text{-}75,NGA}$ quantifies only the most intense time periods of shaking (based on the derivative of the Arias Intensity husid plot). The result is that ground motions that have multiple periods of strong energy have shorter calculated durations due to the low energy section between the strong energy shaking being removed from the duration calculation. This result is negligible for crustal records (often having one period of shaking) but can be significant for subduction motions (like ground motions from the 2011 Tohoku, Japan earthquake).

4.6.2 Seismic Hazard Deaggregation

Seismic hazard deaggregation information is acquired from the United States Geological Survey (USGS) from the 2014 National Hazard Model (Petersen, et al., 2014; USGS, 2018). Deaggregations are conducted at each site for three spectral acceleration levels of Sa(T=0.2s), Sa(T=0.3s), and Sa(T=0.5s) to match the fundamental periods of the six models as closely as possible (see Table 4.2), and for nine different hazard levels ranging from 75 to 10000 year return periods. Site conditions are assumed to be the boundary between site class B and C (Vs30 = 760 m/s) for all sites. In each case, deaggregation information includes moment magnitude (M), rupture distance (R), epsilon (ε), source type (crustal, inslab, or interface), and percent contribution to the total hazard. We use the mean M, R, ε, and percent contribution for a given source type at each

hazard level. Example deaggregation results at a period of 0.3s in Eugene are shown in Table 4.3. Deaggregations at each site at Sa(T=0.3s) can be found in Appendix A.2.

Table 4.3. Seismic hazard deaggregation from the 2014 USGS Hazard Model for T=0.3s in Eugene showing mean M, R, ε, and percent contribution for all source types at all hazard levels.

		Crustal				Inslab				Interface			
Hazard Level	**Sa(T=0.3s) [g]**	**M**	**R [km]**	**ε**	**%**	**M**	**R [km]**	**ε**	**%**	**M**	**R [km]**	**ε**	**%**
75	0.03	6.4	121	0.3	65	6.9	128	-1.2	11	8.7	108	-2.8	24
275	0.13	6.5	63	0.7	17	6.9	92	-0.3	15	8.8	98	-1.1	68
475	0.23	6.5	40	0.8	8	6.9	80	0.2	13	8.8	93	-0.4	80
975	0.40	6.5	25	0.9	4	7.0	71	0.7	10	8.9	85	0.2	86
2475	0.69	6.5	17	1.2	3	7.0	64	1.1	9	8.9	79	0.8	89
4000	0.87	6.5	15	1.3	2	7.0	62	1.3	8	8.9	76	1.0	90
6000	1.03	6.5	13	1.4	2	7.1	61	1.5	7	9.0	75	1.2	91
8000	1.16	6.6	12	1.5	2	7.1	60	1.6	7	9.0	73	1.3	91
10000	1.26	6.6	11	1.5	2	7.1	59	1.7	7	9.0	73	1.4	92

Table 4.3 shows that the total contributions from each source type change as the hazard level increases. In Eugene, most notably, crustal hazards contribute 65% to the total hazard at the 75-year hazard level and then falls to 2% at the 10000-year hazard level. Conversely, interface earthquakes contribute only 24% at the 75-year hazard level and increases to 92% at the 10000-year hazard level. In all cases, ε increases as the return period increases, indicating a more peaked spectra with more rare events. M increases and R decreases for each source type with increasing hazard level. Both Los Angeles and San Francisco's seismic hazards are comprised of 100% crustal source types which follow the M, R, and ε trends seen in Eugene. Portland and Anchorage both follow the same trends described above with an increasing subduction hazard and decreasing crustal hazard. Seattle actually sees an increase in crustal hazard and decrease in subduction hazard as hazard levels increase. M, R and ε values tend to stay constant when looking at the different spectral periods. Although several relatively short periods of interest are considered, the same seismic scenarios dominate the hazard regardless of these periods.

4.6.3 Ground Motion Prediction Equations and Correlations

The GMPEs used for spectral acceleration and duration for different source types are reported in Table 4.4. These GMPEs are used to determine expected spectral acceleration and ground motion duration from the M, R, and ε values gathered from the deaggregation for each source type. GMPEs used for duration and spectral acceleration for subduction earthquakes are based on work from NGA-Sub (PEER, 2018), and represent the most recent GMPEs developed for this purpose.

Table 4.4. Spectral acceleration and significant duration GMPEs used in the hazard-consistent methodology.

	Crustal GMPE	**Inslab GMPE**	**Interface GMPE**
Spectral Acceleration	Campbell & Bozorgnia (2014)	BC Hydro 2018 Update (Abrahamson et al., 2018)	BC Hydro 2018 Update (Abrahamson et al., 2018)
Significant Duration	Afshari & Stewart (2016)	NGA-Sub (Walling et al., 2018)	NGA-Sub (Walling et al., 2018)

The M and R inputs to the GMPES are from the deaggregation; other inputs are based on assumptions described here. $V_{S,30}$ is assumed to be 760 m/s for all of the GMPEs. For BC Hydro 2018 for subduction earthquakes, Z_{tor} (depth to the top of fault) values are necessary. We assume Z_{tor} for interface earthquakes to be 25 km for Eugene, Portland, Seattle, and Anchorage. Z_{tor} for inslab earthquakes is taken to be 45 km for Eugene, 50 km for Seattle and Portland, and 40 km for Anchorage (Frankel, 2018). For the Campbell & Bozorgnia (2014) GMPE, fault width (W) is estimated using the recommendations of Kaklamanos et al. (2011). The fault was assumed to be vertically oriented (i.e. normal to the ground surface), having a rake angle of zero degrees, without a hanging wall. Based on these parameters, we followed the recommendations of Campbell & Bozorgnia (2014) to estimate $Z_{tor,}$ Z_{bot} (depth to the bottom of fault), Z_{hyp} (depth to the hypocenter), and $Z_{2.5}$ (depth to the 2.5 km/s shear-wave velocity horizon).

The current version of Walling et al. (2018) is preliminary and does not include a site term and, unsurprisingly, our analysis showed a bias with V_{s30}. Previous authors have shown that a site term is needed for duration GMPEs (Kempton & Stewart, 2006; Bommer, et al., 2009; Afshari & Stewart, 2016). Accordingly, we apply nonlinear regression based on data from Van Houtte et al. (2017) to formulate a site term for use with the Walling et al. (2018) GMPE, according to Equation 4.1:

$$\ln\left(\widehat{Ds_{5-57,NGA}}\right)_{es} = \ln\left(\mu_{source} + \mu_{path}\right)_{es} + \left(c_0 + c_1 \ln\left(\frac{V_{S,30}}{760}\right)\right)_s \quad (4.1)$$

where $\widehat{Ds_{5-57,NGA}}$ is the median estimated significant duration, μ_{source} is the source duration as calculated using the median coefficients in Walling et al. (2018), μ_{path} is the path duration as calculated using the median coefficients in Walling et al. (2018), and c_0 and c_1 are regression coefficients equal to -0.2469 and -0.1466, respectively. The subscripts e and s refer to the predictions for the s-th site in the e-th earthquake. The logarithmic errors of the adjusted model, calculated as $\varepsilon r = \ln\left(Ds_{5-75,NGA}\right) - \ln\left(\widehat{Ds_{5-75,NGA}}\right)$, pass a Lilliefors (1967) test for normality and have zero mean.

Trends of the duration GMPEs are illustrated in Figure 4.8. In order to compare durations from the crustal duration GMPE, Afshari & Stewart (2016), with Walling et al. (2018) for subduction events, it is necessary to convert $Ds_{5\text{-}75}$ to $Ds_{5\text{-}75,NGA}$. For this purpose, $Ds_{5\text{-}75}$ and $Ds_{5\text{-}75,NGA}$ are calculated for the FEMA P-695 (2009) Far Field ground motions (all crustal). A linear regression was performed between $Ds_{5\text{-}75}$ and $Ds_{5\text{-}75,NGA}$, showing that $Ds_{5\text{-}75,NGA} = 0.896\ Ds_{5\text{-}75}$ with an $R^2 = 0.93$. This relationship is used to deterministically convert crustal $Ds_{5\text{-}75}$ to $Ds_{5\text{-}75,NGA}$ for comparison. This figure shows that, for higher magnitude earthquakes, Afshari & Stewart (2016)

predicts much higher durations for crustal earthquakes than for subduction earthquakes with the same magnitude and site-to-source distance. The longer durations at high magnitudes results from the long durations ground motions from the Wenchuan and Denali earthquakes that influenced the Afshari & Stewart (2016) trends at large magnitudes. Subduction earthquakes are known to produce long duration shaking. However, the results of Figure 4.8 tend to suggest that these long durations are more a function of the large R and M usually associated with these earthquakes. Walling et al. (2018) predicts a longer duration for interface earthquakes compared to inslab earthquakes for large distances, considering the same magnitude, because of the multiple slips experienced in large interface earthquakes, spreading out the seismic waves and increasing the duration at the site.

The correlation coefficients needed are between the residuals of spectral accelerations at different periods and between spectral acceleration and ground motion duration. Table 4.5 lists the correlation coefficient models used in this study. Baker & Jayaram (2008) was selected for period by period spectral acceleration correlations for all source types because these correlations have been shown to be relatively insensitive to the tectonic environment. Bradley (2011) is selected for crustal spectral accelerations and significant durations, consistent with Chandramohan (2016). For correlations between spectral acceleration and duration for subduction environments, correlation coefficients are computed between Walling et al. (2018) and Abrahamson et al. (2018) for implementation into the hazard-consistent IDA framework. The new correlation coefficients and their comparison with Bradley (2011) are described in Appendix A.4.

Table 4.5. Correlation coefficient models between spectral acceleration at different periods and between spectral acceleration and significant duration.

	For: Crustal Sources	**Inslab Sources**	**Interface Sources**
$Sa(\tau_i)$ vs $Sa(\tau_j)$	Baker & Jayaram (2008)	Baker & Jayaram (2008)	Baker & Jayaram (2008)
Ds vs $Sa(\tau_i)$	Bradley (2011)	NGA-Sub vs BC Hydro (computed in this study)	NGA-Sub vs BC Hydro (computed in this study)

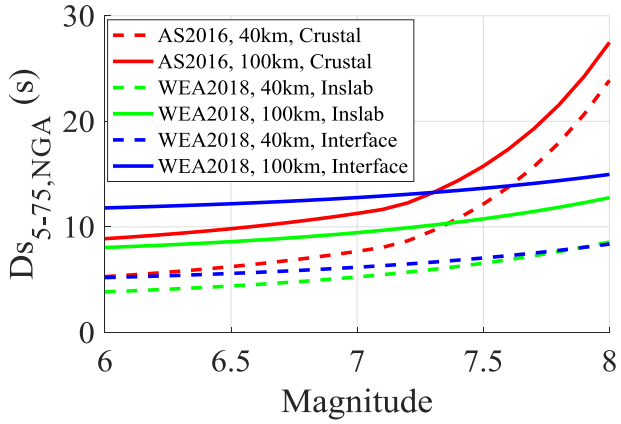

Figure 4.8. $Ds_{5\text{-}75,NGA}$ plotted for a range of magnitudes for the selected duration GMPEs. AS2016 corresponds to Afshari and Stewart (2016) and WEA2018 corresponds to Walling et al. (2018).

4.6.4 Target *SaRatio* and Significant Duration

Following the framework outlined in Chandramohan (2016) Chapter 5, and using the modifications outlined in the previous sections, target *SaRatio* and $Ds_{5\text{-}75,NGA}$ are calculated for each building model, at each site, for the nine previously defined hazard levels. Table 4.6 shows the target *SaRatio* and $Ds_{5\text{-}75,NGA}$ for the hazard at 0.3s, corresponding to the two-story multifamily building, in Los Angeles and Eugene. Table 4.7 shows the target *SaRatio* and $Ds_{5\text{-}75,NGA}$ for the four-story multifamily at the same sites. Target *SaRatio* and $Ds_{5\text{-}75,NGA}$ for each multifamily building at each site can be found in Appendix A.3.

Table 4.6. Hazard and target spectral shapes and duration at 0.3 s period for the two-story multifamily building (MFD2).

	Los Angeles			Eugene		
Hazard Level	**Sa(T=0.3s) [g]**	***SaRatio (0.29,087)***	***$Ds_{5\text{-}75,NGA}$* [s]**	**Sa(T=0.3s) [g]**	***SaRatio (0.29,087)***	***$Ds_{5\text{-}75,NGA}$* [s]**
75	0.26	2.1	4.8	0.03	1.4	12.2
275	0.57	2.3	4.3	0.13	1.3	13.4
475	0.76	2.4	4.2	0.23	1.3	12.5
975	1.08	2.5	4.2	0.40	1.4	11.1
2475	1.59	2.7	4.1	0.69	1.5	9.8
4000	1.90	2.8	4.1	0.87	1.5	9.3
6000	2.20	2.9	4.0	1.04	1.7	8.9
8000	2.40	3.0	4.1	1.16	1.6	8.8
10000	2.57	3.0	4.0	1.26	1.6	8.5

Table 4.7. Hazard and target spectral shapes and duration at 0.5 s period for the four-story multifamily building (MFD4).

	Los Angeles			Eugene		
Hazard Level	**Sa(T=0.5s) [g]**	***SaRatio (0.51,1.53)***	***$Ds_{5\text{-}75,NGA}$* [s]**	**Sa(T=0.5s) [g]**	***SaRatio (0.51,1.53)***	***$Ds_{5\text{-}75,NGA}$* [s]**
75	0.18	2.6	5.4	0.03	1.8	12.2
275	0.39	2.9	5.0	0.10	1.8	13.4
475	0.53	2.9	4.9	0.18	1.8	13.0
975	0.75	3.0	4.8	0.31	1.9	11.9
2475	1.12	3.2	4.7	0.53	2.0	10.9
4000	1.35	3.3	4.7	0.67	2.1	10.5
6000	1.56	3.4	4.7	0.79	2.2	10.1
8000	1.71	3.4	4.7	0.88	2.2	9.9
10000	1.84	3.5	4.7	0.96	2.2	9.8

Overall trends when comparing the target IM between Los Angeles and Eugene are consistent at 0.3 and 0.5s periods (Table 4.6 and Table 4.7). Target *SaRatios* are higher in Los Angeles than in Eugene, indicating a more peaked spectra in Los Angeles. Eugene also has a longer target $Ds_{5\text{-}75,NGA}$. These *SaRatios* and durations are consistent with what would be expected by the seismic hazard differences; Eugene is dominated by subduction hazards (Table 4.3) with magnitudes and distances that produce higher long period energy and longer duration shaking than the crustal earthquake scenarios that control the seismic hazard in Los Angeles. In Eugene, the

expected duration generally decreases as the hazard level increases. The decrease in duration is due to two competing factors. As shown in Table 4.3, as hazard level increases (i.e., for the rarer events), M increases and R decreases. These trends have opposite effects on duration of shaking, but the decreasing R plays a more significant role in the expected duration, relative to M. Therefore, the expected duration decreases. This trend is much more prominent in Eugene relative to LA because of the larger R associated with subduction earthquakes, relative to crustal earthquakes.

Comparing the deaggregation and target IMs in Eugene between 0.3s and 0.5 s periods (Table 4.6 and Table 4.7), the sensitivity of duration to hazard level is less significant at longer periods and the durations are slightly longer for the longer period structure. Target *SaRatios* and $Ds_{5\text{-}75,NGA}$ are both higher for a conditioning period of T=0.5s when compared to T=0.3s at both sites, indicating a more peaked spectra and longer durations are expected for structure with a longer fundamental period. When comparing corresponding deaggregations, the T=0.5s deaggregations have higher M and R for the same hazard level, resulting in longer expected durations. This trend is also consistent with Chandramohan (2016), who showed that at shorter condition periods (T<1s) target durations decreased with an increasing hazard level for interface earthquakes in Seattle, but at longer periods (T≈4s) target durations increased. In the same deaggregation comparison, epsilons for T=0.3s and T=0.5s were very similar. The more peaked spectrum at T = 0.5s is believed to be due to the governing overall shape of typical response spectra. A spectrum with the same epsilon at a longer period will have a higher *SaRatio* when compared to a spectrum with the same epsilon at a shorter period. This trend is because the longer period is farther away from the peak of energy found in the general response spectrum shape (i.e. away from the "constant acceleration" portion of the spectra).

4.6.5 Ground Motion Suite

For the generic set of ground motions used in the IDA analysis, this study uses a modified set of the ground motion suite used in Chandramohan (2016). Chandramohan (2016) employed 22 pairs of motions from the FEMA Far Field set (44 records) (FEMA, 2009) in combination with 44 spectrally equivalent long duration ($Ds_{5\text{-}75} > 25$ sec) motions, one matching each of the individual FEMA Far Field motions. Here, we add the missing orthogonal component for each of the 44 long duration motions. Distributions of *SaRatio* and $Ds_{5\text{-}75,NGA}$ from the final ground motion set are summarized in Figure 4.9 for two different versions of *SaRatio* with different periods. The target IMs for all six sites at the 975-year (diamond) and 2475-year (square) return periods are superimposed. Although the distribution of *SaRatio(0.29,0.87)* covers a range from 0.7 to 2 quite well, most sites are on the upper edge of the *SaRatio* range for the records in the IDA. The median record set duration of $Ds_{5\text{-}75,NGA}$ is 24.6 seconds, which exceeds the target durations in all cases. While Eugene has the highest target durations, San Francisco has higher expected durations than some of the subduction sites. These high durations are due to high expected magnitudes ($M_W >$ 7.2) scenarios from crustal earthquakes at close distances identified in the San Francisco hazard deaggregation. When coupling these expected hazards with Afshari & Stewart (2016) GMPE, the result is longer expected durations. Seattle has a relatively low expected duration when compared to the other sites with subduction hazards, due to a large contribution of $M_W \approx 6.5$ crustal earthquakes representing approximately 50% of its seismic hazard. However, Seattle sits atop a deep sedimentary basin, which have been known to amplify long-period frequency content (Marafi, et al., 2017). The USGS 2014 National Hazard Model (and, as a result, the deaggregations here) do not currently consider the effects of basins.

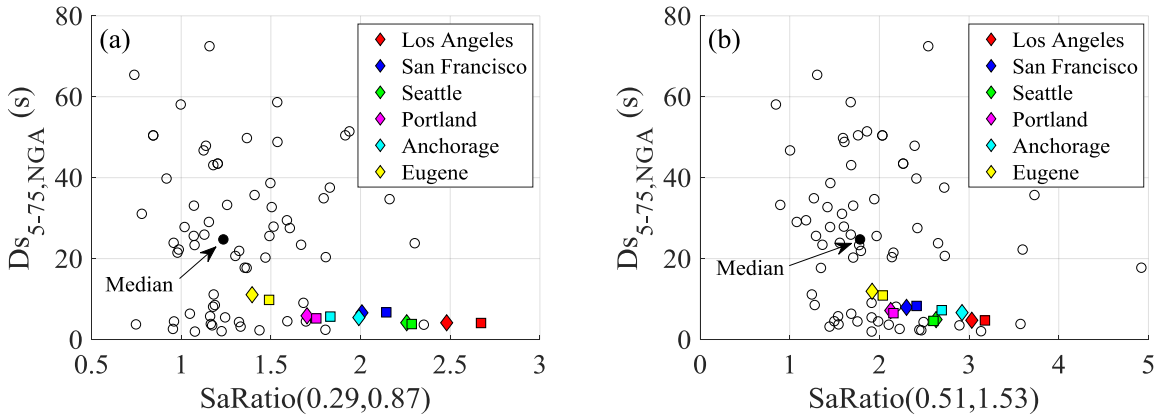

Figure 4.9. Scatter plot of $Ds_{5\text{-}75,NGA}$ vs SaRatio for all motions and target IM for each site at the 975-year (diamond) and 2475-year (square) return periods for SaRatio period ranges consistent with (a) MFD2 and (b) MFD4.

4.6.6 Hazard-Consistent Engineering Demand Parameters

The hazard-consistent IDA approach adjusts EDPs of interest from the generic IDA results using regression analysis (Zhong & Deierlein, 2018). Specifically, a multivariate linear regression analysis is carried out between each EDP (at each hazard level) in natural logarithm (ln) space and *SaRatio* and $Ds_{5\text{-}75,NGA}$ for the motions used in the IDA, as shown in Figure 4.10. The results of this regression are used to produce a median EDP prediction that is conditioned on the target *SaRatio* and target $Ds_{5\text{-}75,NGA}$ at each hazard level. We carried out this regression for four EDPs in each of the two directions (SDR for each story, accelerations at each floor, residual drifts, and collapse capacities) at nine hazard levels, for all six buildings.

Linear multivariate regression (in logarithmic space) is selected as the regression technique for all EDP-*SaRatio* relationships, consistent with Chandramohan (2016) and Zhong & Deierlein (2018). This study found that linear regression fit the data reasonably well across all EDP and intensity levels, considering the R^2 statistic. However, if different regression techniques are used between different EDP, intensity levels, or structure types, better fits of the data could potentially be attained.

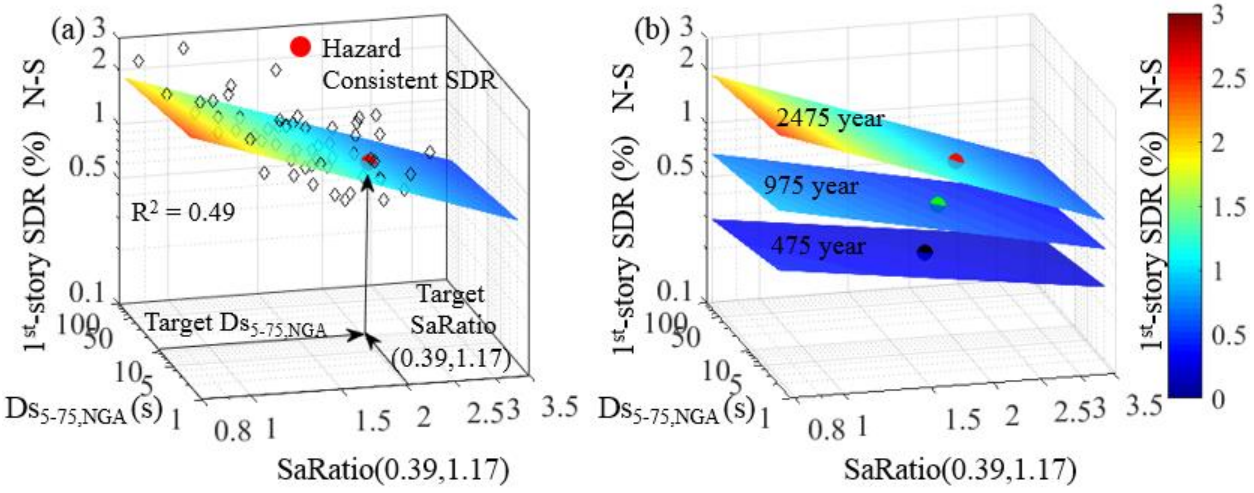

Figure 4.10. Illustration of hazard-consistent IDA approach for adjusting EDPs showing for COM2 in Eugene: (a) regression between *SaRatio*, $Ds_{5\text{-}75,NGA}$ and first-story SDR (N-S direction) at the 2475 year hazard level, and (b) results of regressions for 475, 975 and 2475 hazard levels.

For SDR, we use a bilinear rather than linear regression approach. Trends between SDR and SaRatio at the 2475-year hazard level are shown in Figure 4.11 for MFD1. A linear regression (in log space) does not fit the data very well. Note that many of the target *SaRatio* occur at *SaRatio > 1.5*, increasing the importance of a good fit in the tail of the regression. SDR that are based on linear regression can be underestimated at these high target *SaRatio*. In all cases, we observe a flattening out of SDR at very high values of *SaRatio*. Physically, the spectra are becoming so peaked, with little energy at periods surrounding T_1, such that small changes in SaRatio are not very significant and $Sa(T_1)$ is the more important IM. The bilinear algorithm works by selecting the point in the data which produces the two linear regressions to the left and right with the minimum root mean square error. Here, the kink point is restricted to ensure that it is in the middle 80% of the data. For each building, and each hazard level, the kink point is calculated for 1st-story SDR at each hazard level in both the E-W and N-S directions. The maximum kink point is then selected as the lowest *SaRatio* used in the SDR regressions, meaning that only the right side of the

bilinear regression is used. For buildings with lower overstrengths, this bilinear nature of the trend is not as prominent, and the data behaves better for a linear regression. For these cases, both sides of the regressions are very similar, indicating the bilinear regression is not needed, and linear regression using the entire data set is conducted, as shown in Figure 4.10 for COM2. In all cases, the target *SaRatio* are greater than the calculated kink point. The inclusion of this bilinear fit strategy does suggest that there are potential other regression methods that could capture the trends of the data more efficiently when considering each EDP, building and intensity level individually.

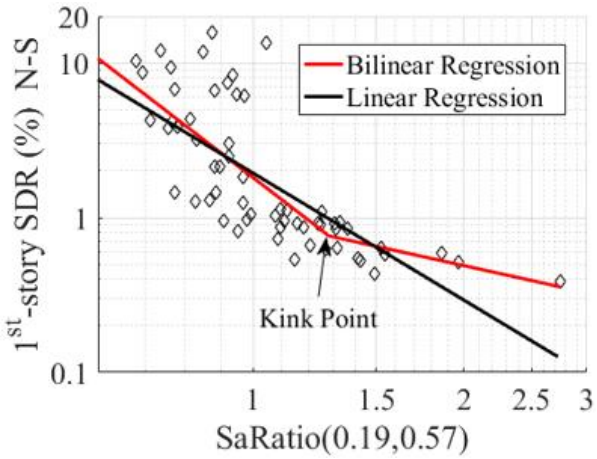

Figure 4.11. Illustration of bilinear regression technique (MFD1, 2745-year hazard level) used in the conditioning of some of the SDRs for hazard-consistent losses.

We also quantify the uncertainty in the obtained hazard-consistent EDP, considering the record-to-record variability, i.e. the uncertainty about the regression. As shown in Chandramohan (2016), the uncertainty of the EDP conditioned on *SaRatio* for each hazard level is calculated using Equation 4.2,

$$\sigma = \sqrt{\frac{RSS}{N_{gm}-3}} \tag{4.2}$$

where RSS is the sum of the squares of the residuals, N_{gm} is the number of ground motions used in the analysis, and 3 represents the number of unknown coefficients in the regression equation. We also examined how the uncertainty in the target *SaRatio* might influence our assessment of the uncertainty in the EDP. Ultimately, the uncertainty in the target ratio (on the order of 0.2 for a logarithmic standard deviation) was not found to significantly influence the results.

For loss assessment, the Seismic Performance Prediction Program (SP3) (Haselton Baker Risk Group, LLC, 2018) takes as input a vector of structural analysis results for each hazard level and EDP of interest. This vector traditionally includes the structural response results for each ground motion run in the analysis. Here, the median and standard deviation of the EDP and an assumed lognormal distribution are used to produce 1000 EDP realizations for each hazard level. This method is employed because the hazard-consistent IDA method only produces a median EDP along with σ for each hazard level. 1000 realizations are generated to ensure the median and spread of distribution is captured in the SP3 inputs (but not correlations in EDPs). These realizations provide the basis for SP3's Monte Carlo simulations.

4.7 HAZARD-CONSISTENT COLLAPSE CAPACITIES

In this section, median collapse capacities for each building are presented considering the expected seismic hazard, quantified by $SaRatio(T_1,3T_1)$ and $Ds_{5\text{-}75,NGA}$ at each site. These values are calculated following the procedure depicted in Figure 4.10, but using $Sa(T_1)$ at collapse as the EDP of interest. For the purpose of examining collapse, Target $SaRatio(T_1,3T_1)$ and $Ds_{5\text{-}75,NGA}$ were taken to be the values calculated at the 10,000-year return period. Chandramohan et al. (2018) suggests using deaggregations from an intensity level equal to $2.2 \times MCE_R$, which corresponds to the median collapse capacity for a newly designed Risk Category I and II structure based on the

assumed fragilities in the *2015 NEHRP Provisions* (FEMA, 2015). As all buildings were designed to the same level (S_{DS} = 1.0g), they all have the same design MCE_R value (S_{MS} = 1.5g). The shaking intensity at 2.2 × MCE_R is therefore equal to 3.3g for all buildings. This 2.2 × MCE_R value exceeds the 10,000-year return period shaking intensity (the limit of deaggregations provided by the 2014 USGS Hazard Model) for all buildings at all sites, so we use the 10,000-year period deaggregation. This approach is a simplification because each part of the collapse fragility curve should appropriately be adjusted with the target IMs at that intensity level (Chandramohan, 2016); however, Chandramohan et al. (2018) showed that the stripe level adjustments for collapse capacities are sufficient.

Figure 4.12 shows the multivariate linear regression in natural logarithm (ln) space between the collapse capacity of MFD2, quantified at Sa(T=0.29s), and *SaRatio(0.29,0.87)* and $Ds_{5\text{-}75,NGA}$ of the record set. In Figure 4.12(b) and (c), the regression is performed separately on each IM. As shown in Figure 4.12(b), collapse capacity is correlated strongly with *SaRatio* (R^2=0.58). This strong correlation with *SaRatio(T_1,3T_1)* was observed for all buildings (R^2 > 0.68 for MFD4, COM1, COM2, and COM4). However, MFD1 did not correlate as well with *SaRatio* (R^2=0.2), due to its high overstrength and large pre-collapse deformation capacity when compared to the other buildings. The low seismic weight and large lateral resistance of MFD1 allows the building to sustain very high drifts before collapse, which led to a high variability in collapse Sa(T=0.19s) for MFD1. The median maximum collapse drift at the scale level before collapse of MFD1 is 28.5%, while the average median maximum pre-collapse drift for the other five buildings is 5.3%. MFD1 has a much lower risk of sidesway collapse which is the dominant mechanism in light-frame wood buildings. Multiple studies, e.g., Chandramohan (2016) and Raghunandan & Liel (2013), have shown that an increase in ductility (now using this definition) corresponds to a

stronger correlation with spectral shape and duration. However, MFD1 seems to show opposite trends, indicating more research in needed into its structural response and the collapse criteria used.

In Figure 4.12(c), correlations between collapse capacity and $Ds_{5\text{-}75,NGA}$ were much lower for all buildings ($R^2 < 0.05$). This weak correlation is due to the relatively low ductility of these buildings when compared to other RC and steel building examined in Chandramohan (2016) and Raghunandan & Liel (2013) ($\mu_T \approx 15$). Both Chandramohan (2016) and Raghunandan & Liel (2013) found that duration effects decreased significantly if buildings were relatively less ductile.

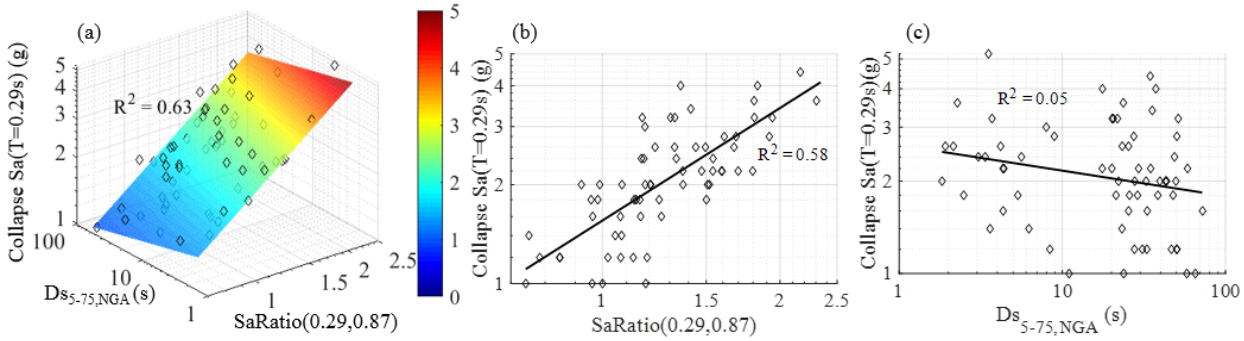

Figure 4.12. Regression between collapse capacity for MFD2 and (a) both *SaRatio(0.29,0.87)* and $Ds_{5\text{-}75,NGA}$, (b) only *SaRatio(0.29,0.87)*, and (c) only $Ds_{5\text{-}75,NGA}$ independently.

According to this methodology, hazard-consistent collapse values for each building at each site are generated, as summarized in Table 4.8. The unadjusted collapse capacities – reported in Table 4.8 – align with the buildings' overstrengths (Table 4.2 ;Figure 4.7). For each building individually, the hazard-consistent collapse capacities at all sites is higher than the unadjusted collapse capacities. In interpreting these values, it is important to note that each building design is constant across each site and does not vary according to the design values at the site. As a result of the strong correlation with *SaRatio*, the adjustment in expected collapse $Sa(T_1)$ is highly dependent on the target *SaRatio*(T_1,$3T_1$), which are reported in Table 4.8. In all cases, the median

SaRatio(T_1,3T_1) of the record set used in the IDA is lower than the target *SaRatio(T_1,3T_1)*. Therefore, adjustments shift to target higher, less damaging values *SaRatio(T_1,3T_1)*, resulting in a higher collapse capacity in terms of Sa(T_1). When comparing the hazard-consistent median collapse Sa(T_1) between sites for the same building, the results are ranked in the same order as the target *SaRatio(T_1,3T_1)* shown in Table 4.8. As reported, Eugene, Anchorage, and Portland have the lowest *SaRatio* for all of the buildings. These low *SaRatio* are due to large subduction contributions to the hazard at each site, providing more energy are longer spectral periods and flattening the expected spectra. Eugene and San Francisco have the longest expected durations, but for different reasons at the two sites. Eugene has a long target duration due to large magnitude interface earthquakes (M_W 9.0) at intermediate distances (R = 73 km) dominating the hazard. Meanwhile, San Francisco has large magnitude crustal earthquakes (M_W 7.5) at relatively close distances (R = 13 km) dominating the hazard. In comparison, Seattle has a relatively short predicted $Ds_{5\text{-}75,NGA}$ due to contribution of relatively lower magnitude crustal earthquakes (M_W 6.8) at relatively close distances (R = 6 km). However, duration has a weak correlation on collapse capacity as shown in Figure 4.12.

Table 4.8. Hazard-consistent median collapse capacities for all buildings at all sites, based on target *SaRatios* and $Ds_{5\text{-}75,NGA}$ at the 10000-year return period hazard level. $Ds_{5\text{-}75,NGA}$ is abbreviated as Ds.

Building	MFD1 (T_1=0.19s)			MFD2 (T_1=0.29s)			MFD4 (T_1=0.51s)			COM1 (T_1=0.33s)			COM2 (T_1=0.39s)			COM4 (T_1=0.62s)		
	SaRatio	***Ds* [s]**	**Col. Sa(T_1) [g]**	***SaRatio***	***Ds* [s]**	**Col. Sa(T_1) [g]**	***SaRatio***	***Ds* [s]**	**Col. Sa(T_1) [g]**	***SaRatio***	***Ds* [s]**	**Col. Sa(T_1) [g]**	***SaRatio***	***Ds* [s]**	**Col. Sa(T_1) [g]**	***SaRatio***	***Ds* [s]**	**Col. Sa(T_1) [g]**
Los Angeles	2.7	3.8	13.2	3.0	4.0	6.1	3.5	4.7	3.0	3.3	4.1	6.1	3.8	4.2	4.4	4.2	4.8	2.3
San Francisco	2.2	6.1	10.8	2.3	6.9	4.4	2.6	8.9	2.1	2.6	7.1	4.2	2.9	7.3	3.1	3.0	9.3	1.6
Seattle	2.2	3.2	11.4	2.3	3.5	4.6	2.6	4.2	2.1	2.6	3.5	4.5	3.1	3.6	3.5	3.3	4.3	1.7
Portland	1.7	4.0	9.0	1.9	4.5	3.5	2.3	5.6	1.7	2.1	4.5	3.3	2.6	4.6	2.6	2.8	5.7	1.5
Anchorage	1.4	3.9	7.9	1.6	5.3	2.9	2.5	7.5	2.0	1.9	5.4	2.8	2.3	5.6	2.3	3.2	7.8	1.7
Eugene	1.4	7.8	7.6	1.6	8.5	2.9	2.2	9.8	1.8	1.9	8.7	2.8	2.3	8.9	2.3	2.8	10.1	1.5
Unadjusted	--	--	5.9	--	--	2.1	--	--	1.4	--	--	1.8	--	--	1.4	--	--	1.0

As mentioned previously, Seattle sits atop a deep sedimentary basin. This type of basin is known to amplify long-period frequency content (Marafi, et al., 2017). Recently, the M9 Project investigated a scenario M_W 9.0 interface earthquake striking off the coast of Oregon and Washington. 3D synthetic ground motions were generated from 30 rupture scenarios with varying hypocenters and slip distributions. Median acceleration response spectra for sites inside and outside the Seattle Basin are reported in Frankel et al. (2018). Here, we calculated representative *SaRatio(0.2,0.6)* to be 0.91 and 0.88, respectively. Similarly, for *SaRatio(0.5,1.5)*, 1.07 and 1.73 are calculated for sites inside and outside of the Seattle Basin, respectively. These results indicate a scenario M_W 9.0 interface earthquake would result in more damaging *SaRatio* (both inside and outside the Seattle Basin) than predicted in the 10000-year hazard level as determined by the 2014 USGS Hazard Model (*SaRatios* of 2.2 and 2.6), and that response inside the basin would be particular damaging for the longer period structures. Results also indicate that when periods larger than ~1.0s are considered in the target *SaRatio*, the effects of basin amplification are much more pronounced. This trend is consistent with Marafi et al. (2017) and Frankel et al. (2018), who determined basin amplification is most significant for periods great than 1 second. Why does this scenario appear so damaging relative to the hazard-consistent analysis? In the 10000-year deaggregation in Seattle, a M_W 9.1 interface earthquake with a 96 km rupture distance has a ~10% contribution to the total hazard (Petersen, et al., 2014; USGS, 2018). In the deaggregation, this event has a relatively low *SaRatio* and long duration, but this is weighted with other scenarios. The durations are also particularly long for a M_W 9.0 interface scenario (both inside and outside the Seattle Basin). Frankel et al. (2018) expects $Ds_{5\text{-}95}$ of approximately 100 seconds, while, for the same scenario, Walling et al. (2018) expects a $Ds_{5\text{-}75,NGA}$ of approximately 16 seconds, both

substantially longer than the expected $Ds_{5\text{-}75,NGA}$ of 3.2s - 4.3s weighting all source types for the 10000-year return period shown in Table 4.8. Frankel et al. (2018) also notes that there was no significant amplification of duration from basin effects while using the $Ds_{5\text{-}95}$ duration metric. These results suggest amplification from basins should be taken into consideration when determining target *SaRatio* for Seattle and other sites with known basins such as Los Angeles and San Francisco. This study does not consider the effects of basins but notes that amplification procedures have been developed in Marafi et al. (2017).

4.8 MODIFICATION FACTORS TO DESIGN VALUES TO ACHIEVE UNIFORM COLLAPSE RISK

Chandramohan (2016) and Chandramohan et al. (2018) proposed a framework for development of modification factors to account for spectral shape and ground motion duration in the Equivalent Lateral Force (ELF) procedure of ASCE 7 (ASCE, 2016). The procedure identifies two modification factors, one for spectral shape (k'_{ss}) and one for duration effects (k'_{dur}), to be applied to the design base shear as shown in Equation 4.3,

$$V = k'_{ss} k'_{dur} C_s W \tag{4.3}$$

where V is the design base shear, C_s is the seismic response coefficient based on mapped values in ASCE 7 and W is the seismic weight. Equations 4.4 and 4.5 report the necessary calculations to develop k'_{ss} and k'_{dur}:

$$k'_{ss} = \left(\frac{SaRatio^{ref}}{SaRatio^{site}}\right)^{c_{ss}} \tag{4.4}$$

$$k'_{dur} = \left(\frac{Ds^{ref}}{Ds^{site}}\right)^{c_{dur}} \quad (4.5)$$

In these equations, $SaRatio^{site}$ and Ds^{site} are the median expected $SaRatio(T_1,3T_1)$ and $Ds_{5\text{-}75,NGA}$, conditional on the exceedance of the ground motion intensity corresponding to 2.2 × MCE_R at the site under investigation. $SaRatio^{ref}$ and Ds^{ref} are the corresponding values at a reference site. Consistent with Chandramohan (2016) and Chandramohan et al. (2018), our Los Angeles site is identified as the reference site, and the San Francisco site is also considered. The implications of this choice are described later.

c_{ss} and c_{dur} are coefficients that quantify the sensitivity of a structure to the effects of response spectral shape and duration, respectively. c_{ss} and c_{dur} are developed through multivariate regression between the $SaRatio(T_1,3T_1)$ and $Ds_{5\text{-}75,NGA}$ of the records and collapse capacities (reported in Appendix A.5, and illustrated for MFD2 in Figure 4.12), as shown in Equation 4.6:

$$\ln Sa(T_1)\ at\ collapse = c_0 + c_{ss} \ln SaRatio(T_1, 3T_1) + c_{dur} \ln Ds_{5-75,NGA} \quad (4.6)$$

Figure 4.13 plots the c_{ss} and c_{dur} factors from buildings analyzed in Chandramohan (2016), which included four different building types: ductile RC moment frames (MF), ductile steel MF, steel concentrically braced frames (SCBF), and buckling restrained braced frames (BRBF). In each case, c_{ss} and c_{dur} are plotted with respect to building period. Chandramohan (2016) investigated c_{ss} and c_{dur} factors correlations with ductility, fundamental period, number of stories, and ultimate roof drift ratio. That study found c_{ss} and c_{dur} correlated best with a structure's fundamental period and selected it as the structural parameter to use. This study also uses this criterion, consistent with Chandramohan (2016). The six buildings analyzed in this study are provided on the same plot.

These results show that light-frame wood buildings analyzed in this study follow the trends of the other buildings analyzed in Chandramohan (2016) well. The exception is MFD1, which exhibited much lower correlation between collapse capacities and *SaRatios*. An updated regression of c_{ss} on period was developed using the results from this study. Ultimately, the new regression was very similar to that previously developed by Chandramohan (2016). Due to the good agreement with the other buildings and regression developed in Chandramohan (2016), this study uses this regression for the calculation of c_{ss}.

Figure 4.13(b) shows the correlation between c_{dur} and building period. The light-frame wood buildings in this study do not follow the same trends as the other four structure types. This outcome is expected, as the R^2 between collapse $Sa(T_1)$ and $Ds_{5\text{-}75,NGA}$ are weak, which we attribute to the structures' relatively lower ductility. Accordingly, we do not develop k'_{dur} factors for use in ASCE 7 for these buildings, as it is evident that duration is not a strong predictor of structural response for buildings with these levels of ductility. The average ductility of the buildings used in Chandramohan (2016) is 8.5, while the average ductility of structures in this study is 4.6.

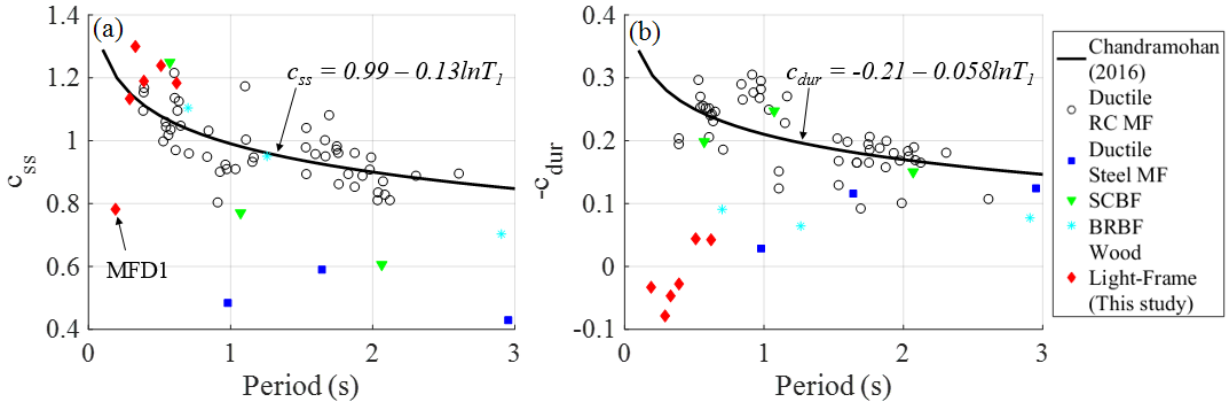

Figure 4.13. Regression-based (a) c_{ss} and (b) $-c_{dur}$ factors for multiple structure types.

Table 4.9 shows the 10000-year return period hazard level and MCE_R target *SaRatio* and resulting k'_{ss} for all of the sites. The target *SaRatio* in Los Angeles for both conditioning intensity

levels are greater than those at other sites for both conditioning periods of 0.2s and 0.5s, implying that Los Angeles has an anticipated more peaked spectra than any other site. Since Los Angeles is selected as the reference site, k'_{ss} values for all other sites are greater than 1.0, suggesting an increase in design base shear due to the lower expected *SaRatio*. The sites with the largest subduction hazard contributions (Portland, Anchorage, and Eugene) have the largest k'_{ss} due to low expected *SaRatio.* The 10000-year hazard level adjustment suggests increases in design base shear by up to 127% in Eugene. Sites with large contributions from crustal hazards, San Francisco and Seattle, also have expected increases in design base shear, represented by $k'_{ss} > 1$.

The 2.2 × MCE_R conditioning intensity level is a simplification of the full reliability approach focused on adjusting the expected median of the fragility curve. We also investigate using MCE_R intensity level deaggregation and k'_{ss} factors, as an alternative to the 2.2 × MCE_R (Chandramohan, 2016; Chandramohan, et al., 2018). Chandramohan (2016) compared expected collapse capacities of an eight-story RC moment frame from multiple methods including MSA, hazard-consistent IDA using the full risk integral, and other simplified methods. That study identified 2.2 × MCE_R to be the best conditioning intensity to achieve the most similar collapse capacity between each simplified method and the collapse capacity determined by the full risk integral for the buildings they examined. The MCE_R intensity level corresponds more toward design intensity levels, which typically have a larger contribution to the total risk of collapse when convolving the hazard curve with the fragility curve (Luco, et al., 2007). In addition, ASCE 7 risk targets, i.e. 1% chance of collapse in 50 years, are based on the total risk integral and consider a structural fragility anchored at a 10% probability of collapse at the MCE_R intensity level (ASCE, 2016). In terms of total risk, intensity levels seen at the median of the fragility curve contribute relatively little due to the low probability of these ground motions, motivating our investigation of

another intensity here. k'_{ss} is lower if based on MCE_R intensity level deaggregations and targets, compared to k'_{ss} conditioned on the 10000-year return period ($2.2 \times MCE_R$), suggesting that design base shears would require less of an increase when targeting MCE_R level shaking rather than median collapse level shaking. This difference in k'_{ss} between the two cases highlights the importance of the selection of the intensity level to upon which to condition k'_{ss} in this framework.

Table 4.9. Calculated k'_{ss} factors for 0.2s and 0.5s, when computed using the 10000-year hazard level and hazard level associated with the MCE_R intensity at each site for two reference sites.

				Site^{ref} = Los Angeles		**Site^{ref} = San Francisco**	
Site	**Period (T_1) [s]**	**10000-yr Target *SaRatio***	**MCE_R Target *SaRatio***	**10000-yr k'_{ss}**	**MCE_R k'_{ss}**	**10000-yr k'_{ss}**	**MCE_R k'_{ss}**
Los Angeles	0.2	2.7	2.2	1.0	1.0	0.8	0.8
	0.5	3.5	3.3	1.0	1.0	0.7	0.8
San Francisco	0.2	2.2	1.9	1.3	1.2	1.0	1.0
	0.5	2.6	2.6	1.4	1.3	1.0	1.0
Seattle	0.2	2.2	2.1	1.3	1.1	1.0	0.9
	0.5	2.6	2.6	1.4	1.3	1.0	1.0
Portland	0.2	1.7	1.7	1.8	1.4	1.3	1.2
	0.5	2.3	2.3	1.6	1.5	1.2	1.1
Anchorage	0.2	1.4	1.5	2.2	1.6	1.7	1.3
	0.5	2.5	2.6	1.5	1.3	1.1	1.0
Eugene	0.2	1.4	1.4	2.3	1.8	1.7	1.5
	0.5	2.2	2.2	1.6	1.6	1.2	1.2

Table 4.9 shows the 10000-year return period hazard level target *SaRatio* and resulting k'_{ss} considering San Francisco as the reference site as an alternative to Los Angeles. The trends are similar when considering either Los Angeles and San Francisco site. However, because San Francisco has a lower target *SaRatio* than Los Angeles, k'_{ss} in all cases is lower. With San Francisco as a reference site, in Los Angeles and Seattle, $k'_{ss} < 1.0$, suggesting that design base shears can be decreased. In this case, the increase in Eugene would be up to 70%.

The selection of a reference site is critical to the development of k'_{ss} factors. This importance is reflected in a 34% increase in k'_{ss} for 0.2s in Eugene when choosing Los Angeles over San Francisco as a reference site considering the 10000-year adjustment. Both Los Angeles and San Francisco are investigated as potential reference sites because their crustal seismic environment is similar to that considered in the development of modern codes and the target risk levels (FEMA, 2009). However, even though both sites' seismic hazard is completely crustal in nature, they have significantly different target *SaRatio* as shown Table 4.9. The original fragility curves and uniform risk targets for ASCE 7 (2016) are based on FEMA P-695. To develop the target fragility curves, FEMA P-695 (2009) developed a spectral shape factor (SSF) considering expected ε at various sites in California. The study found ε(1.0s) at the 0.5% in 50-year hazard level to be approximately 1.7 in Los Angeles and 1.9 in San Francisco. The final ε(1.0s) values used for SDC D in FEMA P-695 were 1.39 and 1.45 (depending on a site's S_1), which are closer to the expected hazard in Los Angeles. The ε values gathered from deaggregation in this study also reflect this trend. However, even though Los Angeles has lower expected ε than San Francisco, it has a higher (more peaked) target *SaRatio* as shown in Table 4.9, which implies that the measure used to quantify spectral shape may have a significant bearing on the outcome. To investigate the trends vis a vis FEMA P-695, we also quantified the ratio between the hazard-consistent collapse capacities and the unadjusted collapse capacities considering just the 22 FEMA Far Field record pairs in this study. These ratios provide an approximate comparison to the SSF from FEMA P-695 (2009) because spectral shape (*SaRatio*) is the dominating factor in the hazard-consistent correction. A ratio of 2.56 was calculated for Los Angeles and 1.72 was calculated for San Francisco. When comparing these ratios to the FEMA P-695 SSF for a building with similar characteristics (i.e., $\mu_T = 4$ and $T_1 \leq 0.5$s), the SSF is 1.22, suggesting a closer comparison to San Francisco. From these

results, either Los Angeles or San Francisco could be selected as a viable reference site based on comparison to the ε or approximate SSF from FEMA P-695 (2009).

4.9 HAZARD-CONSISTENT SEISMIC LOSSES

In this section, hazard-consistent seismic losses are presented. The SP3 software (Haselton Baker Risk Group, LLC, 2018) is used to estimate seismic loss. SP3 takes as input a vector of structural analysis results for each hazard level and EDP of interest. This vector traditionally includes the structural response results for each ground motion run in the analysis. Here, the median and standard deviation of the hazard-consistent EDP and an assumed lognormal distribution are used to produce 1000 EDP realizations for each hazard level. Hazard-consistent EDPs are developed according to the methods discussed in Figure 4.10. SP3 takes structural EDP inputs and develops correlations between them to build probabilistic models of structural response for use in Monte Carlo analysis. In this study, only mean loss curves are reported which limits the significance of the correlations between EDP (our correlations are unrealistic because of how hazard consistent IDA was carried out). Each building component has associated fragilities representing damage states which are linked to repair strategies, and ultimately expected loss. Losses from each component are combined to project total seismic losses. Losses due to probability of collapse and demolition due to the exceedance of 1% residual drift are also included in the loss analysis. The total replacement costs of each building, as calculated in SP3 based on RS Means, are reported in Table 4.10. These values indicate that the commercial archetypes have overall higher replacement cost compared to the multifamily dwellings. The commercial buildings have more expensive components and, on average, have higher costs per square foot compared to the multifamily units.

Table 4.10. Total Replacement cost for each building.

Building	Total Replacement Cost [Dollars]
MFD1	790,000
MFD2	1,580,000
MFD4	4,020,000
COM1	1,120,000
COM2	2,250,000
COM4	4,500,000

Hazard-consistent seismic losses are generated and shown in Figure 4.14, for all six buildings at all six sites. The regression between the various EDPS and the IMs indicate that is *SaRatio* is more important than duration in determining seismic losses. Thus, the reducing adjustments to EDPs to be hazard-consistent are most significant for the crustal sites with the more peaked *SaRatios*. As a result, the sites that had the largest subduction contributions to the total seismic hazard (Portland, Anchorage, and Eugene) had the highest expected total loss due to lower target *SaRatios*. For MFD2, in Figure 4.14(c), the target *SaRatio(0.29,0.87)* in Eugene at Sa(T=0.29s) = 1.26g is 1.63, while for the same intensity, the target *SaRatio(0.29,0.87)* = 2.30 in Seattle and approximately 2.55 in Los Angeles. At this intensity level, the expected seismic losses in Eugene are approximately 32% greater than in Los Angeles and 45% greater than in Seattle for MFD2. The difference in loss increases between subduction and crustal sites at higher intensities.

Anchorage is now compared to Los Angeles because it has higher expected intensities when compared to Eugene for the same hazard level. At an intensity level of Sa(T=0.29s) = 2.0g, MFD2 in Anchorage has a target *SaRatio(0.29,0.87)* = 1.63, and 2.82 in Los Angeles. This difference corresponds to 46% higher estimated loss for MFD2 in Anchorage than in Los Angeles. These differences are more apparent for the stronger buildings (Figure 4.14(a-c)). In these buildings, losses are controlled more by shear wall components, which have a higher variability in potential loss, and not collapse or residual drift, which have a less variable loss (total replacement

cost). For non-collapse scenarios, components such as the shear walls consider uncertainties in the EDP, the component fragility, and repair cost. Furthermore, the total variability in loss is increased due to multiple components contributing to the overall loss. Residual drift and collapse have one expected loss and have the largest contribution to the total loss for buildings with lower overstrengths, decreasing the uncertainty. Therefore, buildings with lower overstrengths (i.e. MFD4, COM2, and COM4) are more susceptible to losses due to residual drift and collapse at lower intensity levels, bringing the loss estimates closer together (Figure 4.14(d-f)).

Figure 4.15(a) and (b) shows deaggregated losses in Anchorage for MFD2 and COM2, respectively. For both buildings, at $Sa(T_1)$ below 0.7g, seismic loss is governed by the shear wall and partition wall elements, which is a function of the hazard-consistent drift. Losses due to shear walls and partition walls are higher in MFD2 because the multifamily archetypes have more walls than the commercial archetypes. At higher intensities, greater than $Sa(T_1)$ = 1.3g, losses due to residual drift and collapse contribute the most to the total loss. COM2 has a lower overstrength than MFD2 and, therefore, expected losses due to collapse and residual drift begin to govern at a lower $Sa(T_1)$. The overall higher probability of collapse and losses due to residual drift in COM2 result in higher expected losses when compared to MFD2. Figure 4.14(a) shows estimated losses in MFD1 are lower than those for all other buildings. The high very high overstrength of MFD1 results in reduced expected losses due to a lower probability of collapse and demolition due to residual drifts. MFD1 also has a higher stiffness than the other buildings, resulting in lower drifts for a given $Sa(T_1)$, and lower expected non-collapse contributions to losses by extension.

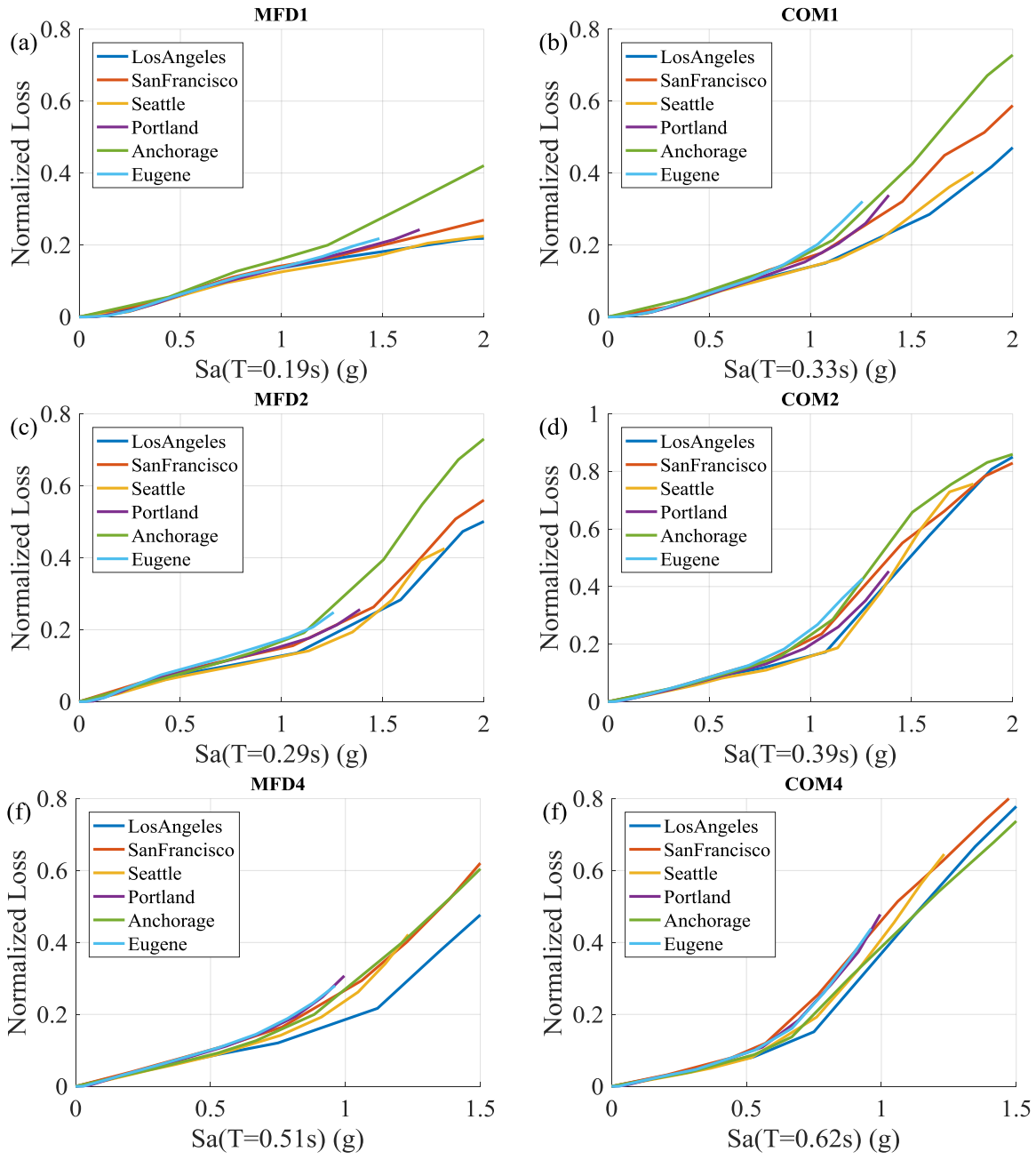

Figure 4.14. Mean hazard-consistent loss, normalized by the replacement cost of the cost of the building plotted as a function of each building's Sa(T_1): for (a) MFD1, (b) COM1, (c) MFD2, (d) COM2, (e) MFD4, and (f) COM4.

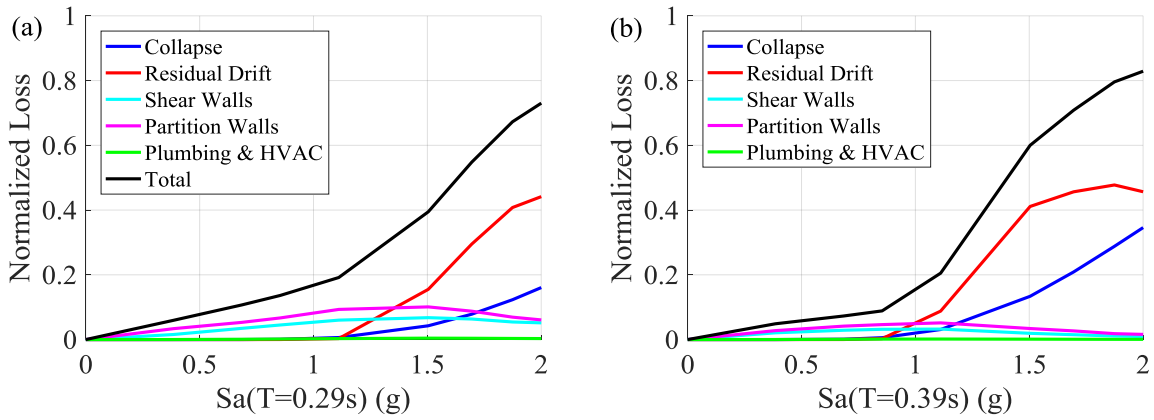

Figure 4.15. Mean hazard-consistent loss, deaggregated by building component and normalized by building replacement cost in Anchorage, for: (a) MFD2 and (b) COM2.

Figure 4.16 compares the expected seismic loss for MFD2 in Anchorage, San Francisco and Los Angeles as a function of hazard level; similar trends are observed for the other buildings (not shown). Although this comparison is not completely consistent, because each site has a different expected Sa(T=0.29s) at each hazard level, interesting comparisons can still be made between the three sites. Anchorage and San Francisco have similar expected Sa(T=0.29s) at each hazard level, with the biggest difference being 26% (0.08g) at the 75-year return period. Los Angeles has higher expected intensities at hazard levels above the 975-year return period when compared to Anchorage and San Francisco, with the largest difference being 20% (0.43g) at the 10000-year return period. At all hazard levels, MFD2 in Anchorage has a higher expected loss than in San Francisco or Los Angeles. The difference in expected losses between Anchorage and Los Angeles or San Francisco is due to the difference in seismic environment, and, as a result, the lower expected *SaRatio* in Anchorage compared to San Francisco or Los Angeles, resulting in a smaller adjustment in EDPs in the hazard-consistent adjustment and, thus, greater losses. When comparing Anchorage to Los Angeles, Anchorage still has larger expected seismic loss, despite Los Angeles having a higher expected Sa(T=0.29s) at hazard levels greater than 975 years,

indicating the more damaging seismic environment in terms of spectral shape and durations in Anchorage, which outweighs the higher expected Sa(T_1) in Los Angeles.

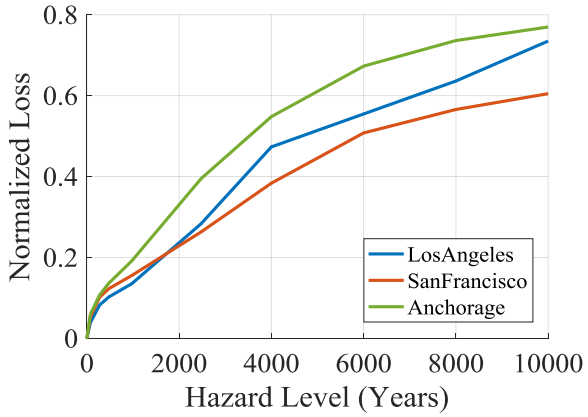

Figure 4.16. Mean total hazard-consistent loss normalized by the replacement cost of the cost for MFD2 as a function of the hazard level return period.

4.10 CONCLUSIONS

This study aims to quantify expected seismic losses and collapse capacities in light-frame wood buildings considering region-specific seismic environments. Differences in tectonic environment can greatly influence duration and frequency content of shaking and, as a result, seismic risk. One-, two-, and four-story multifamily residential and commercial light-frame wood buildings are analyzed through nonlinear dynamic simulations to estimate seismic loss and collapse risk, and to show the influence of seismic environment. The collapse assessments are used to develop spectral shape modification factors that could be used to modify design values in ASCE 7-16 to ensure uniform risk across different seismic regions. The hazard-consistent IDA methodology developed by Chandramohan (2016) is adapted.

The response of these light-frame wood buildings correlates strongly with spectral shape, quantified by *SaRatio(T_1,3T_1)*. Conversely, these assessments show only weak correlations with round motion duration, quantified by $Ds_{5\text{-}75,NGA}$. The weak correlation with $Ds_{5\text{-}75,NGA}$ is due to the

relatively low ductility of these buildings when compared to RC and steel buildings examined in other ground motion duration studies (Chandramohan, 2016; Raghunandan & Liel, 2013). Light-frame wood building response is therefore much more dependent upon the expected *SaRatio(T_1,3T_1)* at the site. rather than the combination of *SaRatio(T_1,3T_1)* and $Ds_{5\text{-}75,NGA}$. *SaRatios* tend to be higher (less damaging) at sites dominated by crustal hazards such as Los Angeles and San Francisco and lower (more damaging) at sites dominated by subduction hazards such as Eugene, Portland, and Anchorage.

As a result of these trends, sites with large contributions from subduction hazards, including Portland, Anchorage, and Eugene, have lower expected collapse capacities and higher expected seismic losses for light-frame wood buildings. For the same building, at the same hazard level, collapse capacities can differ by up to 120% as a result of spectral shape hazard factors. Similarly, corresponding losses can differ by up to 66%.

One alternative for mitigating some of these differences are design modification factors that could amplify design in places where the seismic hazard effects are more adverse for these buildings. These modifications are developed here for the ELF procedure in ASCE 7-16 (2016). These values increase design base shears by up to 130% at the site with the highest subduction contributions to the hazard (Eugene) and by up to 70% in San Francisco. The results also show that there are also important methodological choices that impact the estimated design increases. Here, we investigated the choice of the reference site and the conditioning intensity level. These are found to modify the design increase by as much as 70% (in Anchorage).

CHAPTER 5

5 CONCLUSIONS

5.1 SUMMARY

This dissertation explores the relationship between earthquake properties, ground motion characteristics, structural response, and structural design, considering the influence of regional seismic environments. Chapter 2 examines differences in structural response in induced versus tectonic ground motions, examining the impact of induced ground motions in Oklahoma and southern Kansas on a residential building chimney. A model of a residential chimney is dynamically simulated using a suite of induced ground motions and a similar suite of tectonic ground motions. Structural response is compared between the two ground motion sets to investigate how structural response differs between induced and tectonic ground motions, and what earthquake characteristics are responsible for this observed difference.

Chapter 3 examines residential multifamily light-frame wood buildings in sequences of induced earthquakes. Three-dimensional one and two-story numerical models are dynamically analyzed in sequences of induced ground motions, employing the hazard-consistent incremental dynamic analysis methodology (Chandramohan, 2016) and assembly-based seismic loss estimation (FEMA, 2012) procedures to investigate damage and damage accumulation in the buildings. The goals of this study are to quantify expected damage and seismic loss in light-frame wood construction in induced earthquakes and investigate how these parameters change throughout induced earthquake sequences.

Chapter 4 exercises a framework to quantify how extended ground motion durations can influence building fragilities and, ultimately, explores how we might modify seismic codes to better incorporate this seismic risk. Three-dimensional, multifamily and commercial building

numerical models are dynamically analyzed using the hazard-consistent IDA methodology developed by Chandramohan (2016). Period and site dependent modification factors are developed for use in current seismic design provisions to ensure target performance goals are achieved. Furthermore, hazard-consistent seismic collapse capacities and seismic losses are also presented.

The research presented in Chapter 2, Chapter 3, and Chapter 4 aims to fill gaps in existing literature by quantifying how building response, damage, seismic loss, and building design are all impacted by expected ground motion characteristics in different regions across the United States. In Oklahoma, induced earthquakes, caused by wastewater injection, are the dominant seismic hazard. Meanwhile, large crustal earthquakes dominate the hazard in California and large subduction earthquakes are responsible for the majority of seismic hazard in Cascadia. Some locations, like Seattle, have significant crustal and subduction hazards. The various ground motions produced from these earthquakes impact each of their regions differently. This study explores especially the impact of ground motion duration and frequency content. The effects of spectral shape and duration are considered in terms of their implications for collapse risk targets across different sites and in terms of their influence on seismic loss.

5.2 MAJOR CONTRIBUTIONS

The findings presented in Chapter 2 showed that induced ground motions are less damaging than tectonic ground motions of similar intensity. The difference in collapse capacity is larger for more ductile structures and less significant for more brittle structures. The differences observed between tectonic and induced records sets is largely due to the differences in frequency content between the induced and tectonic ground motions. Ground motions originating from induced earthquakes have less energy at longer periods when compared to similar tectonic earthquakes, making them less damaging as a structure's period lengthens due to nonlinear response. Chapter 2

finds that the difference in frequency content is a product of differences in the regional seismic environment between the western and central U.S. manifested in earthquake rupture depths, stress drops, and geometric attenuation. The differences in these earthquake source characteristics are also due to the underlying physical mechanisms associated with induced and tectonic earthquakes. These findings show how ground motions with similar source characteristics (i.e. magnitude and rupture distance) can produce different structural responses.

Chapter 3 assesses damage and seismic losses for light-frame wood buildings when subjected to sequences of small to moderate magnitude events. Results show that at the observed shaking levels observed in recent earthquakes, minor damage, including the cracking of interior finishes and damage to plumbing and HVAC systems, is expected. This expected damage is consistent with reported damage sustained in the Pawnee and Cushing earthquakes. Results also indicate damage accumulation is observed over the length of a seismic sequence when damage is quantified in terms of absorbed hysteretic energy and the damage index developed by Park & van de Lindt (2009). This damage corresponds to elongation or widening of cracks. However, simulations showed that the vulnerability of the building is not significantly altered by damage in a preceding event, and losses do not change if the building is only repaired once at the end of the sequence. The worsening of damage in the initial event does not significantly alter repair strategies and expected seismic loss does not increase. However, if repairs are conducted after each earthquake in the sequence, the total seismic losses increase greatly.

Chapter 4 quantifies expected seismic loss in light-frame wood buildings considering region-specific seismic hazard that can greatly influence duration and frequency content of shaking and, as a result, seismic risk in terms of losses or collapse (i.e. life safety). Results show light-frame wood building response correlates strongly with spectral shape, but weakly with ground motion

duration. Therefore, light-frame wood building response and expected seismic loss is mostly dependent upon the expected spectral shape at a site, rather than the combination of spectral shape and duration. Sites with large contributions from subduction hazards, including Portland, Anchorage, and Eugene, have higher expected collapse risk and seismic losses for light-frame wood buildings due to flatter expected spectral shapes when compared to crustal sites such as Los Angeles and San Francisco. The chapter also leverages these results to develop site and period dependent modification factors that account for the expected spectral shape and can be used in the design base shear equations in ASCE 7 (2016). Following this trend, design base shears should be increased especially at sites with large contributions from subduction earthquakes. Increases in design base shear are dependent upon the reference site and conditioning intensity level selected and can vary between 50-130% in Eugene for T=0.2s depending on these selections.

5.3 FUTURE WORK

Although the research presented in this dissertation explores many facets of the relationships between regional seismic environments, the resulting expected ground motions, structural response, and structural design, there remain areas of research deserving of further investigation. These areas for future research are products of new questions developed from the investigations conducted in this dissertation, as well as related questions which were out of the scope of the studies pursued in this document. This section outlines future research topics that have been identified as areas where deeper investigation will aid in providing a better understanding of how regional seismic environment and the resulting ground motions can influence the built environment.

One of the main themes of this dissertation is the investigation of light-frame wood buildings in Chapters 3 and 4. All eight building designs between both chapters are for newly constructed modern buildings. These designs provide valuable insight for new construction and potential modifications to current seismic provisions and building codes. However, the majority of existing buildings in the United States are not designed and built to the current standards. In the case of Oklahoma (Chapter 3), many of the reported damage cases are for residences that are older and were not designed and built to modern provisions and codes. Further investigation into older construction would help quantify damage and loss for construction that could potential behave differently in an earthquake. Older light-frame wood buildings could potentially be less stiff and be more susceptible to strength and stiffness deterioration, increasing their seismic loss and potential for damage accumulation at lower levels of shaking than observed in Chapter 3.

Similarly, research investigating older, existing light-frame wood buildings in California and Cascadia is an area in need of further investigation. Furthermore, the examination of existing buildings can provide information pertaining to potential retrofit strategies and cost/benefit relationships of different retrofit scenarios. Seismic loss estimates would also be valuable for the design of insurance policies in regions of high hazard and risk.

Another area of future research that would help fill gaps in knowledge pertaining to induced seismicity is the investigation of the minimum shaking required to cause damage in infrastructure. The majority of the induced earthquakes are of low magnitude, with the largest being the MW 5.8 Pawnee earthquake (USGS, 2017). Low to moderate magnitude earthquakes have not been much investigated by earthquake engineers. Investigation into the minimum magnitude and distance combination that can cause significant damage to buildings and other infrastructure would aid local governments and insurance companies greatly, especially with the

elevated rates of earthquakes in the region. Khosravikia et al. (2018) developed a framework combining USGS Shakemaps from induced earthquakes in Texas and bridge damage fragilities to provide decision making criteria on which bridges were in greatest need of inspection following an earthquake event. Similarly, traffic light systems have been developed, which instruct wastewater injection well operators to decrease injection volumes and rates given the occurrence of a significant earthquake in the region. A similar methodology could be developed here, where probabilities of damage considering a magnitude distance combination could be used to inform operators and local governments of potential risk and can be used to calibrate traffic light systems.

As discussed previously, the buildings analyzed in Chapter 4 were not sensitive to ground motion duration. Our analyses indicated that this finding was due to the lower ductility ($\mu_T \approx 4$) of these buildings when compared to other buildings analyzed in previous duration studies ($\mu_T \approx 15$) (Chandramohan, et al., 2016; Raghunandan & Liel, 2013). Further investigation considering more ductile light-frame wood buildings with deformation capacities similar to Chandramohan et al. (2016) and Raghunandan & Liel (2013) would provide valuable insight to determine if the weak correlations with durations, observed in this dissertation, are a function of the structure's ductility or a function of the physical mechanisms associated with light-frame wood construction.

Lastly, the relationship between one measure of spectral shape, *SaRatio,* and seismic risk and response is investigated in Chapter 4. When investigating the correlation between SDR and *SaRatio*, we observe a flattening out of responses, i.e. story drift ratios, at very high values of *SaRatio*. Physically, the spectra are becoming so peaked, with little energy at periods surrounding T_1, that small changes in *SaRatio* are not very significant and $Sa(T_1)$ is the more important IM. Further investigation into this phenomenon would prove valuable for understanding relationships between structural response and spectral shape. Quantifying a threshold at which spectral shape or

SaRatio is no longer the dominant predictor of structure response because of the limited energy at surrounding periods would aid in providing better predictions of response, as well as adding to the wealth of knowledge already gathered linking spectral shape and structural response.

5.4 LIMITATIONS

This section identifies and discusses some limitations of the research conducted in this dissertation. In particular, consideration of soil-structure interactions, vertical ground motions, velocity pulses, and directivity effects of ground motions were not considered and are outside the scope of this research. These areas could also be investigated in addition to the topics discussed in Section 5.3.

Vertical ground motions were not considered in any of the analysis in Chapters 2, 3, and 4. Therefore, the effect of vertical induced ground motions on infrastructure in Oklahoma and in light-frame wood construction in different seismic environments in the western United States was not considered. Recent literature has shown that vertical ground motions can be helpful or detrimental to a building in terms of collapse risk (Harrington & Liel, 2016). Harrington & Liel (2016) found that vertical ground motions were most detrimental for older nonductile RC buildings or RC buildings with cantilever construction. The light-frame wood buildings examined in this study feature neither of these characteristics and are a different structural system altogether. Further investigation is needed for a reasonable assessment on the impact of vertical ground motions in the context of this study.

Earthquake directivity effects are also not considered in this dissertation. Earthquake ruptures propagating towards a site have been shown to produce higher amplitude and shorter duration ground motions when compared to a rupture propagating away from or normal to at site.

Correspondingly, an earthquake rupture propagating away from a site has been shown to produce lower amplitude but longer duration ground motions (Dziewonski, et al., 1981). In addition, directivity may be associated with velocity pulses. These effects could have a large impact on hazard-consistent target SaRatio and durations at a site. In addition, velocity pulses from ground motions also have a large impact on structural response (Baker, 2008; Champion & Liel, 2012). However, these effects are not considered in the research presented in this study.

Lastly, soil-structure interaction was also not considered in any of the modeling in this dissertation. All of the numerical models assumed a fixed base and did not consider the amplification or de-amplification of ground motions on the building due to the interaction between the soil and structure. Many studies have shown how structural response can vary greatly when considering these interactions (Wong, 1975; NIST, 2012). However, the consideration of soil-structure interaction is outside the scope of this research and is not expected to have a large influence on the results presented in this dissertation due to the relatively short periods of the buildings investigated.

BIBLIOGRAPHY

Abrahamson, N., Kuehn, N., Gulerce, Z., Gregor, N., Bozorgnia, Y., Parker, G., . . . Youngs, R. (2018). *Update of the BC Hydro Subduction Ground-Motion Model using the NGA-Subduction Dataset.* PEER.

Afshari, K., & Stewart, J. P. (2016). Physically Parameterized Prediction Equations for Significant Duration in Active Crustal Regions. *Earthquake Spectra, 32*(4), 2057-2081.

Amadio, C., Fragiacomo, M., & Rajgelj, S. (2003). The effects of repeated earthquake ground motions on the non-linear response of SDOF systems. *Earthquake Engineering & Structural Dynamics, 32*(2), 291–308.

Ancheta, T. D., Darragh, R. B., Stewart, J. P., Seyhan, E., Silva, W. J., Chiou, B. S., . . . Boore, D. M. (2013). *PEER NGA-West2 Database.* Berkeley, CA: Pacific Engineering Research Center.

Anderson, J., Burns, P., Milroy, D., Ruprecht, P., Hauser, T., & Siegel, H. (2017). Deploying RMACC Summit: An HPC Resource for the Rocky Mountain Region. *Proceedings of PEARC17.* New Orleans.

ASCE. (2010). *Minimum Design Loads for Buildings and Other Structures.* Washington DC: ASCE.

ASCE. (2016). *Minimum Design Loads for Buildings and Other Structures.* Washington DC: ASCE.

Assatourians, K., & Atkinson, G. (2018). Development of a database of response spectra and time histories for induced earthquakes. *Seismological Research Letters*, In Review.

ATC. (2018). *Active Projects*. (ATC) Retrieved November 2017, from Applied Technology Council: https://www.atcouncil.org/projects/projects-active

Atkinson, G. (2015). Ground-motion prediction equation for small-to-moderate events at short hypocentral distances, with application to induced-seismicity hazards. *Bulletin of the Seismological Society of America, 105*(2A), 981-992.

Atkinson, G., Wald, D., Worden, C., & Quitoriano, V. (2018). The Intensity Signature of Induced Seismicity. *Bulletin of the Seismological Society of America, 108*(3A), 1080-1086.

Authentic Custom Homes, Homes by Taber LLC, Silver Custom Homes, & Sun Custom Homes. (2018, January 22). Typical siding in Oklahoma. (B. Baird, & R. Chase, Interviewers)

Baker, J. (2008). Identification of near-fault velocity pulses and prediction of resulting response spectra. *Geotechnical Earthquake Engineering and Soil Dynamics IV*, 1-10.

Baker, J. (2011). Conditional Mean Spectrum: Tool for Ground-Motion Selection. *Journal of Structural Engineering, 137*(3), 322-331.

Baker, J., & Cornell, C. (2006). Spectral shape, epsilon and record selection. *Earthquake Engineering & Structural Dynamics, 35*(9), 1077-1095.

Baker, J., & Jayaram, N. (2008). Correlation of spectral acceleration values from NGA ground motion models. *Earthquake Spectra, 24*(1), 299-317.

Ballio, G., & Castiglioni, C. (1994). An approach to the seismic design of steel structures based on cumulative damage criteria. *Earthquake Engineering & Structural Dynamics, 23*(9), 969-986.

Barba-Sevilla, M., Baird, B., Liel, A., & Tiampo, K. (2018). Hazard implications of the 2016 Mw 5.0 Cushing, OK earthquake from a joint analysis of damage and InSAR data. *Remote Sensing, 10*(11), 1715.

Barrett, S. (2016). *The link between hydrofracking, wastewater injection and earthquakes: key issues for re/insurers.* Swiss Reinsurance Company.

Bitton, D. (2016, September 6). *Only minor damage at OSU following Oklahoma's largest earthquake*. Retrieved November 2016, from http://www.stwnewspress.com/news/only-minor-damage-at-osu-following-oklahoma-s-largest-earthquake/article_d78612fe-748e-11e6-89db-f707c9cfeee8.html

Bommer, J., & Martinez-Pereira, A. (2000). Strong-motion parameters: definition, usefulness and predictability. *12th World Conference on Earthquake Engineering, Auckland.* Auckland, NZ.

Bommer, J., Magenes, G., Hancock, J., & Penazzo, P. (2004). The influence of strong-motion duration on the seismic response of masonry structures. *Bulletin of Earthquake Engineering, 2*(1), 1-26.

Bommer, J., Stafford, P., & Alarcón, J. (2009). Empirical equations for the prediction of the significant, bracketed, and uniform duration of earthquake ground motion. *Bulletin of the Seismological Society of America, 99*(6), 3217 - 3233.

Bommer, J., Stafford, P., Edwards, B., Dost, B., van Dedem, E., Rodriguez-Marek, A., . . . Ntinalexis, M. (2017). Framework for a ground-motion model for induced seismic hazard and risk analysis in the Groningen gas field, the Netherlands. *Earthquake Spectra, 33*(2), 481-498.

Bradley, B. (2011). Correlation of significant duration with amplitude and cumulative intensity measures and its use in ground motion selection. *Journal of Earthquake Engineering, 15*(6), 809-832.

Calabrese, A., Almeida, J., & Pinho, R. (2010). Numerical Issues in Distributed Inelasticity Modeling of RC Frame Elements for Seismic Analysis. *Journal of Earthquake Engineering, 14*(1), 38-68.

Calderini, C., & Lagomarsino, S. (2008). A continuum model for in-plane anisotropic inelastic behaviour of masonry. *Journal of Structural Engineering, 134*(2), 209-220.

Campbell, K., & Bozorgnia, Y. (2014). NGA-West2 ground motion model for the average horizontal components of PGA, PGV, and 5% damped linear acceleration response spectra. *Earthquake Spectra, 30*(3), 1087-1115.

Casolo, S., & Pena, F. (2007). Rigid element model for in-plane dynamics of masonry walls considering hysteretic behaviour and damage. *Earthquake Engineering & Structural Dynamics, 36*(8), 1029-1048.

Çelebi, M., Bazzurro, P., Chiaraluce, L., Clemente, P., Decanini, L., DeSortis, A., . . . Milana, G. (2010). Recorded motions of the 6 April 2009 Mw 6.3 L'Aquila, Italy, earthquake and implications for building structural damage: overview. *Earthquake Spectra, 26*(3), 651-684.

Champion, C., & Liel, A. (2012). The effect of near-fault directivity on building seismic collapse risk. *Earthquake Engineering & Structural Dynamics, 41*(10), 1391-1409.

Chandramohan, R. (2016). *Duration of earthquake ground motion: Influence on structural collapse risk and integration in design and assessment practice.* Stanford University: PhD. Thesis.

Chandramohan, R. (2016). *Duration of earthquake ground motion: Influence on structural collapse risk and integration in design and assessment practice.* Stanford University: PhD. Thesis.

Chandramohan, R., Baker, J., & Deierlein, G. (2016). Quantifying the influence of ground motion duration on structural collapse capacity using spectrally equivalent records. *Earthquake Spectra, 32*(2), 927–950.

Chandramohan, R., Baker, J., & Deierlein, G. (2018). Accounting for the Influence of Ground Motion Response Spectral Shape and Duration in the Equivalent Lateral Force Design Procedure. *11th National Conference in Earthquake Engineering.* Los Angeles, CA.

Chase, R., & Liel, A. (2017). Potential for Damage to Brittle Structures in Induced Earthquakes. *World Conference in Earthquake Engineering.* Santiago, Chile.

Christovasilis, I. (2010). *Numerical and Experimental Investigations of the Seismic Response of Light-Frame Wood Structures.* Buffalo: PhD Thesis.

Clayton, P., Zalachoris, G., Rathje, E., Bheemasetti, T., Caballero, S., Yu, X., & Bennett, S. (2016). *The geotechnical aspects of the September 3, 2016 M 5.8 Pawnee, Oklahoma earthquake.* Berkeley, California: GEER Association.

Consigilio Nazionale Delle Ricerche Commissione di studio per la predisposizione e l'analisi di norme tecniche relative alle Costruzioni. (2013). *Istruzioni per la Valutazione Affidabilistica della Sicurezza Sismica di Edifici Esistenti.*

Decanini, L., Gavarini, C., & Mollaioli, F. (2000). Some remarks on the Umbria-Marche earthquakes of 1997. *European Earthquake Engineering, 14*(3), 18-48.

DeJong, M. (2009). *Seismic assessment strategies for masonry structures.* PhD Thesis.

Dziewonski, A., Chou, T., & Woodhouse, J. (1981). Determination of earthquake source parameters from waveform data for studies of global and regional seismicity. *Journal of Geophysical Research: Solid Earth, 86*(B4), 2825-2852.

Eads, L., Miranda, E., & Lignos, D. (2015). Average spectral acceleration as an intensity measure for collapse assesment. *Earthquake Engineering & Structural Dynamics, 42*(12), 2057-2073.

Eads, L., Miranda, E., & Lignos, D. (2016). Spectral shape metrics and structural collapse potential. *Earthquake Engineering & Structural Dynamics, 45*(10), 1643-1659.

Ellingwood, B., Rosowsky, D., & Pang, W. (2008). Performance of light-frame wood residential construction subjected to earthquakes in regions of moderate seismicity. *Journal of Structural Engineering, 134*(8), 1353-1363.

Ellsworth, W. L., Llenos, A. L., McGarr, A. F., Michael, A. J., Rubinstein, J. L., Mueller, C. S., . . . Calaris, E. (2015). Increasing seismicity in the U. S. midcontinent: Implications for earthquake hazard. *The Leading Edge, 34*(6), 618-626.

FEMA. (2009). *FEMA P-695 Quantification of Building Seismic Performance Factors.* Washington DC: Federal Emergency Management Agency.

FEMA. (2012). *FEMA P-58-1: Seismic Performance Assessment of Buildings. Volume 1– Methodology.* Washington, D.C.: Federal Emergency Management Agency.

FEMA. (2015). *NEHRP Recommended Seismic Provisions for New Buildings and Other Structures, Part 1: Provisions, Part 2: Commentary.* Washington, D.C.: Federal Emergency Management Agency.

Filiatrault, A., Fischer, D., Folz, B., & Uang, C. (2002). Seismic Testing of Two-Story Woodframe House: Influence of Wall Finish Materials. *Journal of Structural Engineering, 128*(10), 1337-1345.

Filiatrault, A., Isoda, H., & Folz, B. (2003). Hysteretic damping of wood framed buildings. *Engineering Structures, 25*(4), 461-471.

Folz, B., & Filiatrault, A. (2001). Cyclic analysis of wood shear walls. *Journal of Structural Engineering, 127*(4), 433-441.

Folz, B., & Filiatrault, A. (2004). *A computer program for seismic analysis of woodframe structures.* Richmond, California: Consortium of Universities for Research in Earthquake Engineering.

Folz, B., & Filiatrault, A. (2004). Seismic analysis of woodframe structures. II: Model implementation and verification. *Journal of Structural Engineering, 130*(9), 1361-1370.

Frankel, A. (2018, September). Personal Communication.

Frankel, A., Wirth, E., Marafi, N., Vidale, J., & Stephenson, W. (2018). Broadband Synthetic Seismograms for Magnitude 9 Earthquakes on the Cascadia Megathrust Based on 3D Simulations and Stochastic Synthetics, Part 1: Methodology and Overall Results. *Bulletin of the Seismological Society of America, 108*(5A), 2347-2369.

Frohlich, C., DeShon, H., Stump, B., Hayward, C., Hornbach, M., & Walter, J. (2016). A Historical Review of Induced Earthquakes in Texas. *Seismological Research Letters, 87*(4), 1022-1038.

Furumura, T., Takemura, S., Noguchi, S., Takemoto, T., Maeda, T., Iwai, K., & Padhy, S. (2011). Strong ground motions from the 2011 off-the Pacific-Coast-of-Tohoku, Japan (Mw= 9.0) earthquake obtained from a dense nationwide seismic network. *Landslides, 8*(3), 333.

Ghehnavieh, E. (2017). *Seismic Analysis of Light-Frame Wood Building with a Soft-Story Deficiency.* Clemson University. Clemson University: PHD Thesis.

Ghosh, J., Padgett, J., & Sánchez-Silva, M. (2015). Seismic damage accumulation in highway bridges in earthquake-prone regions. *Earthquake Spectra, 31*(1), 115-135.

Goda, K., & Salami, M. (2014). Inelastic seismic demand estimation of wood-frame houses subjected to mainshock-aftershock sequences. *Bulletin of Earthquake Engineering, 12*(2), 855-874.

Grigoratos, I., Bazzurro, P., Rathje, E., & Savvaidis, A. (2018). A framework to quantify induced seismicity due to wastewater. *Proceedings of the 11th National Conference in Earthquake Engineering.* Los Angeles: EERI.

Hancock, J., & Bommer, J. (2007). Using spectral matched records to explore the influence of strong-motion duration on inelastic structural response. *Soil Dynamics and Earthquake Engineering, 27*(4), 291-299.

Harrington, C., & Liel, A. (2016). Collapse assessment of moment frame buildings, considering vertical ground shaking. *Earthquake Engineering & Structural Dynamics, 45*(15), 2475-2493.

Harvey, S., Heinrich, S., & Muralleetharan, K. (2018). A Framework for Post-Earthquake Response Planning in Emerging Seismic Regions: An Oklahoma Case Study. *Earthquake Spectra, 34*(2), 503-525.

Haselton Baker Risk Group, LLC. (2018). Seismic Performance Prediction Program. Chico, California. Retrieved from http://hbrisk.com

Hatzigeorgiou, G., & Liolios, A. (2010). Nonlinear behaviour of RC frames under repeated strong ground motions. *Soil Dynamics and Earthquake Engineering, 30*(10), 1010-1025.

Hough, S. (2014). Shaking from Injection-Induced Earthquakes in the Central and Eastern United States. *Bulletin of the Seismological Society of America, 104*(5), 2619-2626.

Iervolino, I., Manfredi, G., & Cosenza, E. (2006). Ground motion duration effects on nonlinear seismic response. *Earthquake Engineering & Structural Dynamics, 35*(1), 21-38.

International Code Council. (2018). *International Building Code.* International Code Council.

Jalayer, F. (2003). *Direct Probablistic Seismic Analysis: Implementing Non-linear Dynamic Assesments.* Stanford University: PhD Thesis.

Jalayer, F., & Cornell, C. (2009). Alternative non-linear demand estimation methods for probability-based seismic assessments. *Earthquake Engineering & Structural Dynamics*, 951-972.

Jalayer, F., & Ebrahimian, H. (2017). Seismic risk assessment considering cumulative damage due to aftershocks. *Earthquake Engineering & Structural Dynamics, 46*(3), 369-389.

Jampole, E. (2017, January 3). Interview on EERI Trip to Oklahoma. (R. Chase, Interviewer)

Jones, C. (2016, December 20). *Record 5.8 Pawnee earthquake prompts more than 285 insurance claims for losses so far*. Retrieved from Tulsa World: https://www.tulsaworld.com/earthquakes/record-pawnee-earthquake-prompts-more-than-insurance-claims-for-losses/article_a60f902d-1ecf-5bcb-a0cd-5af5a3ee1c10.html

Joyner, W., & Boore, D. (1988). Measurement, characterization, and prediction of strong ground motion. *Earthquake Engineering and Soil Dynamics II, Proceedings of American Society of Civil Engineers Geotechnical Engineering Division Specialty Conference*, (pp. 43-102). Park City.

Kaklamanos, J., Baise, L., & Boore, D. (2011). Estimating unknown input parameters when implementing the NGA ground-motion prediction equations in engineering practice. *Earthquake Spectra, 27*(4), 1219-1235.

Kansas Sierra Club. (2017, March 8). *Facebook - Kansas Sierra Club*. Retrieved March 1, 2017, from https://www.facebook.com/KansasSierraClub/

Kempton, J., & Stewart, J. (2006). Prediction Equations for Significant Duration of Earthquake Ground Motions Considering Site and Near-Source Effects. *Earthquake Spectra, 22*(4), 985-1013.

Keranen, K., Weingarten, M., Abers, G., Bekins, B., & Ge, S. (2008). Sharp increase in central Oklahoma seismicity since 2008 induced by massive wastewater injection. *Science, 345*(6195), 448-451.

Khosravikia, F., Potter, A., Prakhov, V., Zalachoris, G., Cheng, T., Tiwari, A., . . . Paine, J. (2018). *Seismic Vulnerability and Post-Event Actions for Texas Bridge Infrastructure.* FHWA/TX-17/0-6916-1, Center for Transportation Research (CTR).

Kircher, C., Reitherman, R., Whitman, R., & Arnold, C. (1997). Estimation of Earthquake Losses to Buildings. *Earthquake Spectra, 13*(4), 703-720.

Knife Chief, A. (2017). Pawnee Executive Directior, Personal Correspondence. (B. Baird, Interviewer)

Koliou, A., Filiatrault, A., & Kircher, A. (2016). Assessing Modeling Complexities on the Seismic Performance of an Instrumented Short-Period Hospital. *Journal of Performance of Constructed Facilities, 31*(1), 04016078.

Lacey, M. (2011, November 7). *A Seasoned Combatant of Tornadoes Now Finds the Earth Is Moving, Too*. (The New York Times) Retrieved October 2017, from http://www.nytimes.com/2011/11/08/us/oklahoma-earthquakes-damage-st-gregorys-university.html

Lee, J., & Fenves, G. (1998). Plastic-Damage Model for Cyclic Loading of Concrete Structures. *Journal of Engineering Mechanics, 124*(8), 892-900.

Lee, J., & Fenves, G. L. (1998). Plastic-Damage Model for Cyclic Loading of Concrete Structures. *Journal of Engineering Mechanics (ASCE), 124*(8), 892-900.

Li, Q., & Ellingwood, B. (2007). Performance evaluation and damage assessment of steel frame buildings under main shock–aftershock earthquake sequences. *Earthquake Engineering & Structural Dynamics, 36*(3), 405-427.

Liel, A., Luco, N., Raghunandan, M., & Champion, C. (2015). Modifications to risk-targeted seismic design maps for subduction and near-fault hazards. *12th International Conference on Applications of Statistics and Probability in Civil Engineering, ICASP12.* Vancouver.

Lilliefors, H. (1967). On the Kolmogorov-Smirnov test for normality with mean and variance unknown. *Journal of the American statistical Association, 62*(318), 399-402.

Liu, T., Luco, N., Liel, A., & Hoover, S. (2017). Building collapse and life endangerment risks from induced seismicity in the United States. *16th World Conference in Earthquake Engineering.* Santiago, Chile.

Llenos, A., & Michael, A. (2013). Modeling Earthquake Rate Changes in Oklahoma and Arkansas: Possible Signatures of Induced Seismicity. *Bulletin of the Seismological Society of America, 103*(5), 2850-2861.

Lotfi, H., & Shing, P. (1994). Interface model applied to fracture of masonry structures. *Journal of Structural Engineering, 120*(1), 63-80.

Lourenco, P. B. (1996). *Computational Strategies for Masonry Structures.* PhD Thesis.

Lourenco, P., Rots, J., & Blaauwendraad, J. (1998). Continuum model for masonry: parameter estimation and validation. *Journal of Structural Engineering, 124*(6), 642–652.

Luco, N., & Cornell, A. (2007). Structure-specific scalar intensity measures for near-source and ordinary earthquake ground motions. *Earthquake Spectra, 23*(2), 357-392.

Luco, N., Bazzuro, P., & Cornell, C. (2004). Dynamic versus static computation of the residual capacity of a mainshock-damaged building to withstand an aftershock. *13th World conference on earthquake engineering.* Vancouver.

Luco, N., Ellingwood, B. R., Hamburger, R. O., Hooper, J. D., Kimball, J. K., & Kircher, C. A. (2007). Risk-targeted versus current seismic design maps for the conterminous United States.

Magenes, G., & Calvi, G. (1997). In-plane seismic response of brick masonry walls. *Earthquake Engineering & Structural Dynamics, 26*(11), 1091-1112.

Mahin, S. (1980). Effects of duration and aftershocks on inelastic design earthquakes. *Proceedings of the Seventh World Conference on Earthquake Engineering, 5,* pp. 677-680. Instanbul.

Marafi, N., Berman, J., & Eberhard, M. (2016). Ductility-dependent intensity measure that accounts for ground-motion spectral shape and duration. *Earthquake Engineering & Structural Dynamics, 45*(4), 653-672.

Marafi, N., Eberhard, M., Berman, J., Wirth, E., & Frankel, A. (2017). Effects of deep basins on structural collapse during large subduction earthquakes. *Earthquake Spectra, 33*(3), 963-997.

Miranda, E., & Davalos, H. (2018). Improved approach to estimate the probability of collapse of structures during earthquakes. *Proceedings of the 11th National Conference in Earthquake Engineering.* Los Angeles: Earthquake Engineering Research Institute.

Mohammed, M., Sanders, D., & Buckle, I. (2015). Shake Table Tests of Reinforced Concrete Bridge Columns Under Long Duration Ground Motions. *6th International Conference on Advances in Experimental Structural Engineering.* University of Illinois.

Moschetti, M., Thompson, E., Powers, P., Hoover, S., & McNamara, D. (2018). Ground Motions from Induced Earthquakes in Oklahoma and Kansas. *Seismological Research Letters*, In Press.

National Research Council (NRC). (2013). *Induced Seismicity Potenial in Energy Technologies.* Washington DC: National Academy of Sciences.

Nazari, N., van De Lindt, J., & Li, Y. (2013). Effect of mainshock-aftershock sequences on woodframe building damage fragilities. *Journal of Performance of Constructed Facilities, 29*(1), 04014036.

NIST. (2012). *GCR 12-917-21 Soil-structure interaction for building structures.* US Department of Commerce.

Novakovic, M., & Atkinson, G. (2018). Empirically calibrated ground-motion prediction equation for Oklahoma. *Bulletin of the Seismological Society of America, 108*(5A), 2444-2461.

Oklahoma Insurance Commisson. (2017, March 17). Oklahoma Earthquake Insurance Data. Oklahoma.

Pacific Engineering Research Center (PEER). (2016b). *OpenSees*. (University of California Berkeley) Retrieved May 2016, from http://opensees.berkeley.edu/

Pallarés, F. J., Agüero, A., & Martín, M. (2006). Seismic behaviour of industrial masonry chimneys. *International Journal of Solids and Structures, 43*(7), 2076-2090.

Pan, Y., Ventura, C., & Finn, W. (2018). Effects of Ground Motion Duration on the Seismic Performance and Collapse Rate of Light-Frame Wood Houses. *Journal of Structural Engineering, 144*(8), 04018112.

Pang, W., & Shirazi, S. (2013). Corotational Model for Cyclic Analysis of Light-frame Wood Shear Walls and Diaphragms. *ASCE Journal of Structural Engineering, Special issue NEES 2: Advances in Earthquake Engineering, 139*(8), 1303-1317.

Pang, W., Ziaei, E., & Filiatrault, A. (2012). A 3D Model for Collapse Analysis of Soft-story Light-frame Wood Buildings. *World Conference on Timber Engineering.* Auckland, NZ.

Park, S., & van de Lindt, J. (2009). Formulation of seismic fragilities for a wood-frame building based on visually determined damage indexes. *Journal of Performance of Constructed Facilities, 23*(5), 346-352.

Park, Y., & Ang, A. (1985). Mechanistic seismic damage model for reinforced concrete. *Journal of Structural Engineering, 111*(4), 722-739.

PEER. (2018). *Next Generation Attenuation (NGA) - Sub.* In Preparation: PEER.

Pei, S., & van de Lindt, J. (2011). "Seismic numerical modeling of a six-story light-frame wood building: Comparison with experiments. *Journal of Earthquake Engineering, 15*(6), 924-941.

Pei, S., van de Lindt, J., Pryor, S., Shimizu, H., Isoda, H., & Rammer, D. (2010). *Seismic testing of a full-scale mid-rise building: The NEESWood capstone test.* MCEER.

Petersen, M. D., Moschetti, M. P., Powers, P. M., Mueller, C. S., Haller, K. M., Frankel, A. D., . . . Wheeler, R. (2014). *Documentation for the 2014 Update of the United States National Seismic Hazard Mpas.* Reston, VA: US Geological Survey.

Petersen, M. D., Mueller, C. S., P, M. M., Hoover, S. M., Llenos, A. L., Ellsworth, W. L., . . . Rukstales, K. S. (2016). Seismic-Hazard Forecast for 2016 Including Induced and Natural Earthquakes in the Central and Eastern United States. *Seismological Research Letters, 87*(6), 1327-1341.

Petersen, M., & Shumway, A. (2018, June). Personal Communication.

Petersen, M., Mueller, C., Moschetti, M., Hoover, S., Rukstales, K., McNamara, D., . . . Cochran, E. (2018). 2018 One-Year Seismic Hazard Forecast for the Central and Eastern United States from Induced and Natural Earthquakes. *Seismological Research Letters, 89*(3), 1049-1061.

Pinheiro, J., Bates, D., DebRoy, S., & Sarkar, D. (2014). Linear and nonlinear mixed effects models. *R package version, 3*.

Quitoriano, V., & Wald, D. (2017, February). Personal Communication.

Raghunandan, M., & Liel, A. (2013). Effect of ground motion duration on earthquake-induced structural collapse. *Structural Safety, 41*, 119-133.

Raghunandan, M., Liel, A. B., & Luco, N. (2015). Aftershock collapse vulnerability assessment of reinforced concrete frame structures. *Earthquake Engineering & Structural Dynamics, 44*(3), 419-439.

Rennolet, S., Moschetti, M., Thompson, E., & Yeck, W. (2018). A Flatfile of Ground Motion Intensity Measurements from Induced Earthquakes in Oklahoma and Kansas. *Earthquake Spectra, 34*(1), 1-20.

Rubinstein, J. L. (2015). Myths and Facts on Wastewater Injection, Hydraulic Fracturing, Enhanced Oil Recovery, and Induced Seismicity. *Seismological Research Letters, 86*(4), 1060-1067.

Ruiz-Garcia, J., & Negrete-Manriquez, J. C. (2011). Evaluation of drift demands in existing steel frames under as-recorded far-field and near-fault mainshock–aftershock seismic sequences. *Engineering Structures, 33*(2), 621-634.

Ryu, H., Luco, N., Uma, S., & Liel, A. (2011). Developing Fragilities for Mainshock-Damaged Structures through Incremental Dynamic Analysis. *Proceedings of the Ninth Pacific Conference on Earthquake Engineering: Building an Earthquake-Resilient Society.* Auckland, NZ.

Sakamoto, Y., Ishiguro, M., & Kitagawa, G. (1986). *Akaike information criterion statistics.* (Vol. 81). Dordrecht, The Netherlands: D. Reidel.

Schultz, R., Wang, R., Gu, Y., Haug, K., & Atkinson, G. (2017). A seismological overview of the induced earthquakes in the Duvernay play near Fox Creek, Alberta. *Journal of Geophysical Research: Solid Earth, 122*(1), 492-505.

Sewell, B. (2017). Pawnee Mayor, Personal Communication.

Shokrabadi, M., & Burton, H. (2018). Risk-based assessment of aftershock and mainshock-aftershock seismic performance of reinforced concrete frames. *Structural Safety, 73*, 64-74.

Simulia. (2013). *ABAQUS 6.13 Documentation.* Retrieved May 2016, from http://bobcat.nus.edu.sg:2080/v6.13/index.html

Stafford, P. (2014). Crossed and nested mixed-effects approaches for enhanced model development and removal of the ergodic assumption in empirical ground-motion models. *Bulletin of the Seismological Society of America, 104*(2), 702-719.

State Corporation of the State of Kansas. (2015). *Order Reducing Saltwater Injection Rates.* The State Corporation of the State of Kansas.

Tarque, N., Camata, G., Spacone, E., Varum, H., & Blondet, M. (2014). Nonlinear Dynamic Analysis of a Full-Scale Unreinforced Adobe Model. *Earthquake Spectra*, *30*(4), 1643-1661.

Taylor, J., Celebi, M., Greer, A., Jampole, E., Masroor, A., Melton, S., . . . Xiao, Y. (2017). *EERI Earthquake Reconnaissance Team Report: M5.0 Cushing, Oklahoma, USA Earthquake on November 7, 2016.* Oakland, CA: Earthquake Engineering Research Institute.

Tesfamariam, S., Goda, K., & Mondal, G. (2015). Seismic vulnerability of reinforced concrete frame with unreinforced masonry infill due to main shock–aftershock earthquake sequences. *Earthquake Spectra, 31*(3), 427-1449.

The Donley Brothers Company. (1936). *The Donley Book of Sucessful Fireplaces.* Cleveland, OH: The Donley Brothers Company.

TMS. (2011). *The Masonry Society Joints Committee. Building code requirements for masonry structures (TMS 402-11/ACI 530-11/ASCE 5-11).* Boulder, CO: The Masonry Society.

Tracy, A., & Javernick-Will, A. (2018). *Induced Seismicity Survey Results.* Boulder: University of Colorado Boulder.

Trapasso, C. (2017, September 27). *Life in the Earthquake Capital of the U.S.: A Tale of Man-Made Disasters and Survival*. Retrieved from Realtor.com: https://www.realtor.com/news/trends/man-made-earthquakes-in-oklahoma/

Trifunac, M., & Brady, A. (1975). A study on the duration of strong earthquake ground motion. *Bulletin of the Seismological Society of America, 65*(3), 581-626.

University of California Berkeley. (2016). *OpenSees*. (University of California Berkeley) Retrieved May 2016, from http://opensees.berkeley.edu/

USGS. (2016, September 3). *M 5.8 - 14km NW of Pawnee, Oklahoma*. Retrieved from United States Geological Survey: https://earthquake.usgs.gov/earthquakes/eventpage/us10006jxs#shakemap

USGS. (2016, September 3). *Magnitude 5.8 Earthquake in Oklahoma*. Retrieved October 2016, from United States Geological Survey: https://www.usgs.gov/news/magnitude-56-earthquake-oklahoma

USGS. (2017, March 8). *Earthquake Hazards Program - Earthquake Catalog*. Retrieved March 1, 2017, from United States Geological Survey: https://earthquake.usgs.gov/earthquakes/search/

USGS. (2017). *Earthquake Statistics*. Retrieved from United States Geological Survey: https://earthquake.usgs.gov/earthquakes/browse/stats.php

USGS. (2018, October). *Cascadia Subduction Zone*. Retrieved from United States Geological Survey: https://earthquake.usgs.gov/data/crust/cascadia.php

USGS. (2018). *Unified Hazard Tool*. (USGS) Retrieved from United States Geological Survey: https://earthquake.usgs.gov/hazards/interactive/

Vamvatsikos, D., & Cornell, C. A. (2002). Incremental Dynamic Analysis. *Eathquake Engineering & Structural Dynamics, 31*(3), 491-514.

van de Lindt, J., Gupta, R., Pei, S., Tachibana, K., Araki, Y., Rammer, D., & Isoda, H. (2010). Damage assessment of a full-scale six-story wood-frame building following triaxial shake table tests. *Journal of Performance of Constructed Facilities, 26*(1), 17-25.

van de Lindt, J., Pei, S., Liu, H., & Filiatrault, A. (2009). Three-dimensional seismic response of a full-scale light-frame wood building: Numerical study. *Journal of Structural Engineering, 136*(1), 56-65.

Van Houtte, C., Bannister, S., Holden, C., Bourguignon, S., & McVerry, G. (2017). The New Zealand strong motion database. *Bulletin of the New Zealand Society of Earthquake Engineering, 50*(1).

Walling, M., Kuehn, N., Abrahmson, N., & Mazzoni, S. (2018). Regional Ground Motion Duration Prediction Model for Subduction Regions. *11th National Conference in Earthquake Engineering.* Los Angeles, CA.

Weingarten, M., Ge, S., Godt, W., Bekins, B., & Rubinstein, J. (2015). High-rate injection is associated with the increase in U.S. mid-continent seismicity. *348*(6241), 1336-1340.

Wilson, M., Foulger, J., Davies, R., & Julian, B. (2017). HiQuake: The Human-Induced Earthquake Database. *Seismological Research Letters, 88*(6), 1560-1565.

Wong, H. (1975). *Dynamic soil-structure interaction.* PhD Thesis: California Institute of Technology.

Yenier, E., & Atkinson, G. (2015b). A regionally-adjustable generic GMPE based on stochastic point-source simulations: Application to central and eastern North America. *Bulletin of the Seismological Society of America, 105*(4), 1989-2009.

Zhong, K., & Deierlein, G. (2018, June). Personal Communication.

A APPENDIX

A.1 ABAQUS WALLETE CALIBRATION

This section provides more detailed information regarding the *ABAQUS* model and the calibrating of the material properties described in Section 2.3.

To represent the chimney, we first modeled it in two-dimensions (2-D) in the in-plane direction using the finite element software *ABAQUS* (Simulia, 2013). The masonry was modeled with an isotropic homogenous material, similar to a number of previous studies modeling masonry, e.g., (Tarque, et al., 2014; Lourenco, et al., 1998; Calderini & Lagomarsino, 2008; Pallarés, et al., 2006). There are many other approaches for masonry modeling (Lotfi & Shing, 1994), including high fidelity approaches that model brick, mortar and interface separately, or use a discrete/rigid element approach (DeJong, 2009; Casolo & Pena, 2007). However, these models are computationally intensive and difficult to calibrate robustly, and the homogeneous material model is sufficient for investigating ground motion impacts on chimneys.

The homogeneous material used in the finite element model was intended to capture the composite behavior of masonry, including the element stress-strain response of clay brick units, mortar between the bricks, and their interface. Figure A.1 shows the monotonic backbone of the compressive and tensile responses implemented to represent the masonry, based on the *ABAQUS* so-called "Concrete Damage Plasticity" (Lee & Fenves, 1998) material model. This material model is similar to that employed by Lourenco et al. (1998) and is applicable to quasi-brittle materials under cyclic loading. Compressive crushing behavior and post peak softening is governed by the compressive fracture energy (i.e., the area under the compressive curve post peak).

Tensile cracking and the tensile softening behavior is defined by an exponential decay that is governed by the tensile fracture energy.

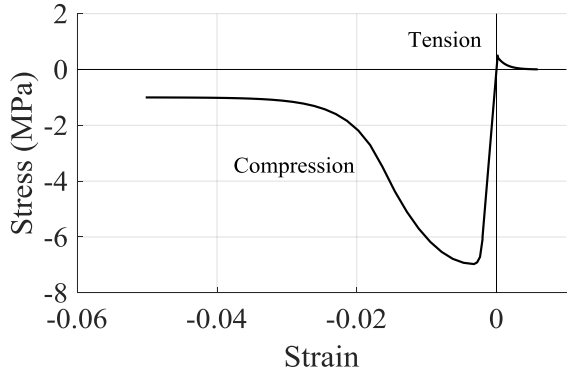

Figure A.1. Stress-strain relationship used to model homogenous masonry material in ABAQUS model of the wallette. The same relationship is used for the chimney, with modifications to the tensile fracture energy due to changes in mesh size.

The properties of this homogenous material were calibrated using a model wallette specimen in *ABAQUS*. This wallette is a red clay brick and mortar wall that Lourenco (1996) tested experimentally and modeled numerically. The wallette masonry material is assumed to be the same masonry material found in the chimney and the brick size used in the specimen is consistent with U.S. construction.

The material properties defining the compression and tensile behavior of the masonry were obtained by adjusting the wallette model properties with the goal of matching the top displacement versus base shear curve and the diagonal crack failure mechanism reported by Lourenco (1996) in their experiments and numerical model of the same wallette. Quadrilateral constant strain elements were employed with a mesh size (defined by the hypotenuse length across the rectangular element) of 0.04 meters. The force-displacement curves and failure mechanisms from both studies are shown in Figure A.2, demonstrating reasonable agreement between the wallette models developed in this study and Lourenco (1996). The stress-strain response of the calibrated material model is provided in Figure A.1.

The calibrated homogenous masonry material model was assigned to the full-scale *ABAQUS* chimney model. Partitions with varying thicknesses were defined to accurately capture the changes in thickness of the typical chimney (in the out of plane direction) in the 2-D model. Again, the model consists of quadrilateral constant strain elements. The mesh size was larger than that used for the wallette. ensuring small enough elements to capture the critical geometric and bending characteristics of the wall, but large enough to ensure responses are accurate in the softening region where strain localization can lead to non-unique solutions (see e.g. Calabrese, et al., 2010). After applying gravity loads (self-weight), this model was subjected to a lateral displacement at the top of the chimney producing the pushover response presented in Figure 2.4. Pushover led to a flexural failure mechanism characterized by tensile cracking and compressive crushing at the bottom of the flue and the top of the chimney base, rather than a shear failure. Dynamic analyses of the finite element model produced a similar, flexurally-dominated failure mode in the modeled direction. Out-of-plane failure mechanisms were not represented in the model.

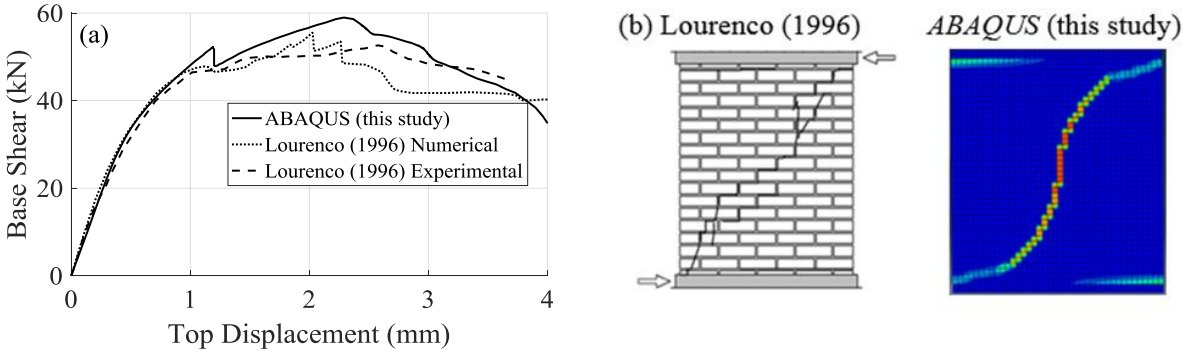

Figure A.2. Comparison of our ABAQUS model of a masonry wallette specimen with previous work (Lourenco, 1996), showing (a) force-displacement response and (b) diagonal crack propagation. In (b) the colors represent the plastic tensile strain, with red and orange indicating the largest values. The figure from Lourenco (1996) in (b) is from experimental work and taken directly from that publication.

A.2 SEISMIC HAZARD DEAGREGATION

In this section, the mean hazard deaggregations, separated by source type, for Los Angeles, San Francisco, Seattle, Portland, Anchorage, and Eugene are provided in Tables A.1-A.6. The deaggregation information is collected from the USGS Unified Hazard tool, which references the 2014 USGS Hazard Model (Petersen, et al., 2014; USGS, 2018). Deaggregations are shown for Sa(T=0.3s) assuming a V_{s30} of 760 m/s. The exact latitude and longitudes for each site are provided in Table 4.1. These deaggregations are provided in addition to those provided in Section 4.6.2, which includes deaggregation information for Eugene for Sa(T=0.3s) at the selected hazard levels.

Table A.1. Seismic hazard deaggregation from the 2014 USGS Hazard Model for T=0.3s in Los Angeles showing mean M, R, ε, and percent contribution for all source types at selected hazard levels.

		Crustal			
Hazard Level	**Sa(T=0.3s) [g]**	**M**	**R [km]**	**ε**	**%**
75	0.26	6.6	26	0.1	100
275	0.57	6.8	16	0.5	100
475	0.76	6.9	14	0.6	100
975	1.08	7.0	12	0.8	100
2475	1.59	7.0	10	1.2	100
4000	1.90	7.1	9	1.3	100
6000	2.20	7.1	9	1.5	100
8000	2.40	7.1	9	1.6	100
10000	2.57	7.1	9	1.6	100

Table A.2. Seismic hazard deaggregation from the 2014 USGS Hazard Model for T=0.3s in San Francisco showing mean M, R, ε, and percent contribution for all source types at selected hazard levels.

		Crustal			
Hazard Level	**Sa(T=0.3s) [g]**	**M**	**R [km]**	**ε**	**%**
75	0.30	6.9	22	0.2	100
275	0.63	7.2	17	0.8	100
475	0.79	7.3	16	1.0	100
975	1.06	7.4	15	1.3	100
2475	1.46	7.4	14	1.7	100
4000	1.66	7.5	14	1.8	100
6000	1.86	7.5	14	2.0	100
8000	2.01	7.5	13	2.0	100
10000	2.14	7.5	13	2.1	100

Table A.3. Seismic hazard deaggregation from the 2014 USGS Hazard Model for T=0.3s in Seattle showing mean M, R, ε, and percent contribution for all source types at selected hazard levels.

		Crustal				Inslab				Interface			
Hazard Level	**Sa(T=0.3s) [g]**	**M**	**R [km]**	**ε**	**%**	**M**	**R [km]**	**ε**	**%**	**M**	**R [km]**	**ε**	**%**
75	0.19	6.3	23	0.0	42	6.7	75	0.3	49	8.9	115	-0.4	10
275	0.43	6.4	14	0.3	43	6.9	70	0.8	44	9.0	108	0.6	12
475	0.56	6.5	12	0.5	45	6.9	68	1.1	42	9.0	106	0.9	13
975	0.78	6.6	10	0.7	49	7.0	66	1.3	39	9.0	103	1.3	12
2475	1.14	6.7	8	1.0	54	7.1	64	1.6	35	9.0	101	1.7	12
4000	1.35	6.7	7	1.2	56	7.1	63	1.8	32	9.1	99	1.9	11
6000	1.55	6.7	6	1.3	59	7.1	62	1.9	31	9.1	97	2.0	11
8000	1.69	6.8	6	1.4	60	7.1	62	2.0	29	9.1	96	2.1	10
10000	1.81	6.8	6	1.5	62	7.1	62	2.0	28	9.1	96	2.1	10

Table A.4. Seismic hazard deaggregation from the 2014 USGS Hazard Model for T=0.3s in Portland showing mean M, R, ε, and percent contribution for all source types at selected hazard levels.

		Crustal				Inslab				Interface			
Hazard Level	**Sa(T=0.3s) [g]**	**M**	**R [km]**	**ε**	**%**	**M**	**R [km]**	**ε**	**%**	**M**	**R [km]**	**ε**	**%**
75	0.07	6.1	47	-0.3	61	6.9	143	0.1	19	8.8	126	-1.5	20
275	0.21	6.2	21	0.0	50	7.0	95	0.4	13	8.9	112	-0.2	37
475	0.32	6.2	16	0.2	48	7.0	82	0.6	12	8.9	107	0.2	40
975	0.49	6.3	12	0.4	48	7.0	72	0.9	11	8.9	101	0.7	41
2475	0.78	6.4	8	0.6	50	7.0	65	1.3	9	9.0	95	1.2	40
4000	0.97	6.5	6	0.8	53	7.1	63	1.5	9	9.0	93	1.4	39
6000	1.14	6.6	6	0.9	54	7.1	62	1.6	8	9.0	91	1.5	37
8000	1.27	6.6	5	0.9	56	7.1	61	1.7	8	9.0	89	1.7	36
10000	1.39	6.6	5	1.0	57	7.1	60	1.8	7	9.0	88	1.7	35

Table A.5. Seismic hazard deaggregation from the 2014 USGS Hazard Model for T=0.3s in Anchorage showing mean M, R, ε, and percent contribution for all source types at selected hazard levels.

		Crustal				Inslab				Interface			
Hazard Level	**Sa(T=0.3s) [g]**	**M**	**R [km]**	**ε**	**%**	**M**	**R [km]**	**ε**	**%**	**M**	**R [km]**	**ε**	**%**
75	0.38	6.2	20	0.4	36	6.6	83	1.2	36	8.1	56	0.0	28
275	0.69	6.3	14	0.7	34	6.8	77	1.6	27	8.7	44	0.1	38
475	0.85	6.3	12	0.9	33	6.9	75	1.8	23	8.9	41	0.2	44
975	1.11	6.3	10	1.1	31	7.0	73	2.0	17	9.0	39	0.5	52
2475	1.50	6.4	9	1.4	29	7.1	70	2.3	12	9.2	36	0.9	59
4000	1.69	6.4	9	1.6	29	7.2	69	2.4	10	9.2	36	1.1	61
6000	1.87	6.4	8	1.7	28	7.2	67	2.5	8	9.2	36	1.3	63
8000	2.01	6.4	8	1.7	28	7.2	67	2.5	7	9.2	36	1.5	65
10000	2.13	6.4	8	1.8	28	7.3	66	2.6	6	9.2	36	1.6	65

Table A.6. Seismic hazard deaggregation from the 2014 USGS Hazard Model for T=0.3s in Eugene showing mean M, R, ε, and percent contribution for all source types at selected hazard levels.

		Crustal				Inslab				Interface			
Hazard Level	**Sa(T=0.3s) [g]**	**M**	**R [km]**	**ε**	**%**	**M**	**R [km]**	**ε**	**%**	**M**	**R [km]**	**ε**	**%**
75	0.03	6.4	121	0.3	65	6.9	128	-1.2	11	8.7	108	-2.8	24
275	0.13	6.5	63	0.7	17	6.9	92	-0.3	15	8.8	98	-1.1	68
475	0.23	6.5	40	0.8	8	6.9	80	0.2	13	8.8	93	-0.4	80
975	0.40	6.5	25	0.9	4	7.0	71	0.7	10	8.9	85	0.2	86
2475	0.69	6.5	17	1.2	3	7.0	64	1.1	9	8.9	79	0.8	89
4000	0.87	6.5	15	1.3	2	7.0	62	1.3	8	8.9	76	1.0	90
6000	1.03	6.5	13	1.4	2	7.1	61	1.5	7	9.0	75	1.2	91
8000	1.16	6.6	12	1.5	2	7.1	60	1.6	7	9.0	73	1.3	91
10000	1.26	6.6	11	1.5	2	7.1	59	1.7	7	9.0	73	1.4	92

A.3 TARGET SARATIO AND $Ds_{5\text{-}75,NGA}$

In this section, target $SaRatio(T_1,3T_1)$ and target $Ds_{5\text{-}75,NGA}$ are provided for periods of 0.2s, 0.3s and 0.5s in Los Angeles, San Francisco, Seattle, Portland, Anchorage, and Eugene in Tables A.7-A.24. These target $SaRatio(T_1,3T_1)$ and $Ds_{5\text{-}75,NGA}$ are calculated following the methods detailed in Section 4.6. These values are provided in addition to the target $SaRatio(T_1,3T_1)$ and $Ds_{5\text{-}75,NGA}$ values described in Table 4.6, Table 4.7, and Table 4.8.

A.3.1 Los Angeles

Table A.7. Hazard and target spectral shapes and duration at 0.2 s period in Los Angeles.

Hazard Level	**Sa(T=0.2s) [g]**	***SaRatio (0.19,0.57)***	***$Ds_{5\text{-}75,NGA}$* [s]**
75	0.32	1.8	4.5
275	0.70	1.9	4.1
475	0.94	2.0	4.0
975	1.32	2.2	3.9
2475	1.93	2.4	3.9
4000	2.31	2.5	3.9
6000	2.64	2.6	3.8
8000	2.91	2.7	3.9
10000	3.13	2.7	3.8

Table A.8. Hazard and target spectral shapes and duration at 0.3 s period in Los Angeles.

Hazard Level	**Sa(T=0.3s) [g]**	***SaRatio (0.29,0.87)***	***$Ds_{5\text{-}75,NGA}$* [s]**
75	0.26	2.1	4.8
275	0.57	2.3	4.3
475	0.76	2.4	4.2
975	1.08	2.5	4.2
2475	1.59	2.7	4.1
4000	1.90	2.8	4.1
6000	2.20	2.9	4.0
8000	2.40	3.0	4.1
10000	2.57	3.0	4.0

Table A.9. Hazard and target spectral shapes and duration at 0.5 s period in Los Angeles.

Hazard Level	**Sa(T=0.5s) [g]**	***SaRatio (0.51,1.53)***	***$Ds_{5\text{-}75,NGA}$* [s]**
75	0.18	2.6	5.4
275	0.39	2.9	5.0
475	0.53	2.9	4.9
975	0.75	3.0	4.8
2475	1.12	3.2	4.7
4000	1.35	3.3	4.7
6000	1.56	3.4	4.6
8000	1.71	3.4	4.7
10000	1.84	3.5	4.7

A.3.2 San Francisco

Table A.10. Hazard and target spectral shapes and duration at 0.2 s period in San Francisco.

Hazard Level	Sa(T=0.2s) [g]	*SaRatio (0.19,0.57)*	$Ds_{5\text{-}75,NGA}$ [s]
75	0.37	1.5	5.3
275	0.76	1.7	5.8
475	0.97	1.7	6.0
975	1.27	1.8	6.1
2475	1.73	2.0	6.1
4000	2.00	2.0	6.1
6000	2.25	2.1	6.1
8000	2.40	2.1	6.1
10000	2.53	2.2	6.1

Table A.11. Hazard and target spectral shapes and duration at 0.3 s period in San Francisco.

Hazard Level	Sa(T=0.3s) [g]	*SaRatio (0.29,0.87)*	$Ds_{5\text{-}75,NGA}$ [s]
75	0.30	1.7	5.5
275	0.63	1.9	6.2
475	0.79	1.9	6.4
975	1.06	2.0	6.6
2475	1.46	2.1	6.7
4000	1.66	2.2	6.8
6000	1.86	2.3	6.9
8000	2.01	2.3	6.9
10000	2.14	2.3	6.9

Table A.12. Hazard and target spectral shapes and duration at 0.5 s period in San Francisco.

Hazard Level	Sa(T=0.5s) [g]	*SaRatio (0.51,1.53)*	$Ds_{5\text{-}75,NGA}$ [s]
75	0.21	2.2	6.1
275	0.44	2.2	7.1
475	0.57	2.2	7.5
975	0.76	2.3	8.0
2475	1.06	2.4	8.3
4000	1.23	2.5	8.5
6000	1.39	2.5	8.7
8000	1.50	2.5	8.8
10000	1.58	2.6	8.9

A.3.3 Seattle

Table A.13. Hazard and target spectral shapes and duration at 0.2 s period in Seattle.

Hazard Level	Sa(T=0.2s) [g]	*SaRatio (0.19,0.57)*	$Ds_{5\text{-}75,NGA}$ [s]
75	0.24	1.9	5.1
275	0.55	2.0	4.4
475	0.73	2.0	4.2
975	1.01	2.1	3.9
2475	1.47	2.1	3.6
4000	1.72	2.2	3.4
6000	1.97	2.2	3.3
8000	2.17	2.2	3.3
10000	2.31	2.2	3.2

Table A.14. Hazard and target spectral shapes and duration at 0.3 s period in Seattle.

Hazard Level	Sa(T=0.3s) [g]	*SaRatio (0.29,0.87)*	$Ds_{5\text{-}75,NGA}$ [s]
75	0.19	2.0	5.3
275	0.43	2.2	4.7
475	0.56	2.2	4.5
975	0.78	2.3	4.2
2475	1.14	2.3	3.8
4000	1.35	2.3	3.7
6000	1.55	2.3	3.6
8000	1.69	2.3	3.5
10000	1.81	2.3	3.5

Table A.15. Hazard and target spectral shapes and duration at 0.5 s period in Seattle.

Hazard Level	Sa(T=0.5s) [g]	*SaRatio (0.51,1.53)*	$Ds_{5\text{-}75,NGA}$ [s]
75	0.12	2.7	5.9
275	0.28	2.7	5.4
475	0.37	2.7	5.2
975	0.52	2.6	4.9
2475	0.76	2.6	4.6
4000	0.91	2.6	4.5
6000	1.05	2.6	4.3
8000	1.15	2.6	4.3
10000	1.23	2.6	4.2

A.3.4 Portland

Table A.16. Hazard and target spectral shapes and duration at 0.2 s period in Portland.

Hazard Level	Sa(T=0.2s) [g]	*SaRatio (0.19,0.57)*	$Ds_{5\text{-}75,NGA}$ [s]
75	0.08	1.5	8.0
275	0.26	1.5	6.4
475	0.38	1.5	5.9
975	0.59	1.5	5.3
2475	0.96	1.6	4.7
4000	1.17	1.6	4.4
6000	1.39	1.6	4.2
8000	1.55	1.7	4.1
10000	1.68	1.7	4.0

Table A.17. Hazard and target spectral shapes and duration at 0.3 s period in Portland.

Hazard Level	Sa(T=0.3s) [g]	*SaRatio (0.29,0.87)*	$Ds_{5\text{-}75,NGA}$ [s]
75	0.07	1.8	8.4
275	0.21	1.7	7.0
475	0.32	1.7	6.5
975	0.49	1.7	5.9
2475	0.78	1.8	5.2
4000	0.97	1.8	4.9
6000	1.14	1.8	4.7
8000	1.27	1.8	4.6
10000	1.39	1.9	4.5

Table A.18. Hazard and target spectral shapes and duration at 0.5 s period in Portland.

Hazard Level	Sa(T=0.5s) [g]	*SaRatio (0.51,1.53)*	$Ds_{5\text{-}75,NGA}$ [s]
75	0.05	2.5	8.8
275	0.15	2.2	8.0
475	0.22	2.1	7.6
975	0.35	2.1	7.2
2475	0.56	2.2	6.5
4000	0.69	2.2	6.2
6000	0.82	2.2	5.9
8000	0.91	2.2	5.7
10000	1.00	2.3	5.6

A.3.5 Anchorage

Table A.19. Hazard and target spectral shapes and duration at 0.2 s period in Anchorage.

Hazard Level	Sa(T=0.2s) [g]	*SaRatio (0.19,0.57)*	$Ds_{5\text{-}75,NGA}$ [s]
75	0.44	2.0	4.5
275	0.78	1.8	4.4
475	0.97	1.7	4.5
975	1.23	1.6	4.5
2475	1.61	1.5	4.3
4000	1.81	1.4	4.2
6000	2.00	1.4	4.1
8000	2.15	1.4	3.9
10000	2.25	1.4	3.9

Table A.20. Hazard and target spectral shapes and duration at 0.3 s period in Anchorage.

Hazard Level	Sa(T=0.3s) [g]	*SaRatio (0.29,0.87)*	$Ds_{5\text{-}75,NGA}$ [s]
75	0.38	2.6	4.9
275	0.69	2.3	4.9
475	0.85	2.2	5.1
975	1.11	2.0	5.4
2475	1.50	1.8	5.7
4000	1.69	1.7	5.6
6000	1.87	1.7	5.5
8000	2.01	1.6	5.4
10000	2.13	1.6	5.3

Table A.21. Hazard and target spectral shapes and duration at 0.5 s period in Anchorage.

Hazard Level	Sa(T=0.5s) [g]	*SaRatio (0.51,1.53)*	$Ds_{5\text{-}75,NGA}$ [s]
75	0.29	3.8	5.6
275	0.53	3.3	5.8
475	0.67	3.1	6.1
975	0.89	2.9	6.7
2475	1.21	2.7	7.3
4000	1.42	2.6	7.4
6000	1.58	2.5	7.5
8000	1.69	2.5	7.5
10000	1.78	2.5	7.5

A.3.6 Eugene

Table A.22. Hazard and target spectral shapes and duration at 0.2 s period in Eugene.

Hazard Level	Sa(T=0.2s) [g]	*SaRatio (0.19,0.57)*	$Ds_{5\text{-}75,NGA}$ [s]
75	0.03	1.2	12.2
275	0.14	1.1	13.1
475	0.26	1.1	12.0
975	0.46	1.2	10.6
2475	0.80	1.3	9.2
4000	1.01	1.3	8.6
6000	1.20	1.3	8.2
8000	1.36	1.4	8.0
10000	1.48	1.4	7.8

Table A.23. Hazard and target spectral shapes and duration at 0.3 s period in Eugene.

Hazard Level	Sa(T=0.3s) [g]	*SaRatio (0.29,0.87)*	$Ds_{5\text{-}75,NGA}$ [s]
75	0.03	1.4	12.2
275	0.13	1.3	13.4
475	0.23	1.3	12.5
975	0.40	1.4	11.1
2475	0.69	1.5	9.8
4000	0.87	1.5	9.3
6000	1.04	1.6	8.9
8000	1.16	1.6	8.7
10000	1.26	1.6	8.5

Table A.24. Hazard and target spectral shapes and duration at 0.5 s period in Eugene.

Hazard Level	Sa(T=0.5s) [g]	*SaRatio (0.51,1.53)*	$Ds_{5\text{-}75,NGA}$ [s]
75	0.03	1.8	12.2
275	0.10	1.8	13.3
475	0.18	1.8	13.0
975	0.31	1.9	11.9
2475	0.53	2.0	10.9
4000	0.67	2.1	10.5
6000	0.79	2.1	10.1
8000	0.88	2.2	9.9
10000	0.96	2.2	9.8

A.4 DEVELOPMENT OF CORRELATION MODEL BETWEEN SPECTRAL ACCELERATION AND $Ds_{5\text{-}75,NGA}$

In this section, a model for the correlation between the errors of the Abrahamson et al. (2018) and Walling et al. (2018) equations is developed by the author, with assistance from Zachary Bullock. We use a database of 1,651 strong motion records taken from interface and in-slab earthquakes in the New Zealand Strong Motion Database (Van Houtte, et al., 2017) to estimate the correlations.

The current version of Walling et al. (2018) is preliminary and does not include a site term and, unsurprisingly, our analysis showed a bias with $V_{s,30}$. This bias is consistent with expectations based previous models for significant duration (Kempton & Stewart, 2006; Bommer, et al., 2009; Afshari & Stewart, 2016). To avoid these biases, we apply nonlinear regression to formulate a site term for use with the Walling et al. (2018) GMPE according to Equation 4.1:

$$\ln\left(\widehat{Ds_{5-57,NGA}}\right)_{es} = \ln\left(\mu_{source} + \mu_{path}\right)_{es} + \left(c_0 + c_1 \ln\left(\frac{V_{S,30}}{760}\right)\right)_s \tag{4.1}$$

where $\widehat{Ds_{5-57,NGA}}$ is the median estimated significant duration, μ_{source} is the source duration as calculated using the median coefficients in Walling et al. (2018), μ_{path} is the path duration as calculated using the median coefficients in Walling et al. (2018), and c_0 and c_1 are regression coefficients equal to -0.2469 and -0.1466, respectively. The subscripts e and s refer to the predictions for the s-th site in the e-th earthquake. The logarithmic errors of the adjusted model, calculated as $\varepsilon r = \ln\left(Ds_{5-75,NGA}\right) - \ln\left(\widehat{Ds_{5-75,NGA}}\right)$, pass a Lilliefors (1967) test for normality and have zero mean.

Additionally, the methodology used to formulate the correlation model requires that the model errors and uncertainty are separated into between- and within-event components. Due to its organization, the Walling et al. (2018) separates uncertainty into source and path components instead, and these estimates do not account for the site adjustment presented above. We use mixed-effects regression (e.g., Pinheiro et al. (2014)) according to Stafford (2014) to estimate between- and within-event standard deviations (τ and ϕ, respectively) for the adjusted Walling et al. (2018) model, and find that $\tau = 0.2273$ and $\phi = 0.5079$. The total standard deviation of the uncertainty around the adjusted Walling et al. (2018) predictions is given by $\sigma^2 = \tau^2 + \phi^2$. The same methodology is also used to decompose ε into between- and within-event components (δB_e and δW_{es}, respectively).

Bradley (2011) developed correlation models between the errors in predicting significant duration and pseudospectral acceleration for shallow crustal earthquakes. This correlation model is also used in this study for correlations for crustal source types. We apply the same methodology here for subduction earthquakes. First, the correlation coefficients between $\delta B_e[PSA]$ and $\delta B_e[SD]$ and between $\delta W_{es}[PSA]$ and $\delta W_{es}[SD]$ are calculated ($\rho_{\delta B_e[PSA],\delta B_e[SD]}$ and $\rho_{\delta W_{es}[PSA],\delta W_{es}[SD]}$) for a range of vibration periods (T). The between- and within-event correlation coefficients are then parameterized into trilinear and quadrilinear functions of $\ln(T)$, respectively. The form for these functions is given by Equation A.1:

$$\hat{\rho}(T) = \begin{cases} \beta_0 + \beta_1 \ln(T), & T < T_1 \\ \beta_0 + \beta_1 \ln(T_1) + \beta_2 \ln\left(\frac{T}{T_1}\right), & T_1 \leq T < T_2 \\ \beta_0 + \beta_1 \ln(T_1) + \beta_2 \ln\left(\frac{T_2}{T_1}\right) + \beta_3 \ln\left(\frac{T}{T_2}\right), & T_2 \leq T < T_3 \\ \beta_0 + \beta_1 \ln(T_1) + \beta_2 \ln\left(\frac{T_2}{T_1}\right) + \beta_3 \ln\left(\frac{T_3}{T_2}\right) + \beta_4 \ln\left(\frac{T}{T_3}\right), & T_3 \leq T \leq 10 \end{cases} \quad \text{(A.1)}$$

where $\hat{\rho}$ may be either $\rho_{\delta B_e[PSA],\delta B_e[SD]}$ or $\rho_{\delta W_{es}[PSA],\delta W_{es}[SD]}$. Table A.25 provides the coefficients for calculating the correlation between the between- and within-event errors. Please note T_1 is not equal to the fundamental period of the building in this equation.

Table A.25. Coefficients for the multilinear correlation coefficient models for subduction earthquakes.

Coefficient	$\rho_{\delta B_e[PSA],\delta B_e[SD]}$	$\rho_{\delta W_{es}[PSA],\delta W_{es}[SD]}$
β_0	-0.5692	-0.4936
β_1	-0.0125	0.0049
β_2	0.2610	0.2508
β_3	0.0188	0.4130
β_4	0	-0.0288
T_1	0.1850	0.2568
T_2	0.7550	3.0424
T_3	10	4.1195

The correlation between the total errors can then be calculated according to Equation A.2:

$$\rho(T) = \frac{\rho_{\delta B_e[PSA],\delta B_e[SD]}(T)\times\tau[PSA](T)\times\tau[SD]+\rho_{\delta W_{es}[PSA],\delta W_{es}[SD]}(T)\times\phi[PSA](T)\times\phi[SD]}{\sigma[PSA](T)\times\sigma[SD]} \quad \text{(A.2)}$$

where $\rho(T)$ is the total correlation as a function of T, $\tau[PSA](T)$ is the between-event standard deviation from Abrahamson et al. (2018) as a function of T, $\phi[PSA](T)$ is the within-event standard deviation from Abrahamson et al. (2018) as a function of T, and $\sigma[PSA](T)$ is the total standard deviation from Abrahamson et al. (2018) as a function of T.

The correlation model developed here yields estimates that are slightly more negative than those calculated according to Bradley (2011), compared in Figure A.3. There are two main factors that may contribute to this difference: (1) the definition of significant duration used by Walling et al. (2018) is somewhat different to that used in the significant duration models considered by

Bradley (2011) and (2) subduction earthquakes tend to have more low-frequency content than shallow crustal earthquakes.

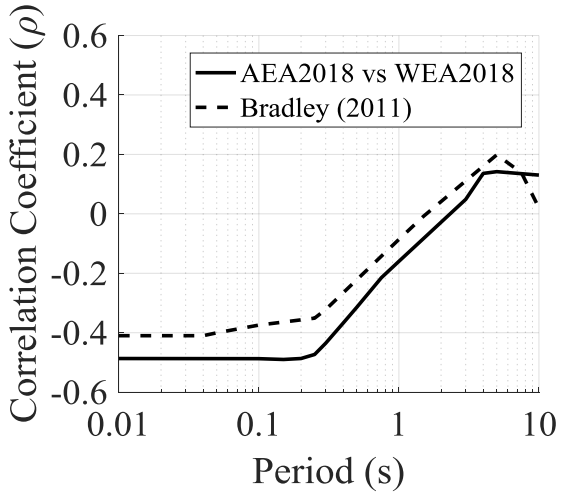

Figure A.3. Correlation models between spectral acceleration and $Ds_{5\text{-}75,NGA}$ developed in this study using Abrahamson et al (2018) (AEA2018) and Walling et al. (2018) (WEA2018) and compared to Bradley (2011) for crustal earthquakes.

Both models yield negative correlation coefficients at short periods, indicating that tendency to overpredict either pseudospectral acceleration or significant duration corresponds to tendency to under predict the other. This relationship appears slightly stronger for subduction earthquakes than for shallow crustal earthquakes. The new definition of significant duration aims to define the time over which body wave energy arrives at the site, while excluding possible periods of weak shaking between the arrive of distinct body waves (if they are present). As noted by Bradley (2011), if the duration over which body wave energy arrives at the site is shorter, there is a greater chance of superposition of waves and therefore higher motion amplitudes. Redefining significant duration in this way may make this effect more apparent in the calculated correlation coefficients. At longer periods, surface waves are more likely to be responsible for peak pseudospectral accelerations, and the correlation is reduced in magnitude.

A.5 REGRESSION CONSTANTS FOR THE TWO-STORY MULTIFAMILY BUILDING USING HAZARD-CONSISTENT IDA

In this section, regression constants derived using the hazard-consistent IDA methodology, developed by Chandramohan (2016), are provided for MFD2. Regression constants are provided at a range of Sa(T=0.3s) that correspond to the hazard levels of San Francisco, but the analyst can interpolate between these levels to obtain other intensity levels of interest for this building. The regression constants are generated using the multivariate regression shown in Equation A.3, which is very similar to Equation 4.6, except now it is generalized for all EDPs (not just collapse Sa).

$$\ln EDP = b_0 + b_1 \ln SaRatio(T_1, 3T_1) + b_2 \ln Ds_{5-75,NGA} \quad \text{(A.3)}$$

The regression constants for SDR, peak floor acceleration, and residual drift at each floor and both horizontal orthogonal directions are provided in Tables A.26-A.30. The resulting R^2 for each regression are also provided.

Table A.26. 1st-story SDR regression constants and resulting R^2 for MFD2 in both N-S and E-W directions.

		N-S Direction				E-W Direction			
Hazard Level	**Sa(T=0.3s) [g]**	**b_0**	**b_1**	**b_2**	**R^2**	**b_0**	**b_1**	**b_2**	**R^2**
75	0.30	-5.73	-0.59	-0.07	0.24	-6.23	-0.47	0.03	0.15
275	0.63	-4.69	-0.97	-0.11	0.43	-5.20	-0.86	0.03	0.31
475	0.79	-4.25	-1.15	-0.14	0.49	-4.91	-0.84	0.02	0.33
975	1.06	-3.78	-1.28	-0.16	0.57	-4.56	-0.85	0.01	0.29
2475	1.46	-2.96	-1.98	-0.16	0.57	-4.00	-1.24	0.05	0.29
4000	1.66	-2.56	-2.45	-0.13	0.52	-3.75	-1.17	0.03	0.28
6000	1.86	-2.50	-2.41	-0.09	0.54	-3.59	-1.23	0.06	0.25
8000	2.01	-2.22	-2.57	-0.09	0.55	-3.47	-1.07	0.03	0.19
10000	2.14	-2.12	-2.61	-0.07	0.56	-3.28	-1.21	0.05	0.19

Table A.27. 2nd-story SDR regression constants and resulting R^2 for MFD2 in both N-S and E-W directions.

		N-S Direction				E-W Direction			
Hazard Level	**Sa(T=0.3s) [g]**	**b_0**	**b_1**	**b_2**	**R^2**	**b_0**	**b_1**	**b_2**	**R^2**
75	0.30	-6.52	-0.80	-0.09	0.35	-7.06	-0.51	0.02	0.13
275	0.63	-5.42	-1.33	-0.09	0.43	-6.03	-0.89	0.03	0.28
475	0.79	-5.25	-1.29	-0.05	0.42	-5.65	-0.89	0.02	0.29
975	1.06	-5.20	-1.05	-0.01	0.42	-5.38	-0.79	0.04	0.26
2475	1.46	-5.27	-0.68	0.06	0.32	-5.05	-0.72	0.04	0.39
4000	1.66	-5.30	-0.44	0.05	0.22	-4.99	-0.61	0.03	0.42
6000	1.86	-5.30	-0.24	0.03	0.16	-4.98	-0.48	0.03	0.37
8000	2.01	-5.36	-0.07	0.03	0.08	-4.98	-0.43	0.04	0.29
10000	2.14	-5.36	-0.10	0.04	0.16	-5.00	-0.37	0.04	0.23

Table A.28. Residual drift regression constants and resulting R^2 for MFD2 in both N-S and E-W directions.

		N-S Direction				E-W Direction			
Hazard Level	**Sa(T=0.3s) [g]**	**b_0**	**b_1**	**b_2**	**R^2**	**b_0**	**b_1**	**b_2**	**R^2**
75	0.30	-8.38	-0.08	0.05	0.02	-8.55	-1.32	-0.05	0.23
275	0.63	-7.54	-0.46	-0.08	0.12	-7.57	-1.80	0.06	0.36
475	0.79	-6.76	-1.37	-0.15	0.28	-6.54	-2.81	-0.07	0.53
975	1.06	-5.67	-2.38	-0.22	0.49	-5.84	-3.78	-0.01	0.63
2475	1.46	-4.69	-1.86	-0.31	0.28	-5.34	-3.48	0.09	0.50
4000	1.66	-4.30	-1.47	-0.31	0.17	-5.02	-3.36	0.06	0.43
6000	1.86	-4.11	-1.13	-0.29	0.10	-5.07	-2.88	0.11	0.33
8000	2.01	-3.92	-1.03	-0.32	0.10	-5.04	-2.55	0.12	0.27
10000	2.14	-4.08	-0.89	-0.25	0.06	-4.83	-2.25	0.08	0.20

Table A.29. 2nd-floor peak acceleration regression constants and resulting R^2 for MFD2 in both N-S and E-W directions.

		N-S Direction				E-W Direction			
Hazard Level	**Sa(T=0.3s) [g]**	**b_0**	**b_1**	**b_2**	**R^2**	**b_0**	**b_1**	**b_2**	**R^2**
75	0.30	-1.10	-0.06	0.00	0.01	-1.24	-0.22	0.02	0.08
275	0.63	-0.41	-0.16	-0.02	0.09	-0.32	-0.58	0.01	0.28
475	0.79	-0.22	-0.23	-0.02	0.15	-0.09	-0.61	0.01	0.31
975	1.06	0.04	-0.34	-0.02	0.23	0.14	-0.49	0.01	0.26
2475	1.46	0.25	-0.42	-0.02	0.28	0.32	-0.17	-0.01	0.04
4000	1.66	0.25	-0.35	0.00	0.20	0.41	-0.05	-0.03	0.03
6000	1.86	0.22	-0.20	0.01	0.09	0.51	-0.05	-0.04	0.06
8000	2.01	0.21	0.01	0.00	0.00	0.50	0.08	-0.04	0.06
10000	2.14	0.20	0.07	0.00	0.01	0.59	-0.06	-0.04	0.07

Table A.30. Roof peak acceleration regression constants and resulting R^2 for MFD2 in both N-S and E-W directions.

		N-S Direction				E-W Direction			
Hazard Level	**Sa(T=0.3s) [g]**	**b_0**	**b_1**	**b_2**	**R^2**	**b_0**	**b_1**	**b_2**	**R^2**
75	0.30	-0.90	-0.26	-0.03	0.14	-1.17	-0.24	-0.01	0.08
275	0.63	-0.10	-0.49	-0.01	0.30	-0.23	-0.54	-0.02	0.26
475	0.79	0.12	-0.50	-0.01	0.33	-0.01	-0.59	-0.01	0.33
975	1.06	0.26	-0.39	0.01	0.22	0.17	-0.42	0.00	0.25
2475	1.46	0.43	-0.31	0.01	0.17	0.37	-0.26	-0.01	0.15
4000	1.66	0.29	-0.14	0.04	0.12	0.46	-0.18	-0.03	0.12
6000	1.86	0.29	-0.10	0.06	0.17	0.58	-0.23	-0.03	0.18
8000	2.01	0.32	0.01	0.04	0.09	0.58	-0.25	-0.01	0.11
10000	2.14	0.41	-0.06	0.03	0.04	0.61	-0.20	-0.01	0.09